



**NAVAL  
POSTGRADUATE  
SCHOOL**

**MONTEREY, CALIFORNIA**

**DISSERTATION**

**LIGAND EFFECTS IN ALUMINUM CLUSTER-BASED  
ENERGETIC MATERIALS**

by

Warren W. Tomlinson

September 2017

Dissertation Supervisor:

Joseph Hooper

**Approved for public release. Distribution is unlimited.**

THIS PAGE INTENTIONALLY LEFT BLANK

REPORT DOCUMENTATION PAGE			Form Approved OMB No. 0704-0188	
Public reporting burden for this collection of information is estimated to average 1 hour per response, including the time for reviewing instruction, searching existing data sources, gathering and maintaining the data needed, and completing and reviewing the collection of information. Send comments regarding this burden estimate or any other aspect of this collection of information, including suggestions for reducing this burden, to Washington headquarters Services, Directorate for Information Operations and Reports, 1215 Jefferson Davis Highway, Suite 1204, Arlington, VA 22202-4302, and to the Office of Management and Budget, Paperwork Reduction Project (0704-0188) Washington, DC 20503.				
1. AGENCY USE ONLY (Leave blank)	2. REPORT DATE September 2017	3. REPORT TYPE AND DATES COVERED Dissertation		
4. TITLE AND SUBTITLE LIGAND EFFECTS IN ALUMINUM CLUSTER-BASED ENERGETIC MATERIALS			5. FUNDING NUMBERS N0001417WX00357	
6. AUTHOR(S) Warren W. Tomlinson				
7. PERFORMING ORGANIZATION NAME(S) AND ADDRESS(ES) Naval Postgraduate School Monterey, CA 93943-5000			8. PERFORMING ORGANIZATION REPORT NUMBER	
9. SPONSORING /MONITORING AGENCY NAME(S) AND ADDRESS(ES) N/A			10. SPONSORING / MONITORING AGENCY REPORT NUMBER	
11. SUPPLEMENTARY NOTES The views expressed in this thesis are those of the author and do not reflect the official policy or position of the Department of Defense or the U.S. Government. IRB number ___N/A___.				
12a. DISTRIBUTION / AVAILABILITY STATEMENT Approved for public release. Distribution is unlimited.			12b. DISTRIBUTION CODE	
13. ABSTRACT (maximum 200 words)  This dissertation examines the electronic structure and thermochemistry of low-valent aluminum clusters that may serve as precursors for new energetic materials. Clusters such as $Al_{50}Cp^*_{12}$ ( $Cp^*=C_5Me_5$ ) have theoretical heats of combustion more than twice that of common high explosives and potentially faster combustion kinetics than bulk metals. The tetrameric aluminum cluster $Al_4Cp^*_4$ is a prototypical monovalent aluminum compound, and a potential precursor for these larger metalloid clusters. The synthesis of $Al_4R_4$ ( $R=C_5Me_4Pr$ , $C_5Me_4iPr$ ), two clusters similar to $Al_4Cp^*_4$ , was recently reported and the effect of their increased steric bulk is discussed here. Experimental results and density functional theory (DFT) analysis show that these clusters are enthalpically more stable than the $Cp^*$ variant, due primarily to non-covalent interactions (NCIs) across ligand groups. These NCIs show how ligand steric bulk can add stability to tetrameric clusters in addition to low-valent metal bonding. Similar calculations are performed on seven other homoleptic Cp-related clusters with varying levels of steric bulk. DFT results are used to predict monomer/tetramer equilibrium for all clusters and show trends counter to expectations regarding the role of ligand bulk. This equilibrium could be an important component in determining the viability of a cluster as a precursor for larger clusters.				
14. SUBJECT TERMS metalloid clusters, energetic material, monovalent aluminum clusters, DFT, ELF, QTAIM, explosives			15. NUMBER OF PAGES 113	
			16. PRICE CODE	
17. SECURITY CLASSIFICATION OF REPORT Unclassified	18. SECURITY CLASSIFICATION OF THIS PAGE Unclassified	19. SECURITY CLASSIFICATION OF ABSTRACT Unclassified	20. LIMITATION OF ABSTRACT UU	

THIS PAGE INTENTIONALLY LEFT BLANK

**Approved for public release. Distribution is unlimited.**

**LIGAND EFFECTS IN ALUMINUM CLUSTER-BASED ENERGETIC  
MATERIALS**

Warren W. Tomlinson  
Commander, United States Navy  
B.S., United States Naval Academy, 1998  
M.A., Air University, 2009

Submitted in partial fulfillment of the  
requirements for the degree of

**DOCTOR OF PHILOSOPHY IN APPLIED PHYSICS**

from the

**NAVAL POSTGRADUATE SCHOOL  
September 2017**

Approved by: Joseph Hooper  
Associate Professor of Physics  
Dissertation Supervisor

James Luscombe  
Professor of Physics

Ray Gamache  
Associate Professor of Physics

Dennis Mayo  
Research Chemist  
NSWC Indian Head

Todd Weatherford  
Professor of Electrical Engineering

Approved by: Kevin Smith, Chair, Department of Physics

Approved by: Douglas Moses, Vice Provost of Academic Affairs

THIS PAGE INTENTIONALLY LEFT BLANK

## ABSTRACT

This dissertation examines the electronic structure and thermochemistry of low-valent aluminum clusters that may serve as precursors for new energetic materials. Clusters such as  $\text{Al}_{50}\text{Cp}^*_{12}$  ( $\text{Cp}^* = \text{C}_5\text{Me}_5$ ) have theoretical heats of combustion more than twice that of common high explosives and potentially faster combustion kinetics than bulk metals. The tetrameric aluminum cluster  $\text{Al}_4\text{Cp}^*_4$  is a prototypical monovalent aluminum compound, and a potential precursor for these larger metalloid clusters. The synthesis of  $\text{Al}_4\text{R}_4$  ( $\text{R} = \text{C}_5\text{Me}_4\text{Pr}$ ,  $\text{C}_5\text{Me}_4\text{iPr}$ ), two clusters similar to  $\text{Al}_4\text{Cp}^*_4$ , was recently reported and the effect of their increased steric bulk is discussed here. Experimental results and density functional theory (DFT) analysis show that these clusters are enthalpically more stable than the  $\text{Cp}^*$  variant, due primarily to non-covalent interactions (NCIs) across ligand groups. These NCIs show how ligand steric bulk can add stability to tetrameric clusters in addition to low-valent metal bonding. Similar calculations are performed on seven other homoleptic Cp-related clusters with varying levels of steric bulk. DFT results are used to predict monomer/tetramer equilibrium for all clusters and show trends counter to expectations regarding the role of ligand bulk. This equilibrium could be an important component in determining the viability of a cluster as a precursor for larger clusters.

THIS PAGE INTENTIONALLY LEFT BLANK

## TABLE OF CONTENTS

I.	INTRODUCTION .....	1
A.	BACKGROUND .....	1
1.	Combustion of Aluminum.....	3
2.	Low-Valent Aluminum Clusters.....	7
B.	DENSITY FUNCTIONAL THEORY .....	11
1.	Hartree-Fock Theory.....	12
2.	Density Functional Theory.....	13
3.	Basis Sets.....	17
C.	METHODOLOGY .....	18
II.	DFT ANALYSIS OF MONOVALENT ALUMINUM CLUSTERS.....	21
A.	TWO NEW CYCLOPENTADIENYL HOMOLEPTIC CLUSTERS .....	21
1.	Synthesis of $\text{Al}_4\text{Cp}^{*\text{Pr}}_4$ and $\text{Al}_4\text{Cp}^{*\text{iPr}}_4$ .....	22
2.	DFT Approach and Thermochemistry Results.....	23
3.	NMR Results.....	29
4.	Structural Analysis of $\text{Al}_4\text{Cp}^{*\text{Pr}}_4$ and $\text{Al}_4\text{Cp}^{*\text{iPr}}_4$ .....	32
B.	ANALYSIS OF THE $\text{CP}^{*\text{ET}}$ VARIANT AND OVERALL LIGAND TRENDS .....	37
C.	QUANTUM THEORY OF ATOMS IN MOLECULES ANALYSIS .....	39
D.	EQUILIBRIUM CONSTANT CALCULATIONS.....	47
III.	LARGER LIGAND VARIANTS .....	51
A.	EFFECTS OF ADDITIONAL STERIC BULK.....	51
1.	$\text{Al}_4(\text{C}_5\text{Me}_4\text{Ph})_4$ .....	51
2.	Other Isopropyl Variants.....	69
IV.	CONCLUSION .....	77
	APPENDIX A. COMPUTATIONAL METHODOLOGY .....	79
	APPENDIX B. ADDITIONAL PUBLICATIONS.....	81
	LIST OF REFERENCES.....	83
	INITIAL DISTRIBUTION LIST .....	93

THIS PAGE INTENTIONALLY LEFT BLANK

## LIST OF FIGURES

Figure 1.	Reaction times for RDX and aluminum powder and influence times for explosive effects. Adapted from [7].	2
Figure 2.	TNT equivalence of organic explosives and bulk aluminum.	3
Figure 3.	TEM image of aluminum particle showing aluminum oxide passivation layer. Source: [17].	5
Figure 4.	Aluminum particle quenched 2.5–3 milliseconds after ignition. Source: [18].	6
Figure 5.	Heat of combustion by mass of two organometallic clusters and two typical organic explosives.	8
Figure 6.	A to-scale depiction of a 25-nanometer diameter aluminum particle, $\text{Al}_{50}\text{Cp}^*_{12}$ and RDX.	9
Figure 7.	Large cluster synthesis approach.	10
Figure 8.	Electron density plot of $\text{Cp}^-$ anion.	14
Figure 9.	Monomers of three AIR ( $\text{R}=\text{Cp}^*$ , $\text{Cp}^{*\text{Pr}}$ , $\text{Cp}^{*\text{iPr}}$ ) variants.	21
Figure 10.	Synthesis of the $\text{Cp}^{*\text{Pr}}$ and $\text{Cp}^{*\text{iPr}}$ variants via salt metathesis and reductive elimination.	22
Figure 11.	Variable-temperature $^{27}\text{Al}$ NMR of $\text{Al}_4\text{Cp}^{*\text{Pr}}_4$ (a) in toluene- $d_8$ (100 mg in 0.8 mL; 302–347 K) and $\text{Al}_4\text{Cp}^{*\text{iPr}}_4$ (b) in toluene- $d_8$ (44.5 mg in 0.5 mL; 303–353 K).	23
Figure 12.	Difference of DFT calculated $\Delta H_{tet}$ values from experimental values for various functionals.	26
Figure 13.	Calculated vs. experimental chemical shifts using M06-2X/6-31G(d).	30
Figure 14.	Calculated chemical shifts using BP86/SVP.	31
Figure 15.	Type A (a) and type B (b) monomers for the $\text{Cp}^{*\text{Pr}}$ variant.	33
Figure 16.	Type A (a) and type B (b) tetramers for the $\text{Cp}^{*\text{Pr}}$ variant.	34
Figure 17.	Eight different isomers of the $\text{Cp}^{*\text{Pr}}$ tetramer, ordered by DFT energies.	35

Figure 18.	The lowest energy configuration for the Cp <sup>*iPr</sup> variant.....	36
Figure 19.	The lowest energy configuration for the theoretical Cp <sup>*Et</sup> variant.....	37
Figure 20.	Initial six variants investigated in order of increasing steric bulk. ....	38
Figure 21.	Plot of the norm of $\nabla\rho$ for the Cp <sup>-</sup> anion.....	40
Figure 22.	Inter-ligand H-H BCPs in the Cp <sup>*Pr</sup> variant (shown in red).....	40
Figure 23.	Inter-ligand H-C and H-H BCPs in the Cp <sup>*iPr</sup> variant (shown in red). ....	41
Figure 24.	Al-Al bond distance vs. total $\nabla\rho_b$ associated with Al-Al BCPs. ....	44
Figure 25.	$\Delta H_{tet}$ calculated via DFT frequency analysis compared to $\Delta H_{tet}$ calculated via equation (8). ....	46
Figure 26.	Monomer (a) and tetramer (b) of Cp <sup>*Ph</sup> <sub>4</sub> variant. ....	52
Figure 27.	Histogram of calculated energy for randomly created structures. ....	59
Figure 28.	Histogram of calculated energy for structures produced by GA. ....	59
Figure 29.	Logarithmic plot of normalized monomer/tetramer ratio for seven different Cp variants. ....	62
Figure 30.	ELF for AlCp monomer with the 0.75 isosurface displayed. ....	64
Figure 31.	ELF for aluminum core of six Cp-type variants with the 0.79 isosurface displayed. ....	65
Figure 32.	Three ELF isosurface values illustrating bifurcation.....	66
Figure 33.	ELF 0.06 isosurface showing NCI between hydrogen and oxygen atoms in a $\beta$ -turn of amino acids.....	68
Figure 34.	ELF 0.03 isosurface showing inter-ligand connection (red circle) and intra-ligand connections (green circles) of domains in Cp <sup>*Ph</sup> variant.....	69
Figure 35.	Lowest energy configuration of the AlCp <sup>3iPr</sup> monomer.....	70
Figure 36.	ELF for aluminum core of the Cp <sup>3iPr</sup> tetramer with the 0.79 isosurface displayed .....	71
Figure 37.	Lowest energy configuration of the AlCp <sup>4iPr</sup> monomer.....	72
Figure 38.	ELF for aluminum core of the Cp <sup>4iPr</sup> tetramer. ....	73

Figure 39.	Lowest energy configuration of the $\text{AlCp}^{5\text{Pr}}$ monomer.....	74
Figure 40.	Logarithmic plot of monomer/tetramer equilibrium ratios for $\text{Cp}$ , $\text{Cp}^*$ , $\text{Cp}^{*\text{Ph}}$ , $\text{Cp}^{3\text{iPr}}$ and $\text{Cp}^{4\text{iPr}}$ variants.....	75

THIS PAGE INTENTIONALLY LEFT BLANK

## LIST OF TABLES

Table 1.	Calculated average lengths for $\text{Al}_4\text{Cp}^*$ .....	25
Table 2.	Calculated length differences from experiment for $\text{Al}_4\text{Cp}^*$ .....	25
Table 3.	Heats and entropies of tetramization for the $\text{Cp}^*$ , $\text{Cp}^{*\text{Pr}}$ and $\text{Cp}^{*\text{iPr}}$ variants using various DFT functionals. ....	27
Table 4.	Heats and entropies of tetramization for the $\text{Cp}^*$ , $\text{Cp}^{*\text{Pr}}$ and $\text{Cp}^{*\text{iPr}}$ variants using M06-2X and various basis sets. ....	28
Table 5.	Heats of tetramization for the $\text{Cp}^*$ , $\text{Cp}^{*\text{Pr}}$ and $\text{Cp}^{*\text{iPr}}$ variants with added dispersion.....	29
Table 6.	Calculated $\Delta H_{tet}$ including basis set superposition error correction for all variants. ....	29
Table 7.	Difference of calculated $^{27}\text{Al}$ NMR chemical shifts from experiment. ....	32
Table 8.	Topological average BCP metrics for all variants. ....	42
Table 9.	Al-Al bond distances and total electron density at BCPs for eight cluster variants. ....	43
Table 10.	Total electron density at Al-Al, H-H and H-C BCPs for various clusters. ....	45
Table 11.	Experimental and calculated equilibrium constants at 298.15K.....	49
Table 12.	Average Al-Al distance and $\rho_b$ for the $\text{Cp}^{*\text{Pr}}$ and $\text{Cp}^{*\text{Ph}}$ variants.....	61

THIS PAGE INTENTIONALLY LEFT BLANK

## LIST OF ACRONYMS AND ABBREVIATIONS

ASE	Atomic Simulation Environment
BCP	bond critical point
BO	Born-Oppenheimer
BSSE	basis set superposition error
CL-20	hexanitrohexaazaisowurtzitane, $C_6N_{12}H_6O_{12}$
COSMO	conductor-like screening model
Cp	cyclopentadienyl, $C_5H_5$
Cp <sup>^</sup>	tetramethylcyclopentadienyl, $C_5Me_4H$
Cp <sup>*</sup>	pentamethylcyclopentadienyl, $C_5Me_5$
Cp <sup>*Et</sup>	tetramethylethylcyclopentadienyl, $C_5Me_4Et$
Cp <sup>*iPr</sup>	tetramethylisopropylcyclopentadienyl, $C_5Me_4iPr$
Cp <sup>*Ph</sup>	tetramethylphenylcyclopentadienyl, $C_5Me_4Ph$
Cp <sup>*Pr</sup>	tetramethylpropylcyclopentadienyl, $C_5Me_4Pr$
Cp <sup>3iPr</sup>	triisopropylcyclopentadienyl, $C_5H_2iPr_3$
Cp <sup>4iPr</sup>	tetraisopropylcyclopentadienyl, $C_5HiPr_4$
Cp <sup>5iPr</sup>	pentaisopropylcyclopentadienyl, $C_5iPr_5$
DFT	density functional theory
DOD	Department of Defense
DTTO	di-1,2,3,4-tetrazine tetraoxide
ELF	electron localization function
EODTD	Explosive Ordnance Disposal Technical Division
Et	ethyl, $CH_2CH_3$
GA	genetic algorithm
GGA	generalized gradient approximation
GIAO	gauge-independent atomic orbital
HF	Hartree-Fock
HMX	octogen, $C_4H_8N_8O_8$
HPC	high performance computing
iPr	isopropyl, $CH(CH_3)_2$
KS	Kohn-Sham

LCAO	linear combination of atomic orbitals
LDA	local density approximation
Me	methyl, CH <sub>3</sub>
NAWC	Naval Air Warfare Center
NCI	non-covalent interaction
NMR	nuclear magnetic resonance
NSWC	Naval Surface Warfare Center
PAW	projector augmented wave
PCM	polarizable continuum model
Ph	phenyl, C <sub>6</sub> H <sub>5</sub>
ppm	parts per million
Pr	propyl, CH <sub>2</sub> CH <sub>2</sub> CH <sub>3</sub>
QTAIM	quantum theory of atoms in molecules
RDX	hexogen, C <sub>3</sub> H <sub>6</sub> N <sub>6</sub> O <sub>6</sub>
SD	Slater determinant
TEM	transmission electron microscope
TNT	trinitrotoluene, C <sub>6</sub> H <sub>2</sub> (NO <sub>2</sub> ) <sub>3</sub> CH <sub>3</sub>

## ACKNOWLEDGMENTS

First and foremost, I would like to thank Dr. Joseph Hooper. He was instrumental in helping me learn the very challenging topic of density functional theory (DFT). Despite completing all required Ph.D. coursework, I had never even heard of the term DFT. Dr. Hooper channeled Mr. Miyagi from the Karate Kid to help me learn DFT. There was quite a bit of “paint the fence” and “wax the car.” I had very little idea what I was doing with DFT, but nonetheless, Dr. Hooper was helping me build a foundation for eventually understanding DFT. Before long, things began to click and that is when my research really took off.

I would like to thank Dr. Dennis Mayo for teaching this physicist the basics of chemistry. I appreciate his patience as I’m sure he felt, at times, that he was dealing with an inexperienced undergraduate student. I never expected to have to learn as much chemistry as I did in the pursuit of my Ph.D. in applied physics, and if it weren’t for Dennis, I never would have gotten there.

I would also like to thank Dr. Bill Colson, Dr. Keith Cohn and Dr. Joseph Blau for their guidance during the qualifier stage of my Ph.D. work. They collectively served as my advisors until Dr. Colson retired shortly after my successful oral examination. All three spent hours and hours of their time ensuring I was prepared for both written and oral qualifiers. For their help, I am grateful.

I would also like to thank Dr. David Wolfe and Blake McCracken for their assistance in completing our very challenging Ph.D. big five courses. I’m not sure I would have ever been able to complete all the work we were given if it was not for their help. Because there were three of us, we usually only had to stare at a problem from Dr. Larraza for about three days before one of us would eventually have an epiphany and get the first step.

I would especially like to thank Dr. Daphne Kapolka for believing that I could be successful in a Ph.D. program. I found Dr. Kapolka’s number from the NPS catalog and called her out of the blue to ask her if I could study physics at NPS if I enrolled in the

Undersea Warfare Curriculum. As a Hornet pilot, this was not the ideal curriculum for me, but it was my only option. Dr. Kapolka was not in the least bit daunted and assured me that she could help me make it happen. After being at NPS for less than a quarter, I told Dr. Kapolka that I wanted to pursue a Ph.D. in physics. Again, she did not flinch. She helped rally support for my eventual application as a Permanent Military Professor and I was ultimately selected.

I would like to thank the Office of Naval Research. This work was supported by their Multidisciplinary University Research Initiative grant number N0001417WX00357, supervised by program managers Clifford Bedford, Kenny Lipkowitz and Chad Stoltz.

Finally, I would like to thank my family. I would like to thank my mother for her support my entire life and for never having any doubt that I could do anything I wanted to. I would like to thank my sister for the same, as well as her family and my wife's family for always being there when my wife and I needed any assistance throughout this long journey. Most importantly, I would like to thank my wife, Amy, and our beautiful children, Alex and Katie. Amy made sure my work absolutely came first despite her own career and the requirements which come with managing a household with small children. For her support and patience, I will always be grateful. Katie made sure I never had a bad day. No matter how bad things went, I was always happy as long as I could get my daily snuggles from Katie. Alex, in his own way, reminded me of the gravity of what I was doing. After watching a clip of my defense, he looked at me and asked, "Daddy, how did you get so smart?" Being extremely excited himself about entering the first grade, he then said, "Daddy, you must be in about the 20<sup>th</sup> grade." Not any more, Alex, not any more.

# I. INTRODUCTION

## A. BACKGROUND

The addition of aluminum particles to high explosives is a common method of improving overall energy production and can enhance blast effects [1]. PBXN-109, for example, is a common general purpose high explosive that is composed of a mix of hexogen (RDX), aluminum, binder and plasticizer. The addition of aluminum to an explosive formulation generally increases the overall blast impulse, but reduces detonation velocity and pressure [2]. To understand the contribution aluminum makes to the improvement of high explosives, a brief overview of detonation is necessary.

Detonation is a process involving a supersonic pressure wave perpetuated by an ongoing chemical reaction. For example, the decomposition of RDX into  $N_2$ ,  $H_2O$ ,  $CO$  and  $CO_2$  releases thousands of kilojoules of energy per mole, creating heat and pressure that will perpetuate the chemical reaction and can drive metal, a blast wave or otherwise do work external to the explosive. The detonation wave moves several kilometers per second and is driven by a reaction zone that is on the order of a few millimeters or less in width [3]. Only energy released inside the reaction zone will contribute to detonation wave propagation and its peak pressure. This requires the reaction time of the high explosive to be less than a microsecond—otherwise the detonation wave and reaction zone will pass over the molecule before it has had time to release energy. Aluminum burns too slowly to contribute to the detonation wave, though depending on the confinement of the charge, post-detonation combustion of aluminum can still contribute to brisance [4]. The ignition time for aluminum varies depending on the size and type of particle, but is on the order of just under a millisecond to tens of milliseconds for typical micrometer to nanometer scale particles included in explosive formulations [5], [6]. By the time the aluminum particles have ignited, the reaction zone has passed. For this reason, aluminum is generally treated as an inert material from a detonation perspective. Figure 1 shows reaction times for RDX and a typical micrometer-sized aluminum powder compared to the reaction times required to influence key capabilities of a high explosive.

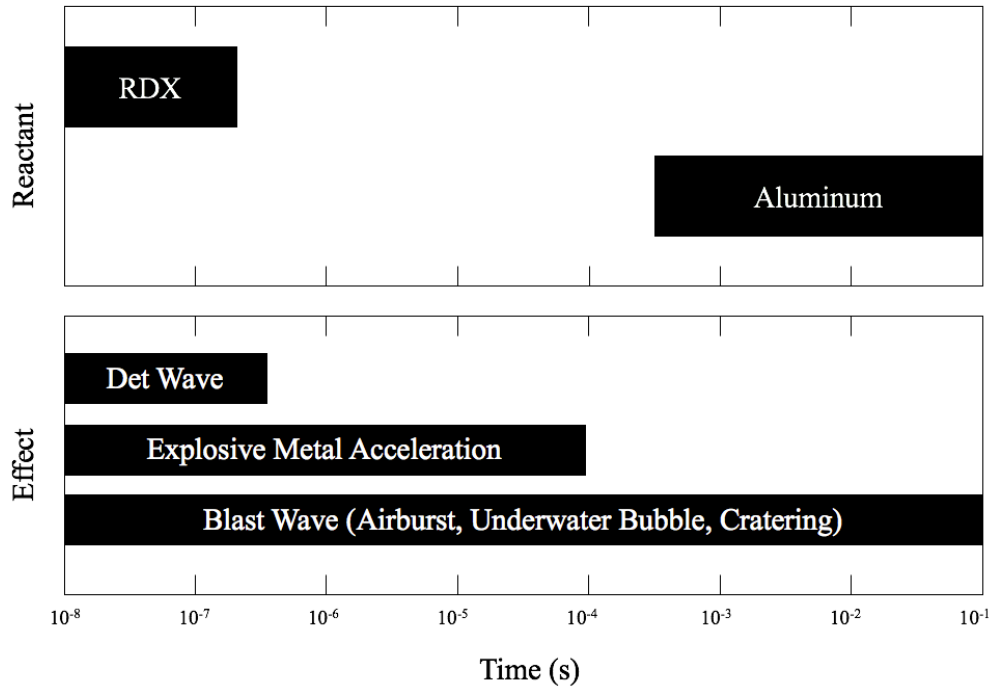
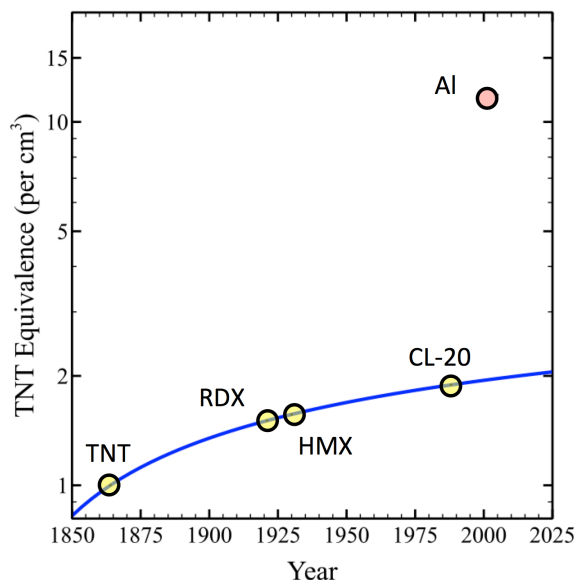


Figure 1. Reaction times for RDX and aluminum powder and influence times for explosive effects. Adapted from [7].

Even though aluminum does not help sustain a detonation wave, it is still commonly added to the current stock of military-grade high explosives like RDX, octogen (HMX) and hexanitrohexaazaisowurtzitane (CL-20). The aluminum typically contributes to blast effects and has a relatively high energy density. Despite more than a century of development, the energy density of high explosives has improved slowly. Figure 2 shows a rough progression from trinitrotoluene (TNT) to CL-20, the most powerful commodity high explosive in wide scale production [8]. TNT equivalence for the organic compounds was determined by the chemical equilibrium code Cheetah and compares total energy released by detonation. Also shown is bulk aluminum. For aluminum, the total energy release by detonation for TNT is compared to the heat of combustion of aluminum metal oxidized to form aluminum oxide ( $\text{Al}_2\text{O}_3$ ),  $83 \text{ kJ/cm}^3$  [9]. This represents a theoretical maximum energy release for aluminum with infinitely available oxidizer, and shows the tremendous potential of metalized explosives.



Explosives are listed based on the year they were first synthesized.

Figure 2. TNT equivalence of organic explosives and bulk aluminum.

Reducing the timescale of aluminum reaction would represent a significant advance in high explosive development, allowing the high energy density of the metal to be incorporated into detonation and metal-throwing effects. While new organic explosives (e.g., octanitrocubane [10] and di-1,2,3,4-tetrazine tetraoxide (DTTO) [11], [12]) still hold promise for significant improvements in organic explosive performance, their total energy density is unlikely to approach that of heavily aluminized formulations [13]. If the kinetics of the aluminum combustion can be rapid enough to react in or close to the reaction zone, significant enhancements beyond organic explosives could be realized.

### 1. Combustion of Aluminum

Aluminum is a group 13 metal with a natural oxidation state of +3. It exists naturally in minerals in the +3 oxidation state and the pure metal form is only obtained through industrial processes. Bulk aluminum readily reacts with oxygen forming the ceramic  $\text{Al}_2\text{O}_3$  releasing about 31 kJ/g of energy [14]. By comparison, 1 gram of CL-20 releases about 8 kJ/g of energy [15]. Because of the increased energy density of

aluminum compared to organic explosives, it is routinely used as an energetic additive in many explosive compounds. Typically, aluminum is added in the form of small manufactured particles ranging in size from about 100 nanometers to a few hundred microns. Their relatively long ignition time and burn time, however, prevent the energy released during oxidation from participating in the detonation reaction.

A typical aluminum micro-particle is not purely bulk aluminum. Though usually synthesized in an argon atmosphere, particles are eventually exposed to air. Once exposed, the surface of a particle will immediately oxidize and produce a thin ceramic shell around the interior aluminum known as a passivation layer. The thickness of the passivation layer varies, but is usually around a few nanometers. Figure 3 shows a transmission electron microscope (TEM) image for a roughly 100-nanometer diameter aluminum particle. The passivation layer represents the first barrier to efficient combustion of an aluminum particle. Before the bulk aluminum core of a particle can be oxidized, the oxidizer must penetrate the aluminum oxide shell. This is generally accomplished in one of two ways: either by the diffusion of the oxidizer and aluminum metal through the heated aluminum oxide shell, or due to the fracturing of the aluminum oxide shell as a result of the expansion of the expanding, molten aluminum core. Regardless of the mechanism, delay in the ignition of the aluminum particle will result. This delay depends on a number of factors, but at its shortest is just under a millisecond [6]. This delay is sufficient to prevent aluminum oxidation from participating in the detonation process. Efforts to passivate aluminum with something other than aluminum oxide are ongoing and success has been achieved in the area of self-assembled monolayers [16]. Jouet et al. successfully produced organic-coated, oxide-free aluminum nanoparticles that were air stable [16]. While this approach potentially removes a barrier to ignition of aluminum particles, it reduces the overall aluminum content compared to traditionally passivated aluminum particles. This is because the molar mass of the passivation agents used are 25–30 times greater than that of bulk aluminum [16].

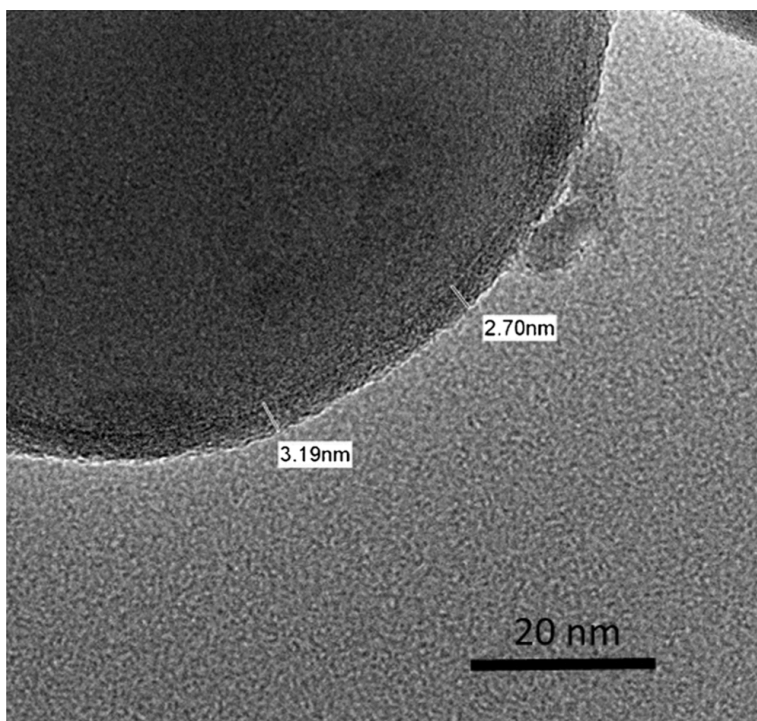


Figure 3. TEM image of aluminum particle showing aluminum oxide passivation layer. Source: [17].

While production of oxide-free aluminum particles would reduce ignition times and potentially provide an oxidizing agent for the aluminum, there is a second barrier to efficient burning of bulk aluminum. The boiling point of aluminum oxide is about 500 K higher than that of aluminum. During particle combustion, gas-phase aluminum and oxygen gas create aluminum oxide. The aluminum oxide tends to condense and form a cap which attaches to the remaining aluminum in the particle [18]. This oxide cap further complicates and inhibits the combustion process and ultimately slows the burn rate of the particle. Figure 4 shows a 70-micrometer diameter aluminum particle about three milliseconds after ignition. The smooth structure on the right is aluminum oxide. This oxide cap prevents aluminum particles from combusting in a manner similar to hydrocarbon droplets, which have a burn time proportional to the diameter of the droplet squared. Efforts to model aluminum particle combustion are ongoing, but what is relevant to this work is that burn time is generally on the order of milliseconds. While burn times from aluminum microparticles have been measured in the hundreds of milliseconds,

Beckstead points out that the vast majority of the available energy is released within about the first five milliseconds [19]. Work by Dreizin corroborates this, showing that for 90 micrometer aluminum particles, burn times at 3,000 K were about 5–10 milliseconds [20]. Reducing particle size to the nanometer regime does improve burn times. Shock ignition of 100 nanometer aluminum particles had burn times of just under 600 microseconds [6]. This is almost ten times faster than a typical micron-sized particle, but still significantly slower than the reaction time of a molecule like RDX, less than one microsecond. There is a drawback to using small, nanometer-sized particles, however. As size decreases, the aluminum oxide passivation layer makes up a larger and larger percentage of the total mass of the particle. The impact varies depending on the manufacturing process and the age of the particle, but in general, particles less than about 50 nanometers are composed of no more than about 40% of aluminum by mass [16].

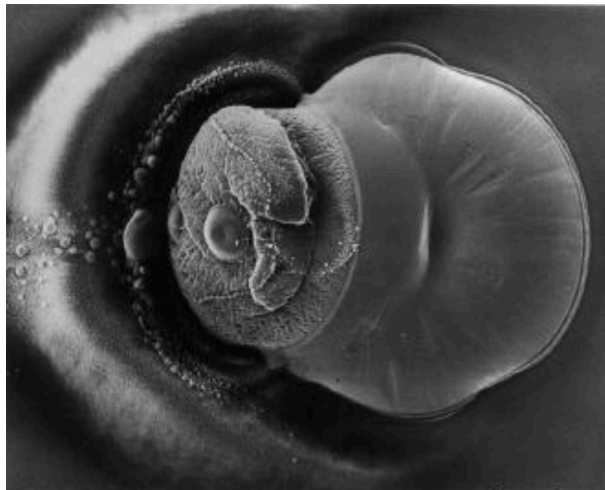


Figure 4. Aluminum particle quenched 2.5–3 milliseconds after ignition.  
Source: [18].

Typical aluminum particles used in explosive compounds ignite and burn long after the detonation wave has passed. Even advances in aluminum particle production, like size reduction and reduction or even elimination of the passivation layer, still put energy release 2–3 orders of magnitude too slow to contribute to detonation wave propagation. Additionally, these ignition and burn time calculations assume a readily

available supply of oxidizer, typically O<sub>2</sub>, in the gas phase. This is not likely to be the case when the particles are packed into an explosive compound. This work explores an alternative avenue to harnessing the full energetic potential of bulk aluminum. Ongoing research into small organometallic aluminum clusters has shown that clusters with large numbers of low valent aluminum atoms can be synthesized. While considerable synthesis challenges remain, their relatively small size and potential to include oxidizer within the surrounding ligands could allow them to oxidize on time scales similar to those of traditional organic explosives.

## 2. Low-Valent Aluminum Clusters

Monovalent aluminum clusters have received considerable attention in recent years, following the initial synthesis of the monovalent aluminum cluster Al<sub>4</sub>Cp\*<sub>4</sub> (Cp\* = C<sub>5</sub>Me<sub>5</sub>) [21]. Investigations on this and similar low valence aluminum clusters have continued; Al<sub>4</sub>Cp\*<sub>4</sub> has served as an aluminum atom source in the formation of nanoparticles, and AlCp\* units have proven to be an efficient ligand in many transition metal complexes [22]–[25]. Larger clusters with a significant number of low-valence aluminum atoms have also been investigated [26]–[30]. These systems are of interest for a variety of applications, including use as energetic material [31]. The unique structure of these clusters, with aluminum atoms in the central core surrounded by organic ligands, may allow for fast metal combustion kinetics while avoiding the rapid sintering and native oxide layer that limit traditional aluminum nanoparticle combustion [32]. The close proximity of exterior ligands to the low-valent metal core may offer opportunities for very rapid mass transfer between the metal and oxidizing functional groups on the ligand. The energetic potential of Al<sub>4</sub>Cp\*<sub>4</sub> and a similar, larger cluster, Al<sub>50</sub>Cp\*<sub>12</sub>, were shown to potentially have volumetric heats of combustion approaching 60% of bulk aluminum [31]. This is especially impressive considering the density of these clusters is less than half of that of bulk aluminum [31]. Figure 5 shows a comparison of calculated heats of combustion by mass of both compounds compared to RDX and a generic aluminized plastic bonded explosive, PBX.

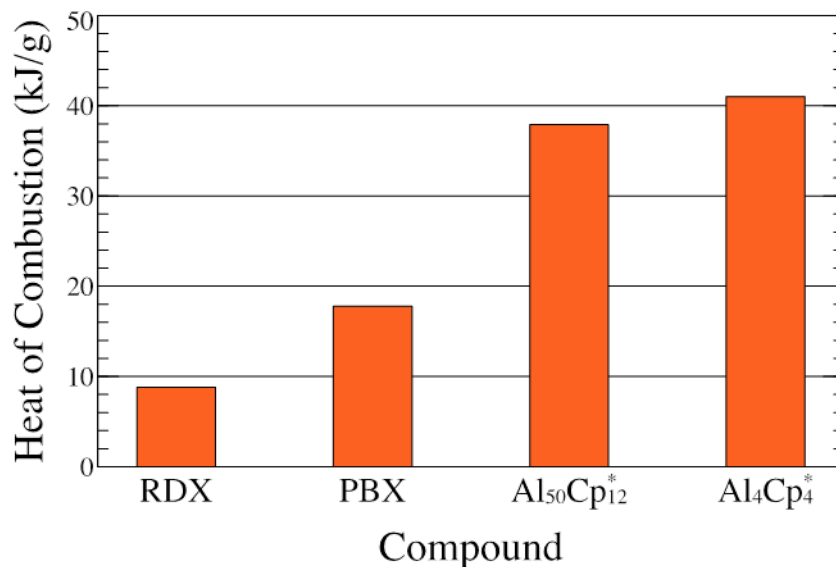


Figure 5. Heat of combustion by mass of two organometallic clusters and two typical organic explosives.

Compared to aluminum particles currently used in explosives, these low valent aluminum clusters are expected to burn significantly faster than traditional bulk metals. There is no oxide layer surrounding these particles and an oxidizer could potentially be integrated into the surrounding organic ligand. All that is between the aluminum core and the oxidizing agent is a stabilizing organic ligand, which is only a few bond lengths thick. Additionally, these clusters are significantly smaller than the smallest aluminum particles used in explosives. Figure 6 shows an aluminum nanoparticle with a diameter of 25 nanometers and an oxide layer three nanometers thick. The oxide layer represents about 56% of the total volume of the particle. To the right are to-scale depictions of Al<sub>50</sub>Cp<sup>\*</sup><sub>12</sub> and RDX. This visual demonstrates not only the increased impact of the oxide layer on small aluminum nanoparticles, but also the dramatic size difference between these particles and even large monovalent aluminum clusters.

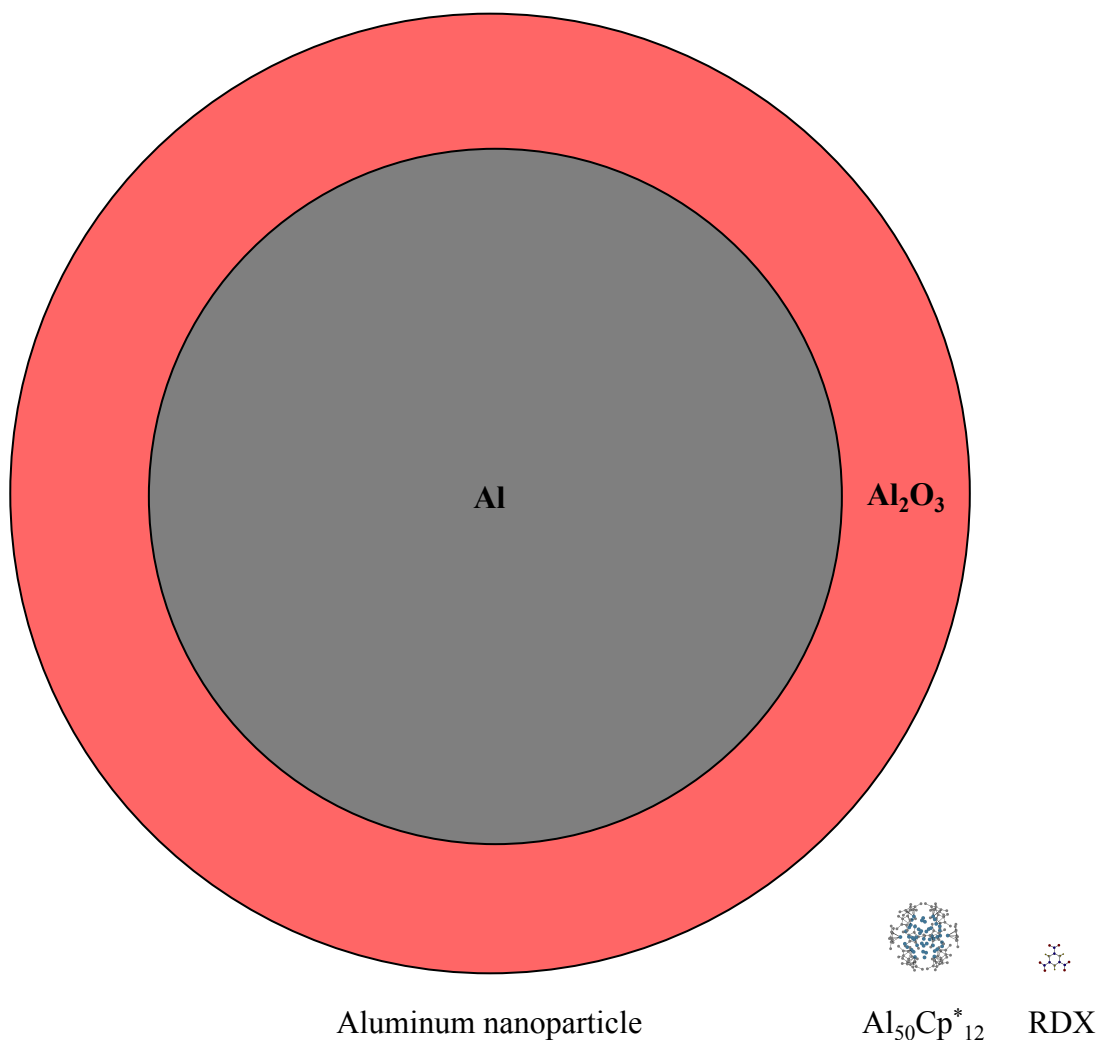


Figure 6. A to-scale depiction of a 25-nanometer diameter aluminum particle,  $\text{Al}_{50}\text{Cp}^*_{12}$  and RDX.

Currently there are seven synthesized and structurally characterized tetrameric clusters containing a tetrahedral, monovalent aluminum core [33]–[39]. Of these seven, only two are homoleptic complexes stabilized by a variant of the cyclopentadienyl ligand:  $\text{Al}_4\text{Cp}^*_4$  and  $\text{Al}_4\text{Cp}^{\wedge}_4$  ( $\text{Cp}^{\wedge}=\text{C}_5\text{Me}_4\text{H}$ ). The tetramer of the unsubstituted variant,  $\text{Al}_4\text{Cp}_4$  ( $\text{Cp}=\text{C}_5\text{H}_5$ ), has been observed in solution but never isolated [38]. Work on these clusters, as well as other low valence aluminum clusters, is ongoing; as the synthesis and isolation of these materials is difficult and the final products are often air-sensitive, density functional theory (DFT) analysis has been very helpful in understanding the behavior of

these clusters [40]–[46]. These tetrameric clusters are of importance because they represent potential precursors for larger metalloid clusters [47]. Of chief concern is the monomer to tetramer ratio of these clusters in equilibrium. A high ratio of monomers to tetramers is desired for a large cluster synthesis approach pursued by Curtis Johnson and David Morris at Naval Air Warfare Center (NAWC), China Lake. The approach takes advantage of two known reactions, shown in the top two positions in Figure 7. The bottom reaction in the Figure is the approach of Johnson and Morris [48]. The first reaction demonstrates the ability of the  $\text{AlCp}^*$  variant to react with the trivalent species,  $\text{AlCl}_2\text{H}$ . The second reaction demonstrates the ability of potassium graphite to reduce trivalent  $\text{AlCl}_2\text{H}$  to bulk aluminum metal. By using a low molar amount of potassium graphite, to prevent reduction of  $\text{AlCp}^*$  monomers and tetramers, the hope is that bulk metal produced by the reduction of  $\text{AlCl}_2\text{H}$  in combination with available  $\text{AlCp}^*$  monomers in solution will lead to large, metalloid clusters analogous to  $\text{Al}_{50}\text{Cp}^*_{12}$ . A high ratio of monomers to tetramers for  $\text{Al}_4\text{Cp}^*_4$  and analogous compounds would provide more potential building blocks for larger clusters.

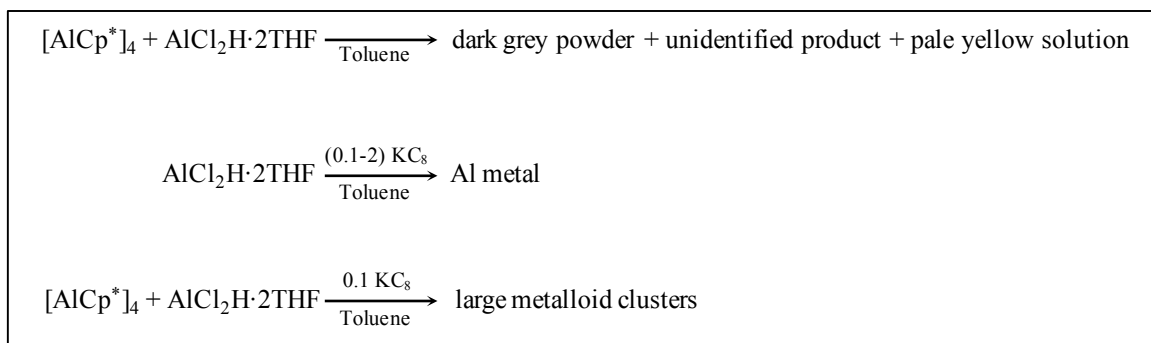


Figure 7. Large cluster synthesis approach.

Until recently, monomers in solution were only detectable for the  $\text{Cp}^*$  variant with a ratio of about one monomer for every 500 tetramers at room temperature. Two new aluminum clusters with substituted cyclopentadienyl ligands have been recently synthesized by Dennis Mayo and Rebecca Wilson at the Naval Surface Warfare Center (NSWC), Indian Head Explosive Ordnance Disposal Technical Division (EODTD), both with detectable monomers in solution. The properties of these new systems are

considered in great detail in following sections. Both clusters had monomer to tetramer ratios greater than the Cp\* variant. While these systems failed to crystallize and unambiguous structural data could not be obtained experimentally, a combination of variable-temperature  $^{27}\text{Al}$  nuclear magnetic resonance (NMR) experiments and DFT calculations described later strongly indicate these are tetrameric  $\text{Al}_4\text{Cp}^{*\text{Pr}}_4$  ( $\text{Cp}^{*\text{Pr}}=\text{C}_5\text{Me}_4\text{Pr}$ ) and  $\text{Al}_4\text{Cp}^{*\text{iPr}}_4$  ( $\text{Cp}^{*\text{iPr}}=\text{C}_5\text{Me}_4\text{iPr}$ ) and their respective monomers. These additional clusters provide key experimental thermochemical data that will ultimately help in developing a computational means of predicting monomer to tetramer ratio for theoretical tetrameric clusters. Computational approaches to electronic structure and thermochemistry analysis are varied, however, and different methodologies can lead to substantially different results. Before discussion of computational approaches to analyzing low-valence aluminum metalloids clusters, it is important to understand the origins and structure of modern DFT.

## B. DENSITY FUNCTIONAL THEORY

DFT provides an avenue for determining the ground state of a many electron system. In theory, exact solutions can be obtained, however in practice this is not the case. DFT has its roots in the Schrödinger equation which is analytically solvable for single electron systems, but becomes extremely complex for systems with even just a few electrons. For a system with  $n$  electrons and  $M$  nuclei the many-body Hamiltonian is:

$$\begin{aligned}\hat{H}_{BO} &= T_e + V_{eN} + V_{ee} + V_{NN} \\ &= -\frac{1}{2} \sum_{i=1}^n \nabla_i^2 - \sum_{i=1}^n \sum_{l=1}^M \frac{Z_l}{|\mathbf{r}_i - \mathbf{R}_l|} + \sum_{i=1}^n \sum_{j>i}^n \frac{1}{|\mathbf{r}_i - \mathbf{r}_j|} + \text{const.}\end{aligned}\quad (1)$$

Here we use atomic units where the mass of the electron, its charge,  $\hbar$  and  $4\pi\epsilon_0$  are all set to unity. The atomic unit of energy is called the Hartree and is  $\sim 27.21$  eV. This equation also makes use of the Born-Oppenheimer (BO) approximation which assumes the nuclei are motionless. This eliminates the kinetic energy term for the nuclei and will reduce the nuclei-nuclei potential to a constant. To determine the wave functions for the ground state of this system we need to solve the time-independent Schrödinger equation:

$$\hat{H}_{BO}\Psi(\mathbf{x}_1, \dots, \mathbf{x}_n) = E_0\Psi(\mathbf{x}_1, \dots, \mathbf{x}_n). \quad (2)$$

The vectors  $\mathbf{x}_i$  denote the coordinates of the  $i^{\text{th}}$  electron ( $\mathbf{r}_i$ ) as well as the spin of the  $i^{\text{th}}$  electron (up or down). This is a second order differential equation with  $4N$  variables. Exact solutions are beyond reach. A key property of the Hamiltonian, however, is that when it acts on the true wavefunction the lowest possible energy is produced. This allows the use of the variation principle where an initial guess of the wavefunction is continuously varied until the energy is minimized.

### 1. Hartree-Fock Theory

Hartree-Fock (HF) theory is an early attempt to arrive at the wavefunction of a many-body system developed in the 1920s and 1930s. HF theory makes use of a very simple guess for the structure of a many body wavefunction and then makes use of the variation principle to find an approximation of the actual wavefunction. First, the theory assumes that all electrons in the system are non-interacting. The wavefunction would then just be a combination of single-electron wavefunctions. Simply multiplying single electron wavefunctions together would not produce the anti-symmetry required for wavefunctions of fermions, so the appropriate form is a Slater determinant (SD):

$$\Psi_{SD}(\mathbf{x}_1, \dots, \mathbf{x}_n) = \frac{1}{\sqrt{n!}} \begin{vmatrix} \psi_1(\mathbf{x}_1) & \dots & \psi_n(\mathbf{x}_1) \\ \vdots & \ddots & \vdots \\ \psi_1(\mathbf{x}_n) & \dots & \psi_n(\mathbf{x}_n) \end{vmatrix}. \quad (3)$$

The single electron wavefunctions,  $\psi_i$ , are called orbitals and make up an orthonormal set. When the three non-constant terms of  $\hat{H}_{BO}$ , Eq. (1), act on  $\Psi_{SD}$ , four terms are produced. The first two can readily be identified as the kinetic energy and the electron-nucleus interaction terms. The third and fourth terms are both associated with the two-particle summation that represents electron-electron interactions,  $V_{ee}$ . They are known as the Coulomb ( $J$ ) and exchange ( $K$ ) terms respectively. The reason both exist is purely a consequence of the antisymmetric nature of the Slater determinant [49].  $J$  represents the self-interaction of the electron density cloud and the potential is considered *local* [49], [50].  $K$  represents self-repulsion and the potential is considered *non-local* [49], [50]. Because all terms contain only combinations of single particle wavefunctions, they can be readily evaluated and the ground state energy calculated. The orbitals are then varied,

preserving their orthonormality, until the energy is minimized. Despite the simple initial guess at the true many particle wavefunction, HF theory can produce ground state energies that are as much as 99.9% accurate [50]. The energy the HF theory fails to capture is called correlation energy,  $E_C$ , and can be quite large for even relatively small molecules.

## 2. Density Functional Theory

DFT is an effort to improve upon the success of HF theory by finding a route to the ground state energy with only knowledge of the electron density,  $\rho(\mathbf{r})$ . In theory, all we need to fully determine  $\hat{H}_{BO}$  is knowledge of the number of electrons and the potential they are subject to. This potential is defined by the static positions of the atomic nuclei and the number of electrons can be determined by integration of  $\rho(\mathbf{r})$  over all space. Figure 8 shows a plot of  $\rho(\mathbf{r})$  for the  $\text{Cp}^-$  anion. The positions of the atomic nuclei can clearly be seen as cusps of  $\rho(\mathbf{r})$ . The cusps are related to the nuclear charge of the nucleus by the equation:

$$\lim_{r \rightarrow 0} \left[ \frac{\partial}{\partial r} + 2Z_A \right] \bar{\rho}(r) = 0, \quad (4)$$

where  $\bar{\rho}(r)$  is the spherical average of  $\rho(r)$  [49]. The electron density allows us to determine not only nuclei position, but also atomic charge.

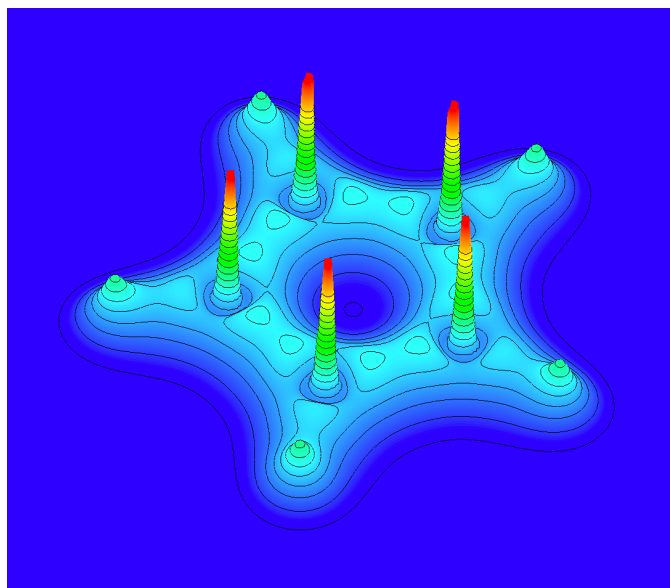


Figure 8. Electron density plot of  $\text{Cp}^-$  anion.

The final key element is a theorem by Hohenberg and Kohn which states that any ground state configuration of electrons is uniquely determined by the external potential [51]. Stated another way, a certain configuration of nuclei surrounded by a certain number of electrons will give rise to one and only one  $\rho(\mathbf{r})$ . That means there is a unique ground state energy and wavefunction associated with  $\hat{H}_{BO}$ , which we can get from  $\rho(\mathbf{r})$ . This is because  $\rho(\mathbf{r})$  can provide nuclear positions and charges, and integration of  $\rho(\mathbf{r})$  can provide the number of electrons. All the information we need to determine  $\hat{H}_{BO}$ , and therefore the ground state energy, must be available within the electron density and so there must be some energy functional  $E[\rho(\mathbf{r})]$  which produces the correct ground state energy if given the correct electron density. The problem is reduced from a  $4N$  dimensional second order differential equation to a functional with three special variables.

The form of this energy functional is not clear. The electron-nucleus interaction potential,  $V_{eN}$ , can be readily calculated from  $\rho(\mathbf{r})$ , but the kinetic energy and the electron-electron interaction potential cannot [50]. Ultimately the form of the energy functional is motivated from HF theory. About 80–90% of the electron-electron potential is captured in the HF term,  $J$ , which can be calculated from  $\rho(\mathbf{r})$  [50]. The kinetic energy

of non-interacting particles,  $T_S$ , is indirectly a functional of  $\rho(\mathbf{r})$  and is a large portion of the true kinetic energy [50]. The energy functional is then:

$$E[\rho] = T_S[\rho] + V_{eN}[\rho] + J[\rho] + E_{XC}[\rho] + V_{NN}, \quad (5)$$

where  $V_{NN}$  is the constant nucleus-nucleus potential and the exchange-correlation energy,  $E_{XC}[\rho]$ , is:

$$E_{XC}[\rho] = K[\rho] + E_C[\rho] + (T[\rho] - T_S[\rho]), \quad (6)$$

where  $K[\rho]$  is the HF exchange term and  $E_C[\rho]$  is the correlation energy, the energy missing from HF theory. The form of  $E_{XC}[\rho]$  is unknown, but if it was known then  $E[\rho]$  would be exact [49].

The best modern DFT can do is to continually create better and better approximations of  $E_{XC}[\rho]$ . The two most common approaches are based on a hypothetical uniform electron gas. The local density approximation (LDA) uses the known form of the exchange energy for a uniform electron gas and very accurate simulation data to motivate the remaining portion of  $E_{XC}[\rho]$  [49]. The resulting expression for  $E_{XC}[\rho]$  is then applied to each differential volume element of the actual (non-uniform) electron density and integrated to obtain the total exchange-correlation energy [50]. The generalized gradient approximation (GGA) improves upon LDA by including terms containing the gradient of the actual (non-uniform) electron density [49]. Attempts to improve upon GGA functionals with higher derivatives and kinetic energy terms has been tried as well. These functionals are called meta-GGAs [50]. Ultimately all of these approximations are theoretically motivated, but include empirical fitting parameters to try and produce the most accurate results [50]. They are also considered local. They attempt to represent  $E_{XC}[\rho]$ , which contains the non-local HF exchange energy,  $K$ , with expressions that only depend on the density and its gradient at a specific point [49].

In addition to LDA, GGA and meta-GGA, another approach that is common in thermochemistry calculations is the use of hybrid functionals. Hybrid functionals mix elements of HF theory with traditional DFT. The important element they include from HF theory is the exact exchange term,  $K$  [49]. The amount varies depending on the

formulation, but usually about 20–30% of exact exchange is included [49]. The inclusion of HF exchange adds a non-local element to the functional and the amount is controlled by one of several parameters that adjust all terms in the functional. These parameters are empirically determined in order to produce the best results for as broad a range of systems as possible.

While modern DFT has enjoyed great success, the accuracy of functionals is highly dependent on the type of system investigated. It is not appropriate to say that one particular functional is always more accurate than another, but in general GGAs are more accurate than LDAs and hybrids are more accurate than GGAs [49]. Of course, there are many types of functionals within each group and in some cases, for example, a GGA functional may perform better than a hybrid for a specific system. Once a particular functional is chosen, then the ground state energy of a specific system can be approximated using the variation principle.  $E[\rho]$  is ultimately a functional of electron density, but DFT is based on the Kohn-Sham (KS) approach which uses orbitals of individual electrons to calculate the electron density [52]. These orbitals, called Kohn-Sham orbitals, form a set,  $\{\varphi_i\}$ , and the electron density can be calculated by:

$$\rho(\mathbf{r}) = \sum_i^n |\varphi_i(\mathbf{r})|^2. \quad (7)$$

These KS orbitals are also used to directly calculate the kinetic energy of non-interacting particles. The orbitals, not the actual electron density, are varied to minimize the energy functional,  $E[\rho]$ . They are constructed from collections of functions called basis sets, discussed in the next section. Once the ground state energy and electron density are known, then all important properties of the system can be determined. For example, the first derivatives of the total energy with respect to nuclei perturbation provide a means for molecular geometry optimization [50]. The second derivatives of the total energy can yield vibrational frequencies from which thermochemical data can be calculated via statistical thermodynamics [49]. Mixed second derivatives of the total energy with respect to perturbations of nuclear magnetic moments provide a means for determining NMR chemical shifts [49]. The ability of DFT to determine these and many

other observables of chemical systems has made DFT an essential aspect of chemical analysis in general.

### 3. Basis Sets

The construction of KS orbitals is done through what is called the linear combination of atomic orbitals (LCAO). Initially, known eigenfunctions of the hydrogen atom were used to create basis sets [49]. Today there are four main approaches to constructing basis sets, but the most common for treatment of small molecules and clusters is through the use of Gaussian functions. KS orbitals are created through linear combinations of a set of these functions. If the set was complete, requiring an infinite number of functions, then the resulting orbitals would be exact. In practice, however, the set has a finite number of functions. The more functions in the set, the more accurately the KS orbitals can be described. This leads to the existence of several different sizes of sets. The minimum number of functions necessary to describe a KS orbital is one function for each atomic orbital including the valence orbitals. Carbon, for example, would require five functions, one for each of  $1s$ ,  $2s$ ,  $2p_x$ ,  $2p_y$  and  $2p_z$ . A *double-zeta* basis set would have two functions per atomic orbital; carbon would require ten functions. There are also triple, quadruple and higher zeta basis sets. To improve efficiency, split valence basis sets were created. A split valence double-zeta basis set would have one basis function for core atomic orbitals and two functions for each valence orbital. In this case carbon would require nine basis functions. It is also typical to include polarization functions within basis sets. Polarization functions represent the first unoccupied atomic orbitals of an atom; for carbon, these are the  $d$  orbitals. These functions help the KS orbitals distort appropriately in a molecular environment [49]. Just like DFT functionals, there are many types of basis sets that are of different sizes and constructed in slightly different ways. In general, the use of a triple-zeta basis set with polarization is sufficient to ensure resulting calculations represent the deficiencies of the chosen functional, rather than the basis set [50]. Basis sets of this size can be computationally expensive, however, so for large calculations it may be necessary to use smaller basis sets. Smaller basis sets may not be as accurate, but they can still produce meaningful results and capture trends.

## C. METHODOLOGY

The main goal of this work is to understand the thermodynamic properties and electronic structure of tetrameric, monovalent, aluminum clusters as a result of systematic changes in ligand steric bulk. Of particular interest is the ratio of monomers to tetramers in solution. Large concentrations of monomers are likely necessary for the further development of larger low-valent clusters such as  $\text{Al}_{50}\text{Cp}^*_{12}$  via the solution-based synthesis techniques previously discussed. Until recently, experimental thermodynamic data for monomer/tetramer equilibrium in small monovalent aluminum clusters was only available for the  $\text{Cp}^*$  variant via van 't Hoff analysis of variable-temperature  $^{27}\text{Al}$  NMR [38]. Tetramers of the  $\text{Cp}$  and  $\text{Cp}^\wedge$  variants have been observed in solution, but both disproportionate to trivalent aluminum species and bulk metal before AIR monomers are observed. DFT calculations show that  $\text{Cp}^{*\text{Pr}}$  and  $\text{Cp}^{*\text{iPr}}$  are bound into tetrameric forms more strongly than the  $\text{Cp}^*$  variant, despite the addition of steric bulk on the ligands.

DFT calculations were carried out to examine the electronic structure of these clusters and explore changes in bonding with the ligand variations. As would be expected, the calculated thermochemistry for these clusters is very sensitive to the computational methodology, especially the choice of the DFT functional. Previous calculations gave a wide range of results for tetramerization enthalpies and relative stabilities [31], [38]. The key challenge for these clusters is accurately capturing the dispersive forces present across ligand groups as well as the Al-Al bond behavior in the core. The clusters are combinations of four separate monomers held together not only by aluminum lone pair overlap in the core [31], but also by NCIs across neighboring ligand groups. Because these forces occur over relatively long distances, LDA, GGA and meta-GGA functionals, which are considered local, are severely deficient in capturing the effects [53]. Hybrid functionals, which include the non-local exchange from HF theory are better options, but in general they still cannot reliably describe dispersion [53]. Explicit dispersion corrections can be calculated by adding terms to the KS energy functional that capture the energy due to two and three body interactions. A common approach was developed by Stefan Grimme, called D3 [54]. This method has been shown to be very effective, but it is also computationally expensive. Recently work by Zhao and

Truhlar produced a suite of functionals that are specifically parameterized to handle compounds with significant NCIs [55]. These so-called Minnesota functionals are, in general, not as accurate as D3, but they can perform very well for certain systems without the need for any additional computational effort. This is particularly true for compounds with hydrogen-bonding [56]–[59]. In fact, Grimme found that M06-2X, a hybrid Minnesota functional, performed better than B3LYP-D3, a hybrid functional with explicit D3 added, when benchmarking hydrocarbon reaction energies, which include chain, ring and cage compounds [60]. Explicit inclusion of D3 with M06-2X only produced modest improvements because M06-2X was already able to capture most of the dispersive effects [60]. Grimme also benchmarked M06-2X against the S66 and S66x8 data sets which specifically test performance for noncovalent interactions [61]. He found excellent performance using M06-2X for H-bonded complexes with very little improvement with the addition of D3 [61]. M06-2X ran into difficulty only when benchmarked against the S66x8 set which specifically tests long range dispersion effects by separating dimers beyond their equilibrium geometry [61]. Ultimately, M06-2X performs well for complexes involving short and medium range dispersion, which are the primary interactions in the isolated clusters of this study. It is important to point out that the success of M06-2X, or any other functional, will be highly dependent on the system analyzed. This is also true of the techniques that are designed to handle dispersion. While explicit D3 will more often than not provide more accurate results than M06-2X, this is not necessarily the case for every system [58]. In fact, recent work by Lu et al. has shown that M06-2X has proven to be very accurate in predicting thermodynamic properties and key structural metrics for the two variants with reported solid-state structures (the Cp\* and Cp<sup>^</sup> variants) [62]. Because of this and the computation expediency gained by not using explicit D3 corrections, the M06-2X functional was chosen as the primary workhorse for DFT analysis.

This computational approach was used to calculate the most stable isomers of the Cp<sup>\*Pr</sup> and Cp<sup>\*iPr</sup> tetramers in the absence of experimental crystallographic data. Further details on determining the lowest energy geometric configuration are discussed in II.A.4. Calculated enthalpy of tetramerization  $\Delta H_{tet}$  values for these isomers are within 3 kJ/mol

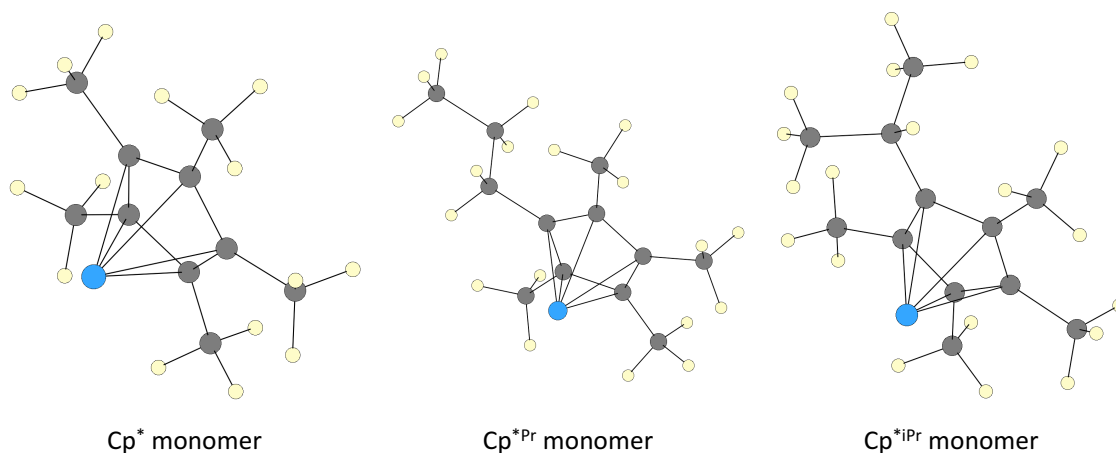
of the experimental values measured for the two new structures. Additionally, M06-2X is also very accurate in predicting  $^{27}\text{Al}$  NMR chemical shifts for a variety of low-valence aluminum clusters. Calculated chemical shifts for  $\text{Cp}^{*\text{Pr}}$  and  $\text{Cp}^{*\text{iPr}}$  tetramers are both within 9 parts per million (ppm) of the signals measured for the two new structures. This strongly suggests that the two new structures are indeed  $\text{Cp}^{*\text{Pr}}$  and  $\text{Cp}^{*\text{iPr}}$  tetramers. The M06-2X functional was also used to examine the thermodynamic properties for the other three Cp-type variants; analysis suggests that the Cp variant has a significantly lower tetramerization enthalpy compared to the other four variants, despite previous DFT work showing the opposite trend [38].

A detailed analysis of bonding was conducted in the context of the Quantum Theory of Atoms in Molecules (QTAIM) theory. This analysis shows the importance of NCIs between the ligands. While increased ligand bulk can result in increased Al-Al separation and a reduction in metal-metal bonding in the core, this is often offset by weak interactions between adjacent ligand groups. The tetramerization enthalpies arise from a balance of lone-pair overlap between monovalent aluminum atoms and non-covalent ligand interactions; this balance is challenging for DFT functionals to capture accurately. Finally, using thermodynamic data calculated using M06-2X, monomer/tetramer equilibrium constants can be calculated for the five existing homoleptic Cp-type variants as well as five theoretical variants with varying levels of steric bulk.

## II. DFT ANALYSIS OF MONOVALENT ALUMINUM CLUSTERS

### A. TWO NEW CYCLOPENTADIENYL HOMOLEPTIC CLUSTERS

It has been challenging to find a reliable computational method for monovalent aluminum cluster thermochemistry using ab initio methods, due in large part to a lack of experimental data and the difficult synthesis of new clusters of this type. Experimental structural data is only available for the  $\text{Cp}^*$  and  $\text{Cp}^*$  tetramers and the larger  $\text{Al}_{50}\text{Cp}^*_{12}$ , and until now experimental thermochemistry data was only available for the  $\text{Cp}^*$  variant. Based on calculated  $^{27}\text{Al}$  NMR chemical shifts and  $\Delta H_{tet}$  values for  $\text{Al}_4\text{Cp}^{*Pr}_4$  and  $\text{Al}_4\text{Cp}^{*iPr}_4$  it is assumed that experimental values observed for the two new structures are indeed  $\text{Cp}^{*Pr}$  and  $\text{Cp}^{*iPr}$  tetramers, providing two additional data points for validating the computational accuracy. Additionally, these two compounds are important because of their increased ligand steric bulk as compared to the  $\text{Cp}^*$  variant. Monomers of all three variants are shown in Figure 9. The two main goals of this thesis are to demonstrate the effectiveness of M06-2X in describing the properties of tetrameric cyclopentadienyl aluminum clusters in general and to investigate the effect of varying ligand bulk for these clusters.



The aluminum (blue) is positioned on a line perpendicular from the middle of the carbon (grey) ring.

Figure 9. Monomers of three AIR ( $R=\text{Cp}^*$ ,  $\text{Cp}^{*Pr}$ ,  $\text{Cp}^{*iPr}$ ) variants.

## 1. Synthesis of $\text{Al}_4\text{Cp}^{*\text{Pr}}_4$ and $\text{Al}_4\text{Cp}^{*\text{iPr}}_4$

The synthesis and solution equilibrium of the  $\text{Cp}^{*\text{Pr}}$  and  $\text{Cp}^{*\text{iPr}}$  variants was carried out by Dennis Mayo and Rebecca Wilson, researchers at the NSWC, Indian Head EODTD. The new cyclopentadienyl aluminum derivatives were prepared via thermally-activated reductive elimination of tetramethyl(alkyl)cyclopentadiene from bis-(tetramethyl(R)cyclopentadienyl) aluminum hydride intermediates ( $\text{Al}(\text{C}_5\text{Me}_4\text{R})_2\text{H}$ , R = n-propyl or i-propyl) in toluene at 80 °C (see Figure 10) [63]. Higher temperature reactions were attempted, but decomposition products were observed in the  $^1\text{H}$  NMR spectrum when carried out above 80 °C. When held at room temperature, solutions of  $\text{Al}(\text{C}_5\text{Me}_4\text{R})_2\text{H}$  in toluene or benzene are also in equilibrium as observed by  $^{27}\text{Al}$  NMR spectroscopy: a solution of  $\text{Al}(\text{C}_5\text{Me}_4^{\text{nPr}})_2\text{H}$  had an  $\text{Al}(\text{C}_5\text{Me}_4^{\text{nPr}})_2\text{H}:\text{Al}_4\text{Cp}^{*\text{Pr}}_4$  ratio of 65:35 after two weeks.

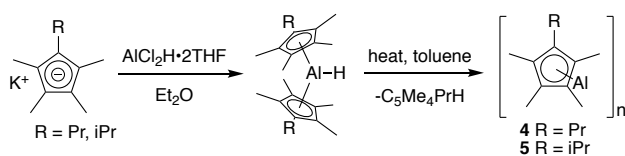


Figure 10. Synthesis of the  $\text{Cp}^{*\text{Pr}}$  and  $\text{Cp}^{*\text{iPr}}$  variants via salt metathesis and reductive elimination.

Reductive elimination of cyclopentadienes from  $\text{Al}(\text{C}_5\text{Me}_4\text{R})_2\text{H}$  was followed via  $^{27}\text{Al}$  NMR spectroscopy. The starting  $\text{Al}(\text{C}_5\text{Me}_4\text{R})_2\text{H}$  derivatives have diagnostic  $^{27}\text{Al}$  NMR signals around -30 ppm; the  $\text{Cp}^{*\text{Pr}}$  and  $\text{Cp}^{*\text{iPr}}$  oligomers, assumed to be tetramer forms, have  $^{27}\text{Al}$  signals at -86 and -89 ppm, respectively. For the  $\text{Cp}^{*\text{Pr}}$  variant, multiple cycles of heating followed by removal of the volatile components were necessary. For the  $\text{Cp}^{*\text{iPr}}$  variant, one heat/evaporation cycle was sufficient. The resultant yellow oils and solutions thereof failed to yield crystals suitable for single crystal x-ray analysis.

The resultant cyclopentadienylaluminum compounds were subjected to variable-temperature van 't Hoff analysis. Solutions of the  $\text{Cp}^{*\text{Pr}}$  and  $\text{Cp}^{*\text{iPr}}$  variants in toluene- $d_8$  were prepared and heated to 80 °C, the  $^{27}\text{Al}$  and  $^1\text{H}$  NMR spectra obtained, and the temperature lowered in 15 degree increments. Spectra are shown in Figure 11. Upon

heating, the monomer signal grows in intensity (-153 ppm for the Cp<sup>\*Pr</sup> variant, -150 ppm for the Cp<sup>\*iPr</sup> variant), showing a shift in the equilibrium towards monomeric species. The thermodynamic parameters were calculated assuming that the -86 and -89 ppm signals for Cp<sup>\*Pr</sup> and Cp<sup>\*iPr</sup> solutions corresponded to tetrameric forms; attempts to fit the data assuming monomer/dimer equilibrium resulted in considerably worse agreement. Additionally, DFT calculations found no stable dimer or trimer configurations of AlCp<sup>\*Pr</sup> or AlCp<sup>\*iPr</sup>. A dimer configuration of AlCp<sup>\*</sup> that was artificially frozen in place was calculated to have an NMR shift of -149 ppm, almost identical to that of the monomeric form. Thus, while larger oligomers cannot be ruled out, all data point to tetrameric Al<sub>4</sub>R<sub>4</sub> structures. For the Cp<sup>\*Pr</sup> variant, the enthalpy and entropy changes ( $\Delta H_{tet}$  and  $\Delta S_{tet}$ ) derived from this analysis are  $-160 \pm 3$  kJ/mol and  $-398 \pm 10$  J/mol·K, respectively. For the Cp<sup>\*iPr</sup> variant,  $\Delta H_{tet}$  and  $\Delta S_{tet}$  are  $-158 \pm 8$  kJ/mol and  $-477 \pm 25$  J/mol·K.

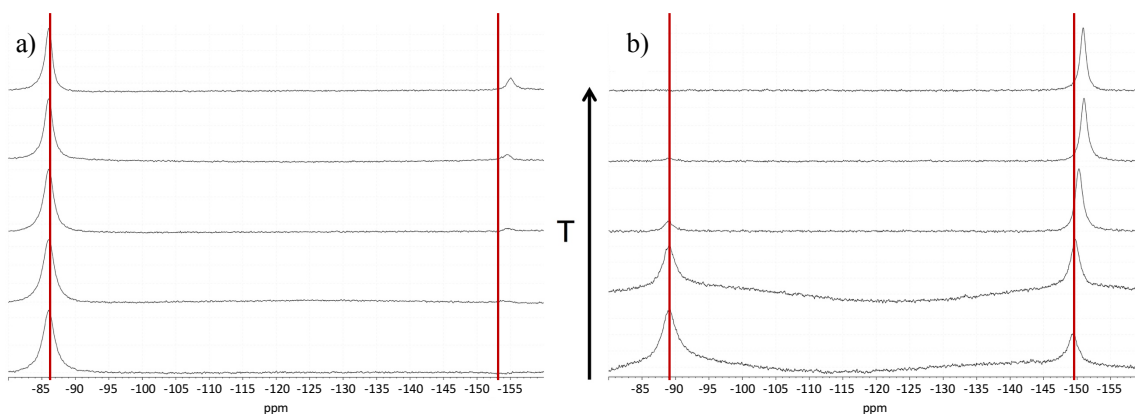


Figure 11. Variable-temperature <sup>27</sup>Al NMR of Al<sub>4</sub>Cp<sup>\*Pr</sup><sub>4</sub> (a) in toluene-*d*<sub>8</sub> (100 mg in 0.8 mL; 302–347 K) and Al<sub>4</sub>Cp<sup>\*iPr</sup><sub>4</sub> (b) in toluene-*d*<sub>8</sub> (44.5 mg in 0.5 mL; 303–353 K).

## 2. DFT Approach and Thermochemistry Results

The choice of DFT functional is critical regardless of the type of system under study. Previous theoretical treatment of these clusters has produced a range of different results. DFT calculations by Schnöckel and co-workers [38], [41] and Williams and Hooper [31] found that the Cp and Cp<sup>^</sup> tetramers are both much more stable enthalpically

against decomposition into monomers than the Cp\* tetramer. This seemed to be supported by the experimental fact that monomers of the Cp and Cp^ variants were not found via <sup>27</sup>Al NMR in solution, but that monomers of the Cp\* variant were found [38], [40]. While geometries and monomer enthalpies of formation were accurately predicted in these works, tetramerization enthalpies were in poor agreement with the experimental results available for the Cp\* variant. Additionally, new experimental thermochemistry data for the Cp\*<sup>Pr</sup> and Cp\*<sup>iPr</sup> variants showed both are more stable enthalpically than the Cp\* variant even though monomers of the Cp\*<sup>Pr</sup> and Cp\*<sup>iPr</sup> variants are found in solution. With this new experimental thermochemistry data available, an examination of the Cp\*, Cp\*<sup>Pr</sup> and Cp\*<sup>iPr</sup> variants was conducted with a range of functionals and basis sets to determine a computational approach that is accurate for both structural and thermochemical values. Since crystal structures do not exist for the Cp\*<sup>Pr</sup> and Cp\*<sup>iPr</sup> tetramers, multiple configurations of each were examined to determine the global minimum cluster structure and nearby isomers. That process is discussed later in this work.

Ten functionals [55], [64]–[74] were examined, all with a split valence double-zeta basis sets with polarization. This type of basis set was used for computational expediency. Included in this list are the two methods used in previous works on these clusters. The first is the method of Schnöckel which is the GGA functional BP86 paired with the split valence double-zeta basis set with polarization, SVP [38]. The second is the method of Williams and Hooper which is the hybrid functional B3LYP paired with the split valence double-zeta basis set with polarization, 6–31G(d,p) [31]. All functionals produce accurate results for key geometrical parameters such as the Al–Al distance and the Al–Cp ring-center distance. Structural parameters for all functionals are given in Table 1 and in general these predict key distances to better than 0.05 Å compared to solid-state x-ray data for the Cp\* tetramer. To get a clearer picture of overall functional performance, Table 2 shows the differences in calculated geometrical parameters from experimental ones. While all functionals perform well, M06-2X is the most accurate for three of the five metrics and is the second and third most accurate for the remaining two.

It is also important to note that M06-2X performs better than B3LYPD3, a hybrid functional with explicit dispersion corrections added, in all five metrics.

Table 1. Calculated average lengths for  $\text{Al}_4\text{Cp}^*_4$ .

Method	Al-Al	Al-C <sub>p</sub> center	Al-C <sub>ring</sub>	C <sub>ring</sub> -C <sub>ring</sub>	C <sub>ring</sub> -C <sub>Me</sub>
<b>EXPERIMENTAL</b>	<b>2.7670</b>	<b>2.0110</b>	<b>2.3450</b>	<b>1.4170</b>	<b>1.5000</b>
M062X/6-31G(d)	2.7672	1.9925	2.3313	1.4231	1.5003
BP86/SVP	2.8184	2.0570	2.3935	1.4386	1.5041
B3LYP/6-31G(d,p)	2.8541	2.0693	2.3994	1.4278	1.5029
B3LYPD3/6-31G(d,p)	2.7403	2.0295	2.3646	1.4268	1.5018
TPSSh/6-31G(d)	2.7802	2.0495	2.3830	1.4293	1.5037
PBEPBE/6-31G(d)	2.7989	2.0505	2.3865	1.4355	1.5030
PBE1PBE/6-31G(d)	2.7849	2.0273	2.3615	1.4239	1.4957
M06L/6-31G(d)	2.6765	1.9801	2.3214	1.4248	1.4920
mPW1PW91/6-31G(d)	2.7989	2.0367	2.3694	1.4235	1.4962
APFD/6-31G(d)	2.7234	1.9988	2.3370	1.4237	1.4968

\* All numbers are in angstroms.

Table 2. Calculated length differences from experiment for  $\text{Al}_4\text{Cp}^*_4$ .

Method	Al-Al	Al-C <sub>p</sub> center	Al-C <sub>ring</sub>	C <sub>ring</sub> -C <sub>ring</sub>	C <sub>ring</sub> -C <sub>Me</sub>
M062X/6-31G(d)	0.0002	0.0185	0.0137	0.0061	0.0003
BP86/SVP	0.0514	0.0460	0.0485	0.0216	0.0041
B3LYP/6-31G(d,p)	0.0871	0.0583	0.0544	0.0108	0.0029
B3LYPD3/6-31G(d,p)	0.0267	0.0185	0.0196	0.0098	0.0018
TPSSh/6-31G(d)	0.0132	0.0385	0.0380	0.0123	0.0037
PBEPBE/6-31G(d)	0.0319	0.0395	0.0415	0.0185	0.0030
PBE1PBE/6-31G(d)	0.0179	0.0163	0.0165	0.0069	0.0043
M06L/6-31G(d)	0.0905	0.0309	0.0236	0.0078	0.0080
mPW1PW91/6-31G(d)	0.0319	0.0257	0.0244	0.0065	0.0038
APFD/6-31G(d)	0.0436	0.0122	0.0080	0.0067	0.0032

\* All numbers are in angstroms.

Despite accurate geometrical results for all functionals, thermodynamic results are much more sensitive to functional. Figure 12 shows the strong variation of the tetramerization enthalpy ( $\Delta H_{tet}$ ) with functional type. All three experimental clusters were optimized with each functional until no imaginary frequencies were found. The

enthalpy and entropy for the tetramerization reaction were calculated from vibrational frequency analysis.

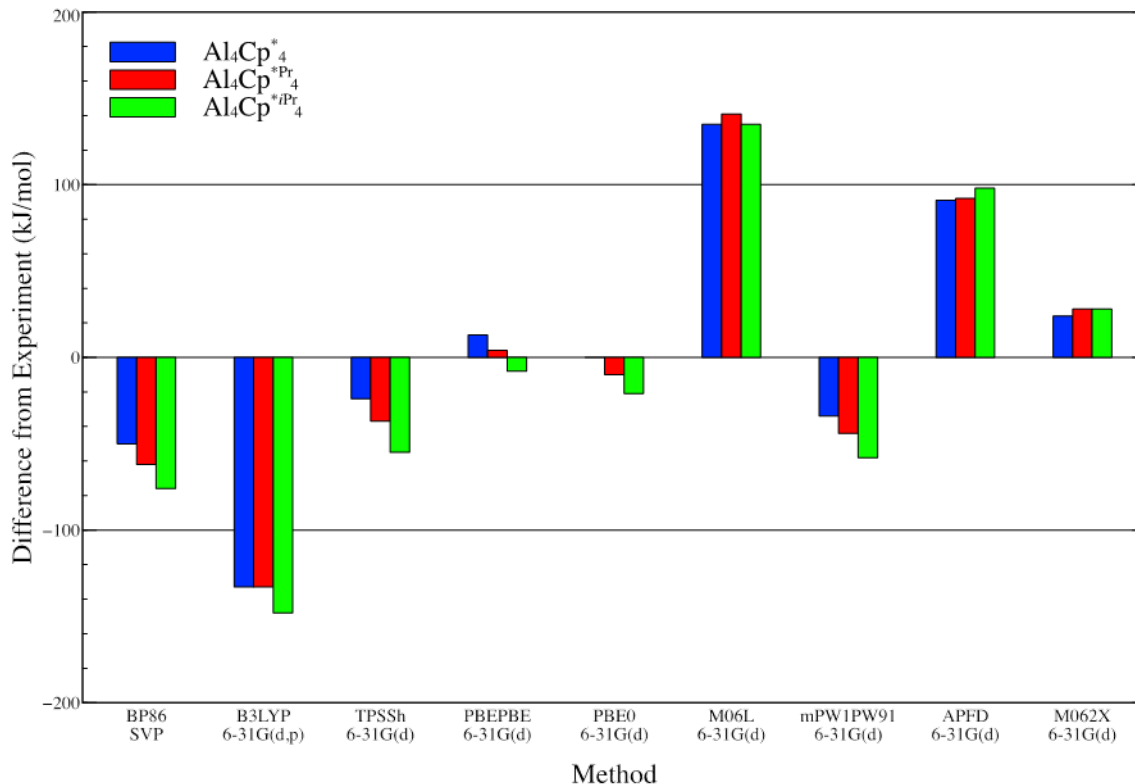


Figure 12. Difference of DFT calculated  $\Delta H_{tet}$  values from experimental values for various functionals.

Differences in  $\Delta H_{tet}$  between experiment and theory are as high as 130 kJ/mol, a value sufficient to make equilibrium rate calculations impossible. Additionally, for all but three functionals, the ordering of  $\Delta H_{tet}$  for the three variants differ from experiment. The Minnesota LDA functional, M06-L, and the hybrid functional, APFD, produce the correct relative ordering of tetramers, but both dramatically over-predict  $\Delta H_{tet}$  for all three structures. The third, M06-2X, has results much closer to experiment. While PBE, PBE0 and M06-2X all perform significantly better than the other methods tested, only M06-2X predicts the correct order of  $\Delta H_{tet}$  for all three variants. Capturing this trend is what is important, as the double-zeta basis set is not expected to be of high accuracy. The results for  $\Delta S_{tet}$  are more mixed. Two methods, BP86 and B3LYP get the order correct,

but the calculated result for the Cp\* variant is in error by over 100 J/mol·K. In general, it appears all tested methods have much higher errors for predicting  $\Delta S_{tet}$ . Numerical results for  $\Delta H_{tet}$  and  $\Delta S_{tet}$  are shown in Table 3. In detailed analysis to follow, enthalpy changes are relied on to validate predicted structures.

Table 3. Heats and entropies of tetramerization for the Cp\*, Cp\*Pr and Cp\*iPr variants using various DFT functionals.

Method	Al <sub>4</sub> Cp* <sub>4</sub>		Al <sub>4</sub> Cp*Pr <sub>4</sub>		Al <sub>4</sub> Cp*iPr <sub>4</sub>	
	$\Delta H_{tet}$	$\Delta S_{tet}$	$\Delta H_{tet}$	$\Delta S_{tet}$	$\Delta H_{tet}$	$\Delta S_{tet}$
<b>EXPERIMENTAL</b>	<b>-150</b>	<b>-0.300</b>	<b>-160</b>	<b>-0.398</b>	<b>-158</b>	<b>-0.477</b>
BP86/SVP	-100	-0.456	-98	-0.482	-82	-0.563
B3LYP/6-31G(d,p)	-17	-0.436	-27	-0.453	-10	-0.585
TPSSh/6-31G(d) <sup>1</sup>	-126	-0.523	-122	-0.496	-103	-0.577
PBEPBE/6-31G(d)	-163	-0.524	-164	-0.503	-150	-0.537
PBE1PBE/6-31G(d)	-150	-0.497	-150	-0.497	-137	-0.560
M06-L/6-31G(d)	-285	-0.564	-301	-0.533	-293	-0.665
mPW1PW91/6-31G(d)	-117	-0.526	-116	-0.514	-100	-0.544
APFD/6-31G(d)	-241	-0.532	-256	-0.613	-255	-0.633
M06-2X/6-31G(d)	-174	-0.649	-188	-0.679	-186	-0.657

\*  $\Delta H_{tet}$  numbers are in kJ/mol;  $\Delta S_{tet}$  numbers are in kJ/mol·K

To determine the sensitivity of basis set choice on thermodynamic calculations, the M06-2X functional was paired with eight different basis sets from Pople, Dunning and Ahlrichs [75]–[80]. The resulting thermodynamic calculations for  $\Delta H_{tet}$  and  $\Delta S_{tet}$ , in addition to experimental results for each of the three variants, are shown in Table 4. These results do not include two energy corrections required for these clusters. The first is basis set super position error (BSSE). BSSE corrects for artifacts that arise when molecular energy is calculated for an isolated monomer and a monomer bound in a cluster. The second is energy corrections due to the presence of the toluene solvent. Both

<sup>1</sup> Despite multiple techniques, the last imaginary vibrational frequency for the Cp\* variant's tetramer using TPSSh was not eliminated. Based on experience reducing negative vibrational frequencies from all other methods it was determined that the removal of a negative frequency corresponds to roughly a 2.5 kJ/mol reduction in  $\Delta H_{tet}$  and about a 0.150 kJ/mol·K reduction in  $\Delta S_{tet}$ . These corrections are not reflected in Table 3, but would not change our overall analysis of functional performance.

corrections were omitted for computational expediency. While there is not a systematic approach to accurate  $\Delta H_{tet}$  values with basis set size, the larger cc-pVTZ was chosen as the most accurate available method. Calculations of tetramers at the double zeta level typically required approximately 4000 CPU hours per system on a Department of Defense (DOD) High Performance Computing (HPC) cluster; increasing the basis size to cc-pVTZ required up to 25,000 CPU hours on the same machine. Calculations on larger clusters, such as  $Al_{50}Cp^*_{12}$ , were not viable at the triple zeta level with the available resources on DOD HPC systems. For this reason, and due to the ability of M06-2X/cc-pVTZ to predict  $\Delta H_{tet}$  to within 3 kJ/mol of experimental values for all variants when BSSE and solvent corrections are added, calculations beyond the triple zeta level of theory were not performed.

Table 4. Heats and entropies of tetramization for the  $Cp^*$ ,  $Cp^{*Pr}$  and  $Cp^{*iPr}$  variants using M06-2X and various basis sets.

Method	$Al_4Cp^*_4$		$Al_4Cp^{*Pr}_4$		$Al_4Cp^{*iPr}_4$	
	$\Delta H_{tet}$	$\Delta S_{tet}$	$\Delta H_{tet}$	$\Delta S_{tet}$	$\Delta H_{tet}$	$\Delta S_{tet}$
<b>EXPERIMENTAL</b>	<b>-150</b>	<b>-0.300</b>	<b>-160</b>	<b>-0.398</b>	<b>-158</b>	<b>-0.477</b>
M062X/6-31G(d)	-174	-0.649	-188	-0.679	-186	-0.657
M062X/6-31+G(d)	-168	-0.624	-182	-0.678	-180	-0.679
M062X/6-31G(d,p)	-181	-0.606	-193	-0.676	-189	-0.648
M062X/6-311G(d,p)	-172	-0.650	-188	-0.626	-187	-0.653
M062X/6-311+G(d,p)	-172	-0.658	-185	-0.635	-183	-0.650
M062X/Def2-TVZP	-173	-0.633	-183	-0.690	-179	-0.671
M062X/cc-pVDZ	-168	-0.610	-181	-0.666	-180	-0.658
M062X/cc-pVTZ	-167	-0.639	-178	-0.690	-175	-0.663

\*  $\Delta H_{tet}$  numbers are in kJ/mol;  $\Delta S_{tet}$  numbers are in kJ/mol·K

Table 5 shows calculated  $\Delta H_{tet}$  values when D3 is included with M06-2X and B3LYP. The addition of Grimme's D3 dispersion correction decreases the predicted  $\Delta H_{tet}$  values calculated with M06-2X by ~40 kJ/mol. This is not surprising as M06-2X has already been specifically parameterized to capture NCIs. Including D3 with B3LYP

dramatically improved results, but the functional still incorrectly orders the  $\text{Cp}^{*\text{Pr}}$  and  $\text{Cp}^{*\text{iPr}}$  variant.

Table 5. Heats of tetramerization for the  $\text{Cp}^*$ ,  $\text{Cp}^{*\text{Pr}}$  and  $\text{Cp}^{*\text{iPr}}$  variants with added dispersion.

Method	$\text{Al}_4\text{Cp}^*_4$	$\text{Al}_4\text{Cp}^{*\text{Pr}}_4$	$\text{Al}_4\text{Cp}^{*\text{iPr}}_4$
<b>EXPERIMENTAL</b>	<b>-150</b>	<b>-160</b>	<b>-158</b>
B3LYPD3/6-31G(d,p)	-167	-180	-184
M062XD3/6-31G(d)	-202	-223	-220

\*  $\Delta H_{tet}$  numbers are in kJ/mol.

The M06-2X functional is clearly superior to all other methods tested and does not require explicit treatment for van der Waals interactions. This choice is consistent with recent work done on the  $\text{Cp}^*$  and  $\text{Cp}$  variants as well as the related heterocubanes reported by Stelzer and co-workers [45], [62]. Table 6 shows the final calculated thermodynamic values for all five clusters using M06-2X/cc-pVTZ including BSSE and solvent corrections.

Table 6. Calculated  $\Delta H_{tet}$  including basis set superposition error correction for all variants.

	$\text{Al}_4\text{Cp}^*_4$	$\text{Al}_4\text{Cp}_4$	$\text{Al}_4\text{Cp}^\wedge_4$	$\text{Al}_4\text{Cp}^{*\text{Pr}}_4$	$\text{Al}_4\text{Cp}^{*\text{iPr}}_4$
M062X/cc-pVTZ	-148.4	-106.7	-153.1	-158.7	-155.8
Experimental	-150	-	-	-160	-158

\* All numbers are in kJ/mol.

### 3. NMR Results

In addition to accurate enthalpies of tetramerization, predicted  $^{27}\text{Al}$  NMR shifts using the M06-2X functional are quite accurate for known monovalent aluminum clusters. There are eight cyclopentadienyl aluminum structures discussed in this work with experimental  $^{27}\text{Al}$  NMR data: the  $\text{Cp}$  and  $\text{Cp}^\wedge$  tetramers and the monomers and

tetramers of the  $\text{Cp}^*$ ,  $\text{Cp}^{*\text{Pr}}$  and  $\text{Cp}^{*\text{iPr}}$  variants. In addition to these eight, experimental NMR data for nine additional related aluminum cyclopentadiene clusters have been reported by Sitzmann and coworkers [35]. Gauge-independent atomic orbital (GIAO) calculations with M06-2X using a 6-31G(d) basis set were performed and the results show that a static shift of +4.5 ppm brings calculated results into close agreement with experiment. Test calculations with the larger cc-pVTZ basis set using the M06-2X functional showed virtually the same results, just with a slightly larger static shift. A plot of experimental values against calculated values, and associated regression fit, are shown in Figure 13.

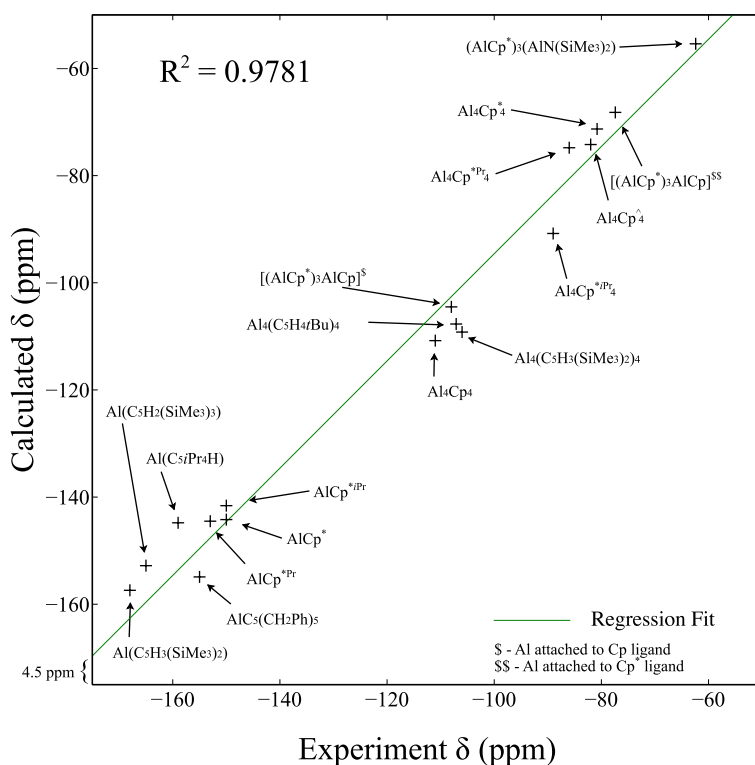


Figure 13. Calculated vs. experimental chemical shifts using M06-2X/6-31G(d).

The use of other functionals showed strong variations from experiment. Figure 14, for example, shows the poor predictive capability of a functional such as BP86 which was used in previous works. The plot shows the same 17 structures from Figure 13, but the calculated ppm values were determined with BP86/SVP. A linear regression results in

a y-intercept of -35, but also in a slope of 0.7. This slope indicates a systematic error present when using the BP86/SVP method. Specifically, at smaller ppm magnitudes, calculated results tend to be more negative than experimental results. At about -115 ppm, calculated and experimental tend to match. At magnitudes beyond -115 ppm, calculated results tend to be less negative than experimental results. Additionally, the linear fit with an  $R^2$  of 0.9286 is not as good as the one for M06-2X with an  $R^2$  of 0.9781.

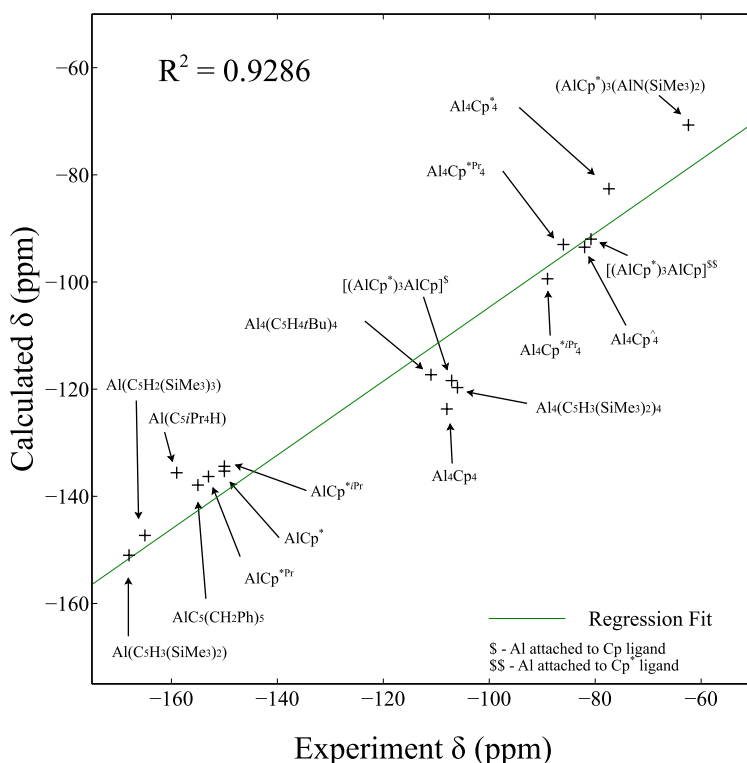


Figure 14. Calculated chemical shifts using BP86/SVP.

To illustrate this point, Table 7 shows the calculated and experimental NMR chemical shifts for all 17 structures. It is ordered from the most negative experimental value to least negative and includes the difference between experiment and calculation for each structure. For BP86/SVP, the average difference from experiment for the seven structures with chemical shifts less than -115 ppm is 17.5. The average difference from experiment for the ten structures with chemical shifts greater than -115 ppm, however, is -10.1. For M06-2X/6-31G(d), the average difference from experiment for the seven

structures with chemical shift less than -115 ppm is 8.5. For the ten structures with chemical shifts more than -115 ppm the average is 4.3. This is consistent with assertion that M06-2X/6-31G(d) provides NMR calculations that are generally about 5 ppm off from experiment.

Table 7. Difference of calculated  $^{27}\text{Al}$  NMR chemical shifts from experiment.

Structure	Calculated Results with delta				Experiment al Results
	BP86	delta	M062X	delta	
$\text{Al}(\text{C}_5\text{H}_3(\text{SiMe}_3)_2)$	-151.0	<b>17.0</b>	-157.4	<b>10.6</b>	-168
$\text{Al}(\text{C}_5\text{H}_2(\text{SiMe}_3)_3)$	-147.3	<b>17.7</b>	-152.8	<b>12.2</b>	-165
$\text{Al}(\text{C}_5\text{iPr}_4\text{H})$	-135.6	<b>23.4</b>	-144.8	<b>14.2</b>	-159
$\text{AlC}_5(\text{CH}_2\text{Ph})_5$	-137.9	<b>17.1</b>	-154.9	<b>0.1</b>	-155
$\text{Cp}^*$ monomer	-135.3	<b>14.7</b>	-144.2	<b>5.8</b>	-150
$\text{Cp}^{\text{iPr}}$ monomer	-136.3	<b>13.7</b>	-141.6	<b>8.4</b>	-150
$\text{Cp}^{\text{Pr}}$ monomer	-134.4	<b>18.6</b>	-144.5	<b>8.5</b>	-153
$\text{Cp}$ tetramer	-117.3	<b>-6.3</b>	-110.8	<b>0.2</b>	-111
$(\text{AlCp}^*)_3\text{AlCp}^{\text{s}}$	-123.7	<b>-15.7</b>	-104.5	<b>3.5</b>	-108
$\text{Al}_4(\text{C}_5\text{H}_4\text{tBu})_4$	-118.4	<b>-11.4</b>	-107.7	<b>-0.7</b>	-107
$\text{Al}_4(\text{C}_5\text{H}_3(\text{SiMe}_3)_2)_4$	-119.7	<b>-13.7</b>	-109.3	<b>-3.3</b>	-106
$\text{Cp}^{\text{iPr}}$ tetramer	-93.0	<b>-4.0</b>	-90.8	<b>-1.8</b>	-89
$\text{Cp}^{\text{Pr}}$ tetramer	-99.4	<b>-13.4</b>	-74.8	<b>11.2</b>	-86
$\text{Cp}^{\wedge}$ tetramer	-93.5	<b>-11.5</b>	-74.2	<b>7.8</b>	-82
$\text{Cp}^*$ tetramer	-92	<b>-11</b>	-71.3	<b>9.7</b>	-81
$(\text{AlCp}^*)_3\text{AlCp}^{\text{ss}}$	-82.6	<b>-5.6</b>	-68.2	<b>8.8</b>	-77
$(\text{AlCp}^*)_3(\text{AlN}(\text{SiMe}_3)_2)$	-70.3	<b>-8.3</b>	-55.4	<b>6.6</b>	-62

<sup>s</sup> Al attached to Cp ligand

<sup>ss</sup> Al attached to Cp\* ligand

#### 4. Structural Analysis of $\text{Al}_4\text{Cp}^{\text{Pr}}_4$ and $\text{Al}_4\text{Cp}^{\text{iPr}}_4$

Solutions the  $\text{Cp}^{\text{Pr}}$  and  $\text{Cp}^{\text{iPr}}$  variants failed to produce x-ray quality crystals, and thus direct structural information is not available for these two newly synthesized systems. Therefore, multiple calculations at the M06-2X/cc-pVTZ DFT level of theory were completed and resulting tetramerization energies were compared with variable temperature NMR experiments. For computational expediency, solvent corrections were not calculated.

The additional ligand steric bulk in the  $\text{Cp}^{*\text{Pr}}$  and  $\text{Cp}^{*\text{iPr}}$  variants results in a number of potential isomeric configurations of the tetramers. Unlike the  $\text{Cp}^*$  monomers, the monomers of the  $\text{Cp}^{*\text{Pr}}$  and  $\text{Cp}^{*\text{iPr}}$  variants are not symmetric. DFT is therefore used to determine the ground state structure, beginning with the  $\text{Cp}^{*\text{Pr}}$  variant. Two stable configurations of the monomeric  $\text{AlCp}^{*\text{Pr}}$  were found and are displayed in Figure 15. In the first, shown in Figure 15(a) and referred to here as type A, the propyl group is oriented away from the monovalent aluminum. The type B configuration shown in Figure 15(b) has the propyl directed inwards in a configuration that would be expected to lead to increased steric hindrance in the tetramer.

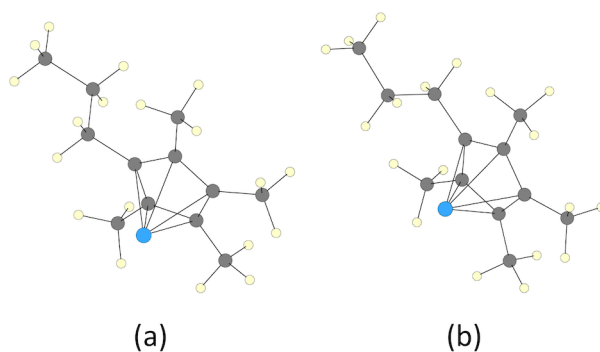


Figure 15. Type A (a) and type B (b) monomers for the  $\text{Cp}^{*\text{Pr}}$  variant.

The type A monomer is only 1.9 kJ/mol lower in DFT energy than the type B monomer. Both types of monomers were found to combine into stable tetramers, though the tetramer formed by type B monomers is less enthalpically stable than its type A counterpart. The most enthalpically stable tetramers derived from each variant are shown in Figure 16. The type B tetramer has a BSSE corrected  $\Delta H_{tet}$  of -135.3 kJ/mol as compared to the -165.4 kJ/mol for the type A tetramer without the solvent correction. This appears to be primarily due to a larger Al-Al separation in the type B tetramer, as might be expected. The average Al-Al distance in the type B variant is 2.867 Å, 10 picometers larger than the 2.767 Å distance for type A tetramers, and is consistent with weaker bonding. Also considered were tetrameric variants formed with a mix of type A and B monomers. While none of these were found to have the highest enthalpic stability,

their predicted  $\Delta H_{tet}$  values are close to the most enthalpically stable structure tested and the experimental value. The most enthalpically stable mixed configuration, a tetramer composed of one B type monomer and three A type monomers, has a  $\Delta H_{tet}$  of -161.9 kJ/mol, just over 3 kJ/mol lower than a tetramer composed of all A type monomers. It also has an average Al-Al distance of 2.794 Å which is only slightly larger than the average Al-Al distance in the pure type A tetramer.

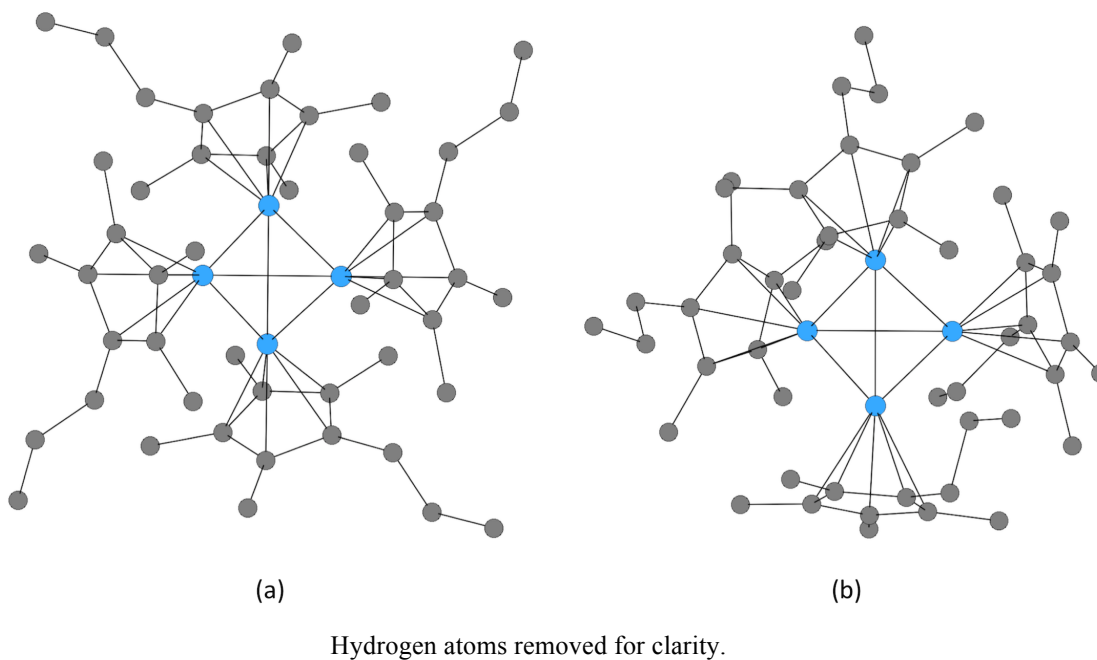
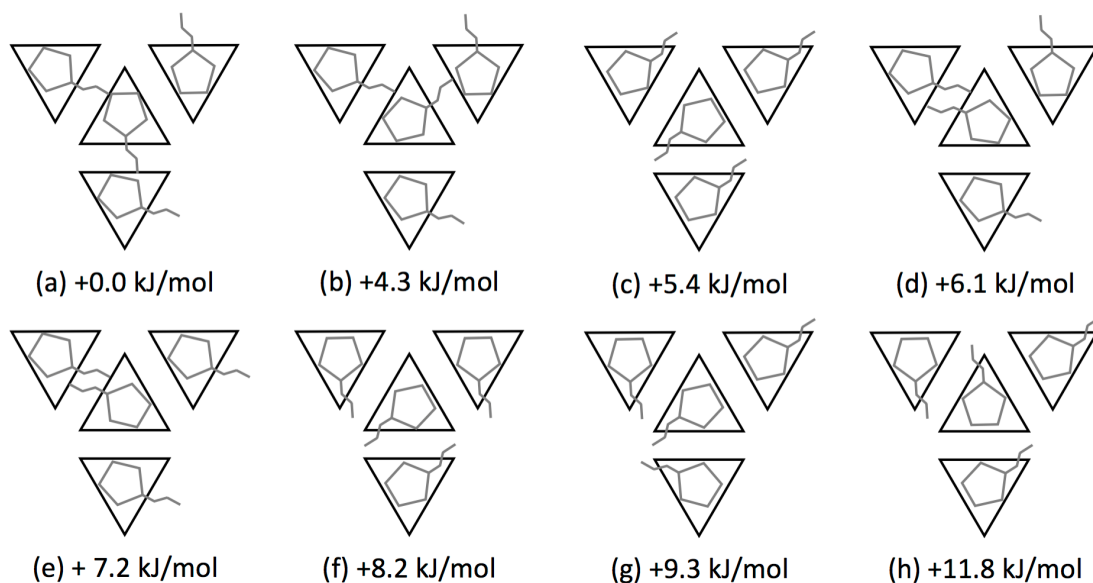


Figure 16. Type A (a) and type B (b) tetramers for the  $\text{Cp}^{*\text{Pr}}$  variant.

Beyond the difference in monomers of the  $\text{Cp}^{*\text{Pr}}$  variant, there are also many possible configurations of the  $\text{Cp}^{*\text{Pr}}$  tetramer. To understand these configurations, it is helpful to imagine the tetramer as a tetrahedron, with each face of the tetrahedron represented by a  $\text{Cp}^{*\text{Pr}}$  ligand. There are two distinct directions the propyl arm of the ligand can point. It can point towards the edge of an adjacent ligand, in which case the propyl arm settles between two adjacent methyl groups from the neighboring ligand, or it can point towards the gap between two adjacent ligands, which is essentially one of the vertexes of the tetrahedron. Each type of configuration, edge or vertex, has separate configurations within it. The configurations are visualized in Figure 17 by a flattened

tetrahedron representing the four faces of the central  $\text{Al}_4$  tetrahedron and their respective  $\text{Cp}^{*\text{Pr}}$  configurations. DFT energies are listed for each configuration relative to the global minimum.



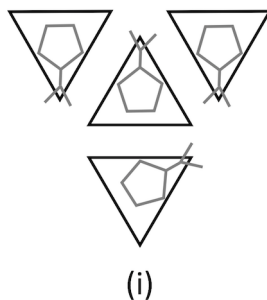
Me groups omitted for clarity.

Figure 17. Eight different isomers of the  $\text{Cp}^{*\text{Pr}}$  tetramer, ordered by DFT energies.

The  $\Delta H_{tet}$  of these configurations are all within 13 kJ/mol of each other, which is comparable to the error in DFT thermochemical results (3 kJ/mol). The  $\Delta H_{tet}$  of the most enthalpically stable configuration shown in Figure 17(a), however, is nearly 5 kJ/mol lower than the next closest isomer, Figure 17(b).

Unlike the  $\text{Cp}^{*\text{Pr}}$  monomer,  $\text{Cp}^{*\text{iPr}}$  monomers are symmetric about the plane of the ligand and do not have multiple variants. Calculations of isomers showed that  $\text{Cp}^{*\text{iPr}}$  configurations in which the  $\text{iPr}$  group points towards the vertex of the tetrahedron are strongly preferred. Because part of the isopropyl group protrudes towards the aluminum core, arranging four ligands in one of the various edge configurations forces a slight separation between the four core aluminum atoms, which results in a significant increase in the calculated  $\Delta H_{tet}$  that is inconsistent with experiment. A variant similar to Figure

17(a), the most enthalpically stable configuration for  $\text{Cp}^{*\text{Pr}}$ , resulted in a predicted  $\Delta H_{tet}$  of -135.6 kJ/mol, significantly different than the experimental value of -158 kJ/mol. The Al-Al bond distance for this configuration was found to be 2.863 Å, almost 0.1 Å further apart than the Al-Al bond distance of the  $\text{Cp}^{*\text{Pr}}$  variant in this configuration. The  $\Delta H_{tet}$  for vertex configurations were much closer to experimental results. In addition to analyzing configurations (c), (f), (g) and (h) from Figure 17 for the  $\text{Cp}^{*\text{Pr}}$  variant, one additional vertex configuration was analyzed. This configuration is very similar to (f) except that instead of two sets of two isopropyl arms pointing to the same vertex there is only one set of two isopropyl arms pointing towards the same vertex. The other two isopropyl arms point to separate vertices. This configuration, (i), is shown in Figure 18. The calculated values of  $\Delta H_{tet}$  for the five configurations were all within 8 kJ/mol of each other, with configuration (i) the most enthalpically stable. Of note, the Al-Al bond distances for this configuration was 2.824 Å. While this distance is still greater than the Al-Al bond distance of the  $\text{Cp}^{*\text{Pr}}$  variant, it is about 40 percent closer than the isopropyl edge configuration analyzed.

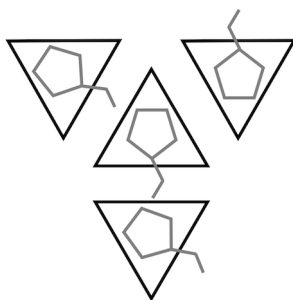


Me groups omitted for clarity.

Figure 18. The lowest energy configuration for the  $\text{Cp}^{*\text{Pr}}$  variant.

## B. ANALYSIS OF THE Cp<sup>\*Et</sup> VARIANT AND OVERALL LIGAND TRENDS

Using this same approach, another cluster in this monovalent aluminum series, Al<sub>4</sub>Cp<sup>\*Et</sup><sub>4</sub> (Cp<sup>\*Et</sup>=C<sub>5</sub>Me<sub>4</sub>Et), was examined. While this system has yet to be synthesized, it allows for the analysis of trends in the tetramer properties as a function of Cp bulk. The most enthalpically stable configuration for this variant is shown in Figure 19. This is the same configuration as the lowest energy Cp<sup>\*Pr</sup> variant shown in Figure 17(a). The  $\Delta H_{tet}$  for this cluster is -157.9 kJ/mol, which makes it slightly more strongly bound than the Cp<sup>\*</sup> variant, but less strongly bound than the Cp<sup>^</sup> variant.

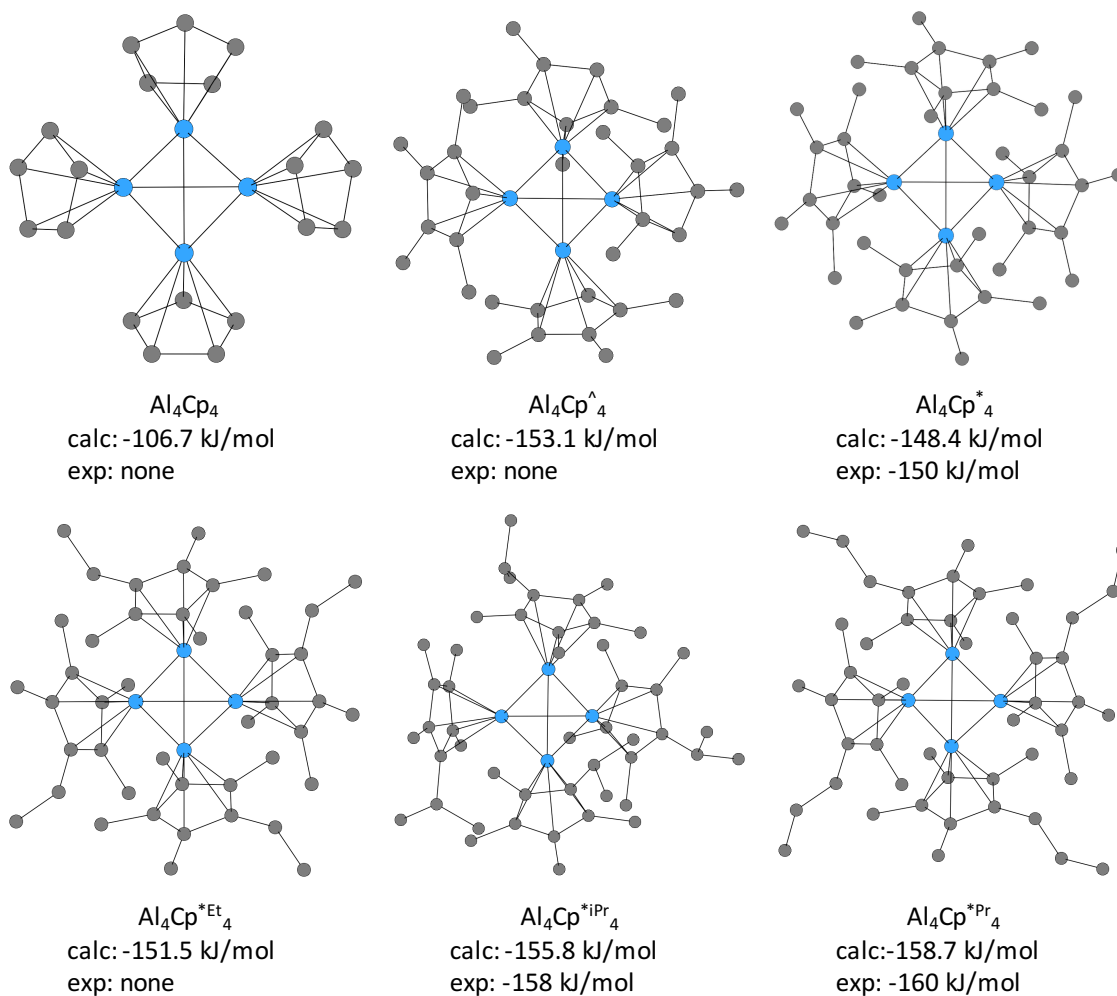


Me groups omitted for clarity.

Figure 19. The lowest energy configuration for the theoretical Cp<sup>\*Et</sup> variant.

After structural analysis of the Cp<sup>\*Pr</sup>, Cp<sup>\*iPr</sup> and Cp<sup>\*Et</sup> variants was complete, all six clusters discussed up to this point were optimized with M06-2X/cc-pVTZ. BSSE corrections were added as well as corrections based on the presence of the solvent toluene. Solvent corrections increased  $\Delta H_{tet}$  values by about 6 kJ/mol for all clusters, but brought calculated values very close to experimental results. Figure 20 shows the most enthalpically stable structures for all six Cp variants, listed in order of increasing steric bulk and annotated with calculated  $\Delta H_{tet}$  values. Experimental values are also included for the Cp<sup>\*</sup>, Cp<sup>\*Pr</sup> and Cp<sup>\*iPr</sup> variants. In general, adding steric bulk within this series results in tetramers with stronger binding, but Al<sub>4</sub>Cp<sup>^</sup><sub>4</sub> is an exception to this trend. Crystal structure data for the Cp<sup>^</sup> variant show that it is configured as shown in Figure 17(b), though it should be noted that DFT calculations show that the Cp<sup>^</sup> variant configured as in Figure 17(a) has a  $\Delta H_{tet}$  only 0.5 kJ/mol higher than the crystal

structure. This suggests that the  $\text{Cp}^\wedge$  variant may be somewhat insensitive to configuration. Despite the fact that the  $\text{Cp}^*$  and  $\text{Cp}^{*\text{Et}}$  variants carry more steric bulk, the  $\text{Cp}^\wedge$  variant is more enthalpically stable. Stability gained by inter-ligand interactions can be offset by a loss of Al-Al bond strength due to increased monomer separation within a cluster. To better understand this balance, the electronic structure is considered in more detail.



Calculated and experimental  $\Delta H_{tet}$  are included. Hydrogens removed for clarity.

Figure 20. Initial six variants investigated in order of increasing steric bulk.

### C. QUANTUM THEORY OF ATOMS IN MOLECULES ANALYSIS

While Al-Al bond length within the core of these clusters can inform overall bond strength, this length does not appear to be good metric for gauging overall cluster stability. The lowest energy configuration of the  $\text{Cp}^{*\text{Pr}}$  variant, for example, has larger Al-Al separation than the  $\text{Cp}$ ,  $\text{Cp}^\wedge$  and  $\text{Cp}^*$  variants but is enthalpically preferred. Work done by Stelzer and co-workers demonstrated the existence of attractive NCIs between adjacent ligands in the  $\text{Cp}^*$  variant [45]. Additionally, Lu and co-workers demonstrated the existence of attractive NCIs across ligands in the  $\text{Cp}^*$  variant [62]. To understand the role of inter-ligand bonding in all variants, QTAIM analysis is performed.

QTAIM analysis involves examining key topological parameters of the electronic density of a given molecule. In particular, points where the density gradient vanishes can indicate potential bonds between atoms. Figure 21 shows a plot of the norm of the gradient for the  $\text{Cp}^-$  anion. All values are positive and are color coded such that red is a maximum and blue is zero. Within the  $\text{Cp}^-$  molecule there are 11 critical points where  $\nabla\rho$  vanishes. Ten of these critical points clearly correspond with the ten covalent bonds present in the molecule. These critical points are three-dimensional saddle points with values of  $\rho$  decreasing in two orthogonal directions and increasing in the third. These critical points are called bond critical points (BCPs) because they correspond to maximum pathways of electron density between two atoms. The 11<sup>th</sup> critical point, at the center of the molecule, is a three-dimensional saddle point with values of  $\rho$  increasing in two orthogonal directions and decreasing in the third. This critical point is called a ring critical point and is purely consequence of the ring structure of the molecule. Using these and other metrics of  $\rho$ , QTAIM provides a means of locating bonds and a quantitative way to classify them. Of particular importance is the ability of QTAIM to predict NCIs that are difficult if not impossible to predict from molecular structure. These types of interactions are key contributors to the overall stability of the clusters studied in this work.

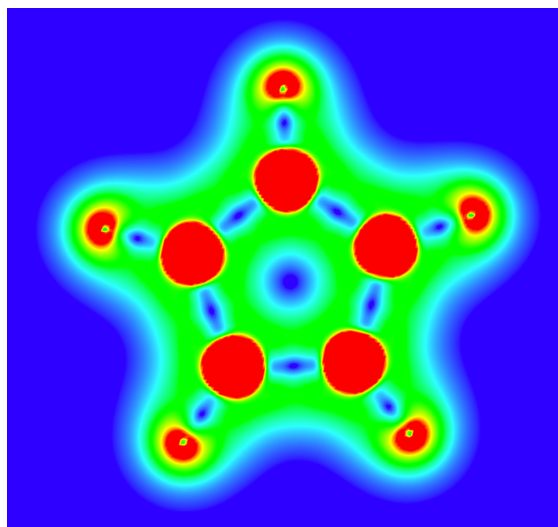


Figure 21. Plot of the norm of  $\nabla\rho$  for the  $\text{Cp}^-$  anion.

BCPs indicating NCIs are found across ligands in the  $\text{Cp}^*$  variant and values for electron density at these and other key BCPs ( $\rho_b$ ) are within one percent of previous work [62]. Similar BCPs are found across ligands of the two newly synthesized  $\text{Cp}^{*\text{Pr}}$  and  $\text{Cp}^{*\text{iPr}}$  tetramers. Figures 22 and 23 show BCPs between adjacent ligands for the lowest energy tetramers for both variants. BCPs between hydrogen atoms as well as hydrogen and carbon atoms across ligands are observed. No inter-ligand bonding was found for the  $\text{Cp}$  variant. BCPs between hydrogen atoms within a single ligand are also observed, but these do not contribute to overall tetramer stability.

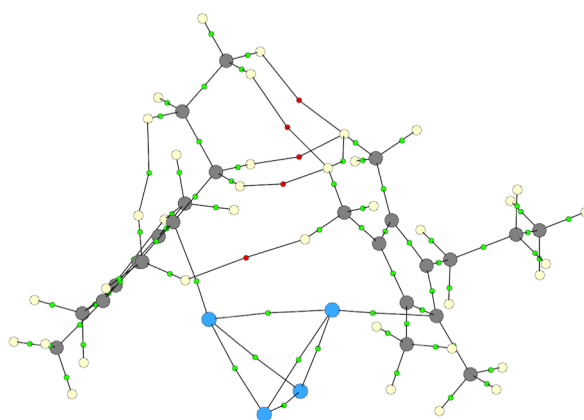


Figure 22. Inter-ligand H-H BCPs in the  $\text{Cp}^{*\text{Pr}}$  variant (shown in red).

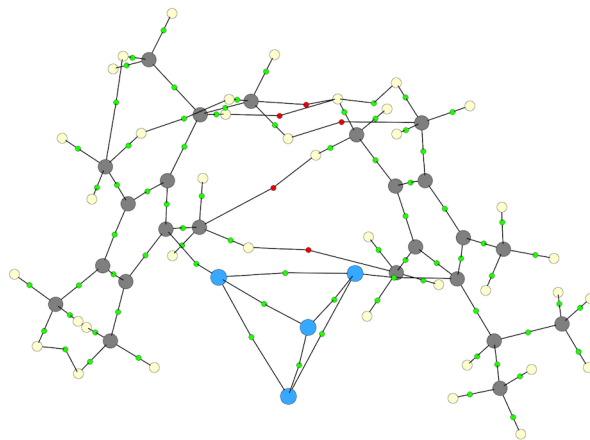


Figure 23. Inter-ligand H-C and H-H BCPs in the Cp<sup>\*ipr</sup> variant (shown in red).

All inter-ligand BCPs were characterized by low values of  $\rho_b$ , positive values of  $\nabla^2\rho_b$  and a positive value for total energy density at the BCP,  $H_b$ . These are all indicators of closed shell bonding, or more generally, NCIs [81], [82]. The QTAIM parameters for Al-Al BCPs indicate a shared or covalent type bond. This is due to  $\nabla^2\rho_b < 0$  and,  $H_b < 0$ , both indicators of a covalent bond [83], [84]. The fact that  $\rho_b$  at these points is slightly lower than the more typical  $10^{-1} e\cdot\text{\AA}^{-3}$  only indicates that the shared bond is relatively weak [85]. BCPs indicating Al-C bonds have low values of  $\rho_b$ , small negative values for  $H_b$ , a kinetic energy per density ratio ( $G_b/\rho_b$ ) close to one and positive values for  $\nabla^2\rho_b$ . These are all indicators of bonding with metal [86], [87]. Additionally, for all but the Cp variant, less than five BCP connecting each aluminum atom to its associated ligand were found. This is a key characterization of the hapticity of the monomer. Hapticity is a measure of the position of the aluminum atom when looking down at the plane of the ligand. A hapticity of  $\eta^5$  would indicate shared bonding with all five carbon atoms, resulting in a position of the aluminum atom in the center of the carbon ring. At the other extreme, a hapticity of  $\eta^1$  would indicate bonding to only one of the carbon atoms and the aluminum atom would be positioned very nearly right on top of that atom. The fact that QTAIM analysis shows less than five BCPs between aluminum atoms and respective carbon rings would seem to suggest that these monomers are not  $\eta^5$ . As pointed out by Farrugia and co-workers, however, BCPs are unreliable indicators of formal hapticity for

metals bonded to  $\pi$ -carbocyclic ligands [88]. A relatively high ellipticity,  $\varepsilon$ , around these BCPs indicates they are in an area of a relatively flat density, making it difficult to pinpoint actual CPs. This fact, as well as the calculated geometrical structures, indicates that the formal hapticity for ligands of all variants is indeed  $\eta^5$ , as would be expected from the structure [89]. Average metrics for pertinent BCPs for all variants are listed in Table 8.

Table 8. Topological average BCP metrics for all variants.

Cluster	BCP type	$\rho$	$\nabla^2\rho$	$\varepsilon$	$ V /G$	$G/\rho$	$H$
Al <sub>4</sub> Cp <sub>4</sub>	Al-Al	0.0378	-0.0201	0.4400	2.7954	0.1677	-0.0114
	Al-C	0.0348	0.0874	5.1460	1.2596	0.8497	-0.0077
Al <sub>4</sub> Cp <sup>^</sup> <sub>4</sub>	Al-Al	0.0375	-0.0183	0.5900	2.6580	0.1854	-0.0115
	Al-C	0.0393	0.1193	12.1500	1.2228	0.9708	-0.0085
	H-H	0.0041	0.0131	0.6739	0.7330	0.6240	0.0007
	H-C <sup>s</sup>	0.0043	0.0146	2.1750	0.7050	0.6317	0.0008
Al <sub>4</sub> Cp <sup>*</sup> <sub>4</sub>	Al-Al	0.0352	-0.0154	0.5033	2.6057	0.1804	-0.0102
	Al-C	0.0403	0.1205	10.0750	1.2282	0.9678	-0.0089
	H-H	0.0055	0.0184	1.8728	0.7534	0.6564	0.0009
	H-C <sup>s</sup>	0.0062	0.0214	1.3333	0.7523	0.6640	0.0010
Al <sub>4</sub> Cp <sup>*Et</sup> <sub>4</sub>	Al-Al	0.0353	-0.0153	0.4933	2.5953	0.1822	-0.0103
	Al-C	0.0411	0.1242	4.6325	1.2265	0.9780	-0.0091
	H-H	0.0062	0.0213	1.8215	0.7609	0.6914	0.0010
	H-C <sup>s</sup>	0.0	0.0	0.0	0.0	0.0	0.0
Al <sub>4</sub> Cp <sup>*iPr</sup> <sub>4</sub>	Al-Al	0.0329	-0.0122	0.4083	2.5212	0.1781	-0.0089
	Al-C	0.03895	0.10833	15.798	1.24925	0.9219	-0.0090
	H-H	0.0063	0.0207	0.8416	0.7729	0.6737	0.0010
	H-C <sup>s</sup>	0.0074	0.0265	1.4044	0.7756	0.7290	0.0012
Al <sub>4</sub> Cp <sup>*Pr</sup> <sub>4</sub>	Al-Al	0.0352	-0.0153	0.4933	2.5955	0.1815	-0.0102
	Al-C	0.0410	0.1237	4.5800	1.2275	0.9756	-0.0091
	H-H	0.0062	0.0211	1.7895	0.7623	0.6913	0.0010
	H-C <sup>s</sup>	0.0040	0.0140	1.3475	0.7070	0.6868	0.0008

\* All numbers are in atomic units.

<sup>s</sup> Inter-ligand BCPs only.

The information gained through QTAIM analysis of these clusters gives insight into the bonding within the tetramers. There is not a simple trend as the steric bulk of the Cp-type ligand increases. It is reasonable to expect that the addition of steric bulk to the ligands of these types of clusters would reduce tetrameric stability, but the opposite is the case. The simplest metric for determining relative Al-Al bond strength is the average bond distance of the six bonds that join the core aluminum atoms together. The Cp and Cp<sup>^</sup> variants have the smallest average Al-Al bond distance at 2.722 Å and 2.720 Å respectively, a mere 0.19 picometers apart and about 4.5 picometers from the next closest variant. This would seem to indicate that the Al-Al bonds within the core of the Cp and Cp<sup>^</sup> are the strongest among all cluster variants, a notion in agreement with experimental observation of only tetrameric species in solution for these two compounds. The amount of electron density at a BCP joining two atoms can indicate relative bond strength for similar type bonds [85]. Based on AIM analysis, all the Al-Al bonds for all cluster variants are shared or covalent type bonds with very similar metrics. As expected, the total electron density at the six Al-Al BCPs is highest for the Cp and Cp<sup>^</sup> variants. Table 9 shows a list of average Al-Al bond distance and total electron density at the BCPs associated with these bonds for all six cluster variants as well as two additional configurations: the Cp<sup>\*Pr</sup> variant in the configuration shown in Figure 17(b) and the Cp<sup>\*iPr</sup> variant shown in the configuration of Figure 17(a). These configurations were included because of their varied Al-Al bond distance.

Table 9. Al-Al bond distances and total electron density at BCPs for eight cluster variants.

	Cp	Cp <sup>^</sup>	Cp <sup>*</sup>	Cp <sup>*Et</sup>	Cp <sup>*iPr</sup>	Cp <sup>*Pr</sup>	Cp <sup>*Pr</sup> §	Cp <sup>*iPr</sup> §§
Al-Al dist.	2.7215	2.7196	2.7684	2.7672	2.8240	2.7670	2.7832	2.8631
$\rho_b$	0.2269	0.2249	0.2114	0.2116	0.1974	0.2114	0.2074	0.1876

\* Numbers are in Å or Å<sup>-3</sup>.

§ Orientation show in Figure 17(b).

§§ Orientation show in Figure 17(a).

There is a clear correlation between the amount of electron density at the six BCPs joining the core aluminum atoms and the Al-Al average bond distance. Figure 24 shows a linear fit of a plot of Al-Al bond distance against total electron density has an  $R^2$  value of over 0.99. This supports the conclusion that the Al-Al bonds at the core of the Cp and Cp<sup>^</sup> variants are the strongest. These bonds, however, are not the only ones involved in overall cluster stability. The H-H and H-C bonds found in all substituted Cp derivatives clearly indicate there is additional stability via non-covalent ligand interactions, both *in silico* and in solution.

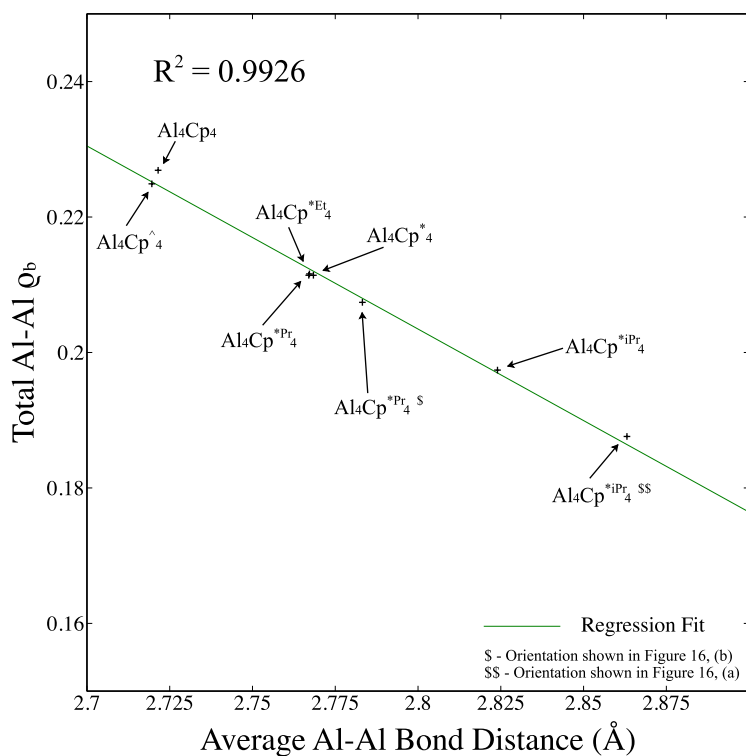


Figure 24. Al-Al bond distance vs. total  $\nabla\rho_b$  associated with Al-Al BCPs.

The relevant metric for assessing the contributions to stability from the inter-ligand H-H and H-C inter-ligand bonds is the magnitude of electron density at the associated BCPs. Like  $\rho_b$  associated with Al-Al bonds,  $\rho_b$  associated with these closed shell bonds can also indicate bond strength [90], [91]. It is important to realize, however, that similar amounts of electron density at BCPs associated with different types of bonds

most likely does not indicate that the bonds are of the same strength [86]. The inter-ligand H-H and H-C bonds in these clusters are closed shell bonds as opposed to the shared Al-Al bonds in the core. The  $\rho_b$  associated with these different types of bonds will have different impacts on stability. Additionally, we would not expect the  $\rho_b$  associated with H-H and H-C bonds to affect stability in the same way. It follows that there are three types of bonds that contribute to stability in these types of clusters: Al-Al, inter-ligand H-H, and inter-ligand H-C bonds. The total amount of electron density associated with each type of bond for each cluster variant is listed in Table 10. These metrics are listed along with the corresponding BSSE corrected  $\Delta H_{tet}$ . No solvent corrections are used so fundamental trends can be analyzed. Also included are the same two additional configurations examined in the Al-Al bond distance analysis. The value of  $\Delta H_{tet}$  for these configurations provides more overall variance for subsequent regression analysis.

Table 10. Total electron density at Al-Al, H-H and H-C BCPs for various clusters.

	Total Al-Al $\rho_b$	Total H-H $\rho_b$	Total H-C $\rho_b$	$\Delta H_{tet}$ (calc)
Al <sub>4</sub> Cp <sub>4</sub>	0.2269	0.0	0.0	-108.6
Al <sub>4</sub> Cp <sup>^</sup> <sub>4</sub>	0.2249	0.0738	0.0086	-161.1
Al <sub>4</sub> Cp <sup>*</sup> <sub>4</sub>	0.2114	0.1066	0.0106	-154.5
Al <sub>4</sub> Cp <sup>*Et</sup> <sub>4</sub>	0.2116	0.1249	0	-157.9
Al <sub>4</sub> Cp <sup>*iPr</sup> <sub>4</sub>	0.1974	0.1193	0.0669	-162.7
Al <sub>4</sub> Cp <sup>*Pr</sup> <sub>4</sub>	0.2114	0.1242	0.0159	-165.7
(Al <sub>4</sub> Cp <sup>*Pr</sup> <sub>4</sub> ) <sup>§</sup>	0.2074	0.1199	0.0144	-160.0
(Al <sub>4</sub> Cp <sup>*iPr</sup> <sub>4</sub> ) <sup>§§</sup>	0.1876	0.1255	0.0382	-135.6

\* Numbers are in  $e\cdot\text{\AA}^{-3}$  or kJ/mol

§ Orientation shown in Figure 17(b).

§§ Orientation shown in Figure 17(a).

Previous work by Boyd and co-workers demonstrated a linear relationship between  $\rho_b$  and bond energy for various types of bonds [92]. A multivariable linear regression of the data in Table 10 was performed. It was based on the summed electron density at Al-Al, H-H, and H-C BCPs to gain a sense of their relative contributions to tetramer stability. The result is this equation:

$$\Delta H_{tet} = a_0 + a_1\rho_{Al-Al} + a_2\rho_{H-H} + a_3\rho_{H-C}, \quad (8)$$

where  $\rho_{X-X}$  is the total electron density at the BCPs associated with X-X bonds for a given cluster. Figure 25 shows a plot of  $\Delta H_{tet}$  calculated with this equation against  $\Delta H_{tet}$  calculated through DFT vibrational frequency analysis. The electron density associated with H-C inter-ligand bonds, governed by the coefficient  $a_3$ , contributes the least to tetramer stability. The optimal fit gives ratios  $a_1/a_3 \approx 3.8$  and  $a_2/a_3 \approx 1.3$ . Thus, approximately 65% of the variation in tetramer binding energy can be explained by the electron density at Al-Al BCPs, which varies linearly with Al-Al separation. The remainder can be attributed to inter-ligand effects.

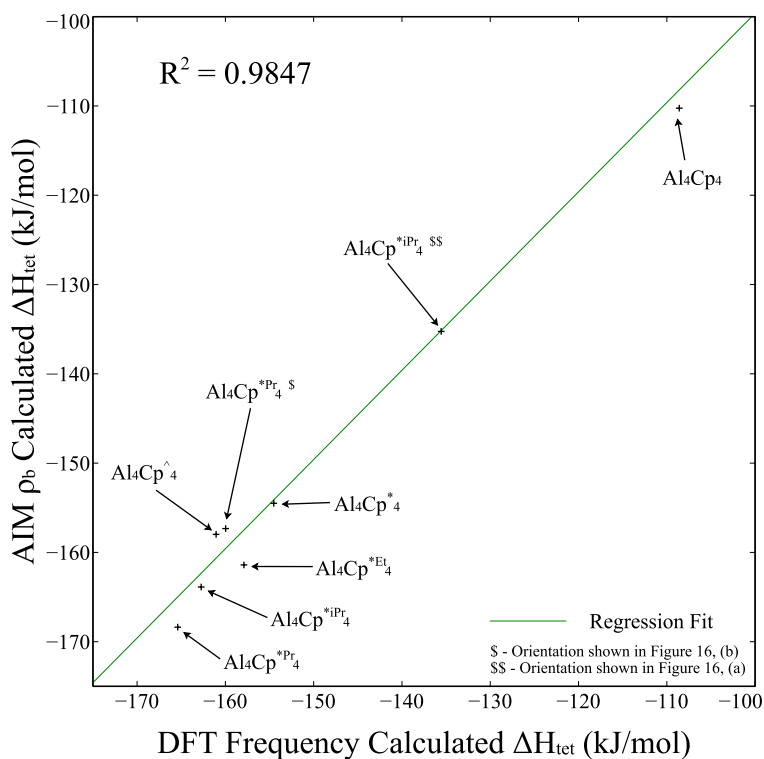


Figure 25.  $\Delta H_{tet}$  calculated via DFT frequency analysis compared to  $\Delta H_{tet}$  calculated via equation (8).

This analysis helps explain why the Cp variant has the lowest binding energy of all clusters considered here, despite having the second smallest Al-Al bond distance and the largest  $\rho_b$  associated with Al-Al bonds. The Cp variant has no inter-ligand H-H or H-C bonds and therefore no additional contribution to tetramer stability. Compared to the Cp variant, the Cp<sup>^</sup> variant has only a slightly smaller average Al-Al bond distance and slightly less  $\rho_b$  associated with Al-Al bonds, but because of the additional  $\rho_b$  associated with inter-ligand H-H and H-C bonds, the Cp<sup>^</sup> variant is 52.5 kJ/mol more stable. This is also why the Cp<sup>\*Pr</sup> variant is slightly more stable than the Cp<sup>\*</sup> despite having the same amount of  $\rho_b$  associated with Al-Al bonds. The Cp<sup>\*Pr</sup> has roughly 20% more electron density associated with inter-ligand H-H and H-C bonds. It is clear that inter-ligand H-H and H-C bonds make non-trivial contributions to the stability. More steric bulk does not necessarily mean more stability, however. Even though the Cp<sup>\*</sup> variant has more steric bulk than the Cp<sup>^</sup> variant, the Cp<sup>^</sup> variant is slightly more stable. Despite the addition of four methyl groups to each ligand in a Cp variant, the average Al-Al distance in the resulting Cp<sup>^</sup> variant is virtually identical (within 0.2 picometers) to that of the Cp variant. The addition of a fifth methyl group, however, results in an average Al-Al distance in a Cp<sup>\*</sup> variant that is 5.5 picometers longer than that of a Cp variant. While the Cp<sup>\*</sup> variant has more  $\rho_b$  associated with inter-ligand bonds than the Cp<sup>^</sup> variant, because of its extra steric bulk, the Cp<sup>^</sup> variant has more  $\rho_b$  associated with Al-Al bonds due to its smaller average Al-Al distance. The extra  $\rho_b$  associated with inter-ligand bonds in the Cp<sup>\*</sup> variant is not sufficient to compensate for the loss of  $\rho_b$  associated with Al-Al bonds. Ultimately there is no simple correlation between ligand bulk and enthalpic stability.

#### D. EQUILIBRIUM CONSTANT CALCULATIONS

To further investigate the behavior of this series of aluminum tetramer clusters, their monomer/tetramer equilibrium in solution was examined. Availability of free monomers in solution is likely a key element in the formation of larger metalloid clusters such as Al<sub>50</sub>Cp<sup>\*</sup><sub>12</sub>. As tetrameric forms disproportionate into trivalent species (e.g., AlCp<sup>\*</sup><sub>3</sub>) and bulk aluminum, the presence of free monomers in solution could allow for their binding to small particles of bulk aluminum to form metalloid clusters. To understand the behavior of the clusters in this work, analysis similar to that of Huber and

Schnöckel following synthesis of the  $Cp^{\wedge}$  variant was performed [38]. The thermodynamic results for all six variants were used to calculate the equilibrium constant,  $K$ , at room temperature using the van 't Hoff equation.

$$K_{eq} = e^{-\frac{\Delta H - T\Delta S}{RT}}. \quad (9)$$

Despite excellent agreement with tetramerization enthalpies,  $K$  values calculated via DFT differ dramatically from experiment due to the exponential dependence on  $\Delta S$ . As discussed previously, no computational method examined was found to predict entropy changes with sufficient accuracy to match experimental  $K$  values. Schnöckel and Huber linearly scaled calculated  $\Delta H_{tet}$  and  $\Delta S_{tet}$  values such that the results for the  $Cp^*$  variant would match experimental values. Because of the poor performance by DFT to predict  $\Delta S_{tet}$ , however, rather than scaling the values for  $\Delta H_{tet}$  and  $\Delta S_{tet}$  separately, the DFT results for both  $\Delta H_{tet}$  and  $\Delta S_{tet}$  are used to calculate  $K$  for each cluster before any scaling. The resulting  $K$  values are then normalized so that the result for the  $Cp^*$  variant corresponds to a monomer to tetramer ratio of 1:449, the experimental ratio. Ratios for the other clusters can then be calculated from their respective normalized  $K$  values. The larger the  $K$  value, the larger the ratio of tetramers to monomers and hence the fewer free monomers in solution. The results of this analysis, as well as experimental values, are shown in Table 11. It should be stressed that this method will likely not indicate which clusters are likely to have monomers found in solution, but instead gives a comparison of which clusters are more or less likely to have monomers in solution as compared to the  $Cp^*$  variant. Rather than attempting to produce predictive values for  $K$ , this method is comparative.

Table 11. Experimental and calculated equilibrium constants at 298.15K.

	Al <sub>4</sub> Cp <sup>*</sup> <sub>4</sub>	Al <sub>4</sub> Cp <sub>4</sub>	Al <sub>4</sub> Cp <sup>^</sup> <sub>4</sub>	Al <sub>4</sub> Cp <sup>*Et</sup> <sub>4</sub>	Al <sub>4</sub> Cp <sup>*Pr</sup> <sub>4</sub>	Al <sub>4</sub> Cp <sup>*iPr</sup> <sub>4</sub>
Experimental Values						
$\Delta H_{tet}$	-150	-	-	-	-160	-158
$\Delta S_{tet}$	-0.300	-	-	-	-0.398	-0.477
$K$	$4.1 \times 10^{10}$	-	-	-	$1.8 \times 10^7$	$5.8 \times 10^2$
Ratio (mon/tet)	1:449	-	-	-	1:65	1:5
Calculated Values						
$\Delta H_{tet}$	-148.4	-106.7	-153.1	-151.5	-158.7	-155.8
$\Delta S_{tet}$	-0.639	-0.380	-0.437	-0.639	-0.664	-0.663
$K$	$4.2 \times 10^{-8}$	$7.0 \times 10^{-2}$	$9.9 \times 10^3$	$1.5 \times 10^{-7}$	$1.3 \times 10^{-7}$	$4.6 \times 10^{-8}$
Normalized $K$ Values						
$K$	$4.1 \times 10^{10}$	$6.8 \times 10^{16}$	$9.6 \times 10^{21}$	$1.4 \times 10^{11}$	$1.3 \times 10^{11}$	$4.5 \times 10^{10}$
Ratio (mon/tet)	1:449	1:16,132	1:313,091	1:613	1:598	1:460

\*  $\Delta H_{tet}$  numbers are in kJ/mol;  $\Delta S_{tet}$  numbers are in kJ/mol·K

The results show that the  $K$  values for Cp<sup>\*</sup>, Cp<sup>\*iPr</sup>, Cp<sup>\*Pr</sup> and Cp<sup>\*Et</sup> variants are all within an order of magnitude and should have similar monomer/tetramer ratios. The results also show that  $K$  values of the Cp and Cp<sup>^</sup> variants are respectively 6 and 11 orders of magnitude larger than that of the Cp<sup>\*</sup> variant. This suggests that there are likely to have significantly lower concentrations of Cp and Cp<sup>^</sup> monomers as compared to the Cp<sup>\*</sup> variant. It is likely that only differences of more than an order of magnitude are significant. It is unreasonable to differentiate the concentrations of the Cp<sup>\*</sup>, Cp<sup>\*iPr</sup>, Cp<sup>\*Pr</sup> and Cp<sup>\*Et</sup> variants since calculated  $K$  values for these variants are all relatively close. Since monomers of the Cp<sup>\*</sup> are known to exist in solution, then based on this analysis, it is reasonable to expect to find monomers of the Cp<sup>\*iPr</sup>, Cp<sup>\*Pr</sup> and Cp<sup>\*Et</sup> variants as well. While the Cp<sup>\*Et</sup> variant has not yet been synthesized, monomers of both the Cp<sup>\*iPr</sup> and Cp<sup>\*Pr</sup> variants were, in fact, found in solution. This analysis also indicates that monomers of Cp variant should be somewhat less prevalent in solution as compared to the Cp<sup>\*</sup> variant. Monomers of the Cp variant were never found in solution, though it is important to note that disproportionation of the Cp variant into trivalent species and bulk aluminum occurs significantly earlier than the other variants, at 85°C below room temperature [38]. Finally, the analysis suggests that monomers of the Cp<sup>^</sup> variant are of significantly lower

concentration than those of the Cp<sup>\*</sup> variant. This is consistent with the experimental fact that monomers of the Cp<sup>^</sup> variant were never found in solution [38].

The behavior of these systems with regard to monomer/tetramer equilibrium may be of importance for alternate synthesis methods such as those reported by Roesky [33] and Fisher [63], which can produce AIR monomers without the need for a complex co-condensation apparatus. A bias towards monomers in solution at higher temperatures may allow for greater synthetic availability of monomers in these solution-based synthesis methods. However, it appears that the complex balance between monovalent Al-Al bonding in the core and non-covalent ligand interactions in the exterior do not lead to a general trend with steric bulk, but rather requires analysis of each individual system.

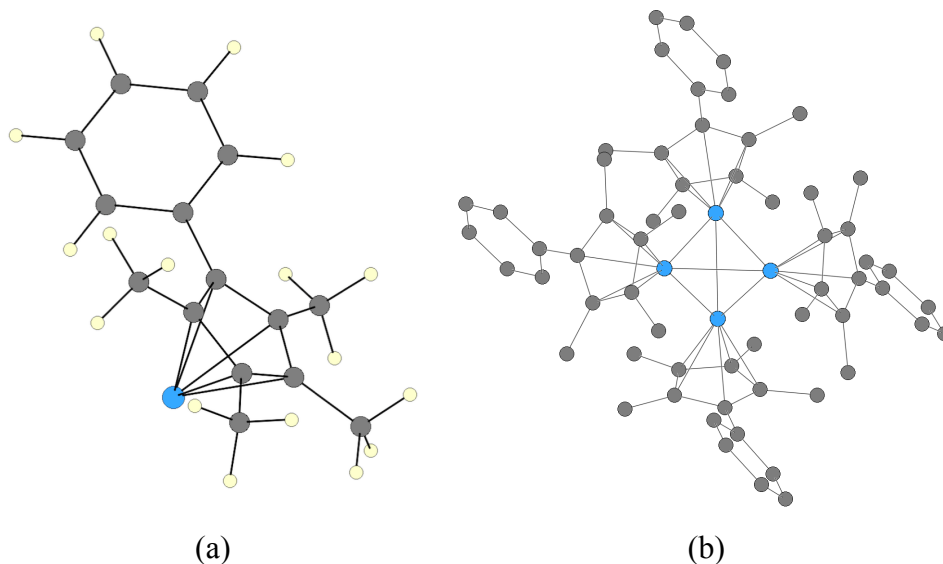
### III. LARGER LIGAND VARIANTS

#### A. EFFECTS OF ADDITIONAL STERIC BULK

While the addition of steric bulk to the unsubstituted Cp variant does not have a direct correlation with enthalpic stability, it does appear that the addition of steric bulk leads to smaller equilibrium constants, and therefore larger monomer/tetramer ratios in solution. The two clusters investigated up to this point that have the highest  $K$  also have the least amount of steric bulk. The Cp<sup>^</sup> variant, however, has only slightly less steric bulk than the Cp<sup>\*</sup> variant, yet has a significantly higher  $K$ . To further understand the relationship between steric bulk and monomers in solution an examination of four additional Cp-type variants is conducted.

##### 1. Al<sub>4</sub>(C<sub>5</sub>Me<sub>4</sub>Ph)<sub>4</sub>

In 2005 Buchin et al. reported possible synthesis of the cluster Al<sub>4</sub>Cp<sup>\*Ph</sup><sub>4</sub> (Cp<sup>\*Ph</sup> = C<sub>5</sub>Me<sub>4</sub>Ph), but the cluster failed to crystalize and experimental <sup>27</sup>Al NMR results were inconclusive [25]. Buchin et al. reported a <sup>27</sup>Al NMR chemical shift of 102.5 ppm, which is significantly higher than that of the Cp<sup>\*</sup> and Cp<sup>^</sup> tetramers, and no DFT calculations were reported [25]. Of significance was the fact that only one NMR signal was detected. Variable temperature NMR by David Morris at NAWC China Lake also confirmed the presence of only one signal up to a temperature of 100 degrees C. The Cp<sup>\*Ph</sup> variant, shown in Figure 26, has the most steric bulk of any Cp<sup>\*</sup> derivative investigated so far. Assuming the single NMR signal is the tetramer, then the absence of monomers in solution is somewhat surprising. To examine this cluster, first the structure of the variant must be determined. DFT NMR analysis is then conducted and compared with experimental results from 2005 as well as more recent results from NAWC China Lake. DFT vibrational frequency analysis is then conducted to determine thermodynamic characteristics which are not available experimentally. Finally, calculated thermodynamic values can be used to determine the value of the equilibrium constant for this cluster and compared with previous six clusters studied.



Hydrogens of tetramer removed for clarity.

Figure 26. Monomer (a) and tetramer (b) of  $\text{Cp}^{*\text{Ph}}_4$  variant.

**a. Structure of  $\text{Al}_4\text{Cp}^{*\text{Ph}}_4$**

Following synthesis of the  $\text{Cp}^{*\text{Ph}}$  tetramer, all attempts to crystalize a structure failed [25]. No experimental structural data is available. The ortho C-H of the phenyl ring protrudes in towards the aluminum atom in the energy-minimized structure. This is in a way similar to the  $\text{Cp}^{*\text{iPr}}$  variant, so a tetramer configured as in Figure 18 was considered to be a likely global minimum. Because of the possibility of twisting of the phenyl ring, however, it is not obvious that this configuration would be the lowest energy structure. In order to examine a large number of possible structures, a genetic algorithm (GA) was implemented using a more efficient DFT code, GPAW. GPAW is a DFT python code based on the projector augmented wave (PAW) method [93], [94]. The code operates within the Atomic Simulation Environment (ASE) which provides a means for creating and manipulating atomic structures [95]. The PAW, as implemented within GPAW, takes advantage of the frozen core approximation [96]. This approximation leverages the known behavior of electrons that are not part of the valence. Core electrons are treated differently and with much less computational effort than the valence electrons. The resulting core wavefunctions are smoothly combined with the valence pseudo

wavefunctions to arrive at an approximation of the all electron Kohn-Sham wavefunction [93]. This provides significant computational efficiency over methods that solve the KS orbital eigenvalue problems for all electrons, the approach used by Gaussian. Additionally, within the PAW framework, LCAO can be used to realize greater computational efficiency. Rather than using large collections of plane waves, which are typically used in the PAW framework, LCAO uses smaller numbers of atomic-like basis functions to approximate wavefunctions [94]. This allows for faster calculations with only a small loss to overall accuracy. Ultimately, energy calculations using GPAW will most likely be less accurate than those performed with Gaussian, but they will be done in far less time. Additionally, the errors suffered within GPAW are systematic, meaning they would be common amongst similar structures and especially among like tetramers with monomers in different configurations. For this reason, GPAW was used to implement the GA designed to find the lowest energy tetramer. To ensure accurate dispersion effects were captured, a critical component of these clusters, the dispersion correction method of Tkatchenko and Scheffler, as implemented within GPAW, was used [97].

To create a tetramer, a single monomer is loaded into the ASE environment and copied three times. The three copies are rotated and translated in such a way as to produce an ideal tetrameric aluminum core with a given Al-Al interatomic distance. For the case of the Cp<sup>\*Ph</sup> variant the chosen distance was 2.8 Å, roughly the average Al-Al distance for the Cp<sup>\*iPr</sup> variant. All four monomers are then individually rotated about the axis through their respective Cp ring center. Each is rotated a random number of degrees and the number of degrees rotated is recorded into bins of 10 degrees. A set of four bins would describe the configuration of the tetramer. For example, a tetramer with a configuration of [0, 2, 18, 35] would represent a tetramer whose four monomers were rotated between 0–10 degrees, 20–29 degrees, 180–189 degrees and 350–359 degrees respectively. Order is important. The configuration [0, 18, 35, 2] would be an entirely different structure due to the order of rotation operations and the interaction of each monomer with its neighbors. The geometry of the created structure is then optimized using GPAW. This optimization tends to keep the monomers in their initial randomly

selected configuration, rotating only slightly before a local potential energy minimum is reached. Attempting to systematically check all possible monomer configurations would require optimizing 1,679,616 structures. The optimization of 100 structures takes about 1,800 hours with 72 CPUs. On a super computing cluster with multiple nodes and thousands of CPUs these structures can be optimized simultaneously. However, the cost of optimizing all 100 structures would be about 130,000 CPU hours, which represents more than 10% of the typical annual allotment of CPU time for research groups using DOD HPC resources. Investigating just 1% of the total possible structures would require nearly 22 million hours of CPU time and more than likely would only give about a 1% chance of finding the global minimum. In order to find the global minimum for the  $\text{Cp}^{*\text{Ph}}$  tetramer in a practical amount of CPU time, a GA in the spirit of Deaven and Ho was used [98]. There are six basic steps for this GA. First, create an initial group of randomly generated candidates. Second, select from these candidates the lowest energy structures to form an initial population. Third, preferentially select candidates from the population for pairing and create a new offspring. Fourth, mutate the offspring with some non-zero probability. Fifth, relax the offspring and include in the current population if the resulting energy is low enough. Finally, repeat the process until the global minimum has likely been found. The application of this process for the  $\text{Cp}^{*\text{Ph}}$  variant borrows heavily from the work of Vilhelmsen and Hammer on metal clusters [99].

#### (1) Starting Candidates

The initial set of randomly generated candidates should be as diverse as possible, but there is no rule of thumb as to how large the list should be. Vilhelmsen and Hammer were studying groups of metal clusters with less than 50 atoms. Random positions for each atom were chosen to create initial structures. This results in a significant number of degrees of freedom for each cluster, however it is very likely that several different configurations could be optimized into the global minimum as there are no constraints holding an atom in place other than the existence of neighboring atoms. The creation of a  $\text{Cp}^{*\text{Ph}}$  cluster only has four degrees of freedom, but it is much less likely for many different configurations to relax into the global minimum. For this reason, rather than an initial set of 20 candidates, as recommended by Vilhelmsen and Hammer, a set of 50 was

chosen [99]. To prevent creating similar candidates, the configuration of each structure, in terms of angular bins, was recorded and repeat configurations were rejected.

## (2) Creating Initial Population

A small population allows stronger candidates to mate more often, but lacks diversity. Vilhelmsen and Hammer found that small populations required less generations to reach a minimum, but the resulting minimum was less likely to be the actual global minimum [99]. A small population size was considered 10 candidates, while a large population was 40 candidates [99]. For this GA, an initial population of 15 was chosen, as speed was of primary importance. Additionally, it is not necessary to find the actual global minimum. As long as the resulting candidate was within a few kilojoules per mole of the actual global minimum then this would represent sufficient accuracy for ultimate monomer/tetramer equilibrium analysis. A population of the 15 lowest energy candidates among the entire set of structures is maintained throughout the entire GA run.

## (3) Selection of Mates

Within the population, it is important to preferentially select the most fitting candidates for mating. Randomly choosing two candidates will ultimately slow the GA's progression towards a global minimum. It is important to select a candidate based not on position in the population, but on actual strength of energy compared to the rest of the population. For this reason, the fitness equation used by Vilhelmsen and Hammer was adopted [99].

$$F_i = \frac{1}{2} [1 - \tanh(2\rho_i - 1)], \text{ with } \rho_i = \frac{E_i - E_{min}}{E_{max} - E_{min}}. \quad (10)$$

Here  $E_{min}$  is the energy of the lowest energy candidate in the population and  $E_{max}$  is the energy of the candidate with the highest energy in the population. The resulting fitness,  $F_i$ , ranges from 0.88 to 0.12 and is further adjusted by the number of times a candidate has been selected for mating,  $n_i$  [99]. The final probability of selection is:

$$P_i = F_i \cdot \frac{1}{\sqrt{1+n_i}}. \quad (11)$$

This construct preferentially selects the lowest energy candidates, but ensures that

particular candidates are not picked too many times. This helps to maintain diversity in the population.

#### (4) Pairing

Pairing of two selected mates is straightforward considering there are only four degrees of freedom for each structure. Each mate must contribute at least one monomer to the offspring. This results in only 14 possible combinations of monomers for the offspring. During a pairing, one of the 14 possible combinations is randomly selected and a new structure is created. The configuration of the structure is derived from the appropriate configuration numbers of the two mates. For example, two mates with configurations [0, 5, 18, 30] and [1, 6, 19, 31] could create offspring with configurations of [0, 5, 19, 31] or [1, 5, 19, 31], but not one with a configuration of [18, 19, 30, 31]. The resulting structure cannot be accepted until its configuration is compared to the configurations of all structures in the entire GA. If the configuration is a repeat the structure is rejected and another one of the 14 possible combinations for the two selected mates is tried. In the case of a mutation, the selected configuration is not eliminated and can be tried again. This continues until all 14 combinations are exhausted at which point the two mates are considered incompatible and new mates are chosen.

#### (5) Mutation

Mutations are a critical aspect of any GA. They introduce random diversity into the existing population. With no mutations, there is a risk of the entire population falling into a wide local minimum resulting in the GA's inability to find the global minimum. Mutating too often, however, introduces too much randomness into the population and adversely affects the GA's ability to progress towards the global minimum. For this work, a 30% mutation rate is used to match the rate used by Vilhelmsen and Hammer [99]. To accomplish this each of the four monomers are tested for mutation in turn. There is an 8.5% chance that a monomer would mutate, which results in an overall chance of any one of the four monomers mutating of 30%. Additionally, it is possible for more than one monomer to mutate. The mutation is a random rotation about the axis through the Cp center of the mutated monomer. The configuration of the new structure is

then updated based on which angular bin the mutated monomer would ultimately fall in after rotation.

#### (6) Optimization and Entry into Population

All structures are optimized to the nearest local minimum using GPAW. In order to take advantage of the volume of CPUs available on DOD HPC clusters, it is desirable to optimize as many structures simultaneously as possible. However, in an effort to extract the maximum efficiency of the GA, a departure from the approach of Vilhelmsen and Hammer is necessary to ensure a maximum number of generations. Therefore, a generational approach similar to that of Johnston's Birmingham cluster GA is employed [100]. A small group of offspring are selected and allowed to fully optimize. A new population is created, including newly relaxed offspring if appropriate. The members of this new population are then given fitness scores and another generation is selected. While there is no rule of thumb as to the number and size of generations necessary for optimal efficiency, a generation size of ten was chosen to allow for ten total generations by the time 150 structures were relaxed. This does not include generation 0, which would be the population created from the first fifty randomly created structures.

#### (7) Termination of the GA and Optimization in Gaussian

The goal was for the GA to narrow in on the global minimum within the first ten generations, or 150 total structures relaxed. For the  $\text{Cp}^{\text{*Ph}}$  variant, the lowest energy structure was produced during the fifth generation. By the end of the tenth generation the top ten structures, though initially configured differently, all optimized to virtually the same configuration. This configuration is shown in Figure 17(c) with Ph groups in place of the Pr groups. This is not surprising as it is logical that the Ph groups would prefer to settle into the gaps between adjacent ligands in a manner similar to that of the iPr groups in the  $\text{Cp}^{\text{*iPr}}$  variant. While it is impossible to know if the actual global minimum was found without an experimental crystal structure, based on the inclusion of mutations to prevent stagnation it is likely a structure very close to the global minimum, if not the global minimum, was in fact found. It is also clear that there are many different initial

configurations that would be capable of relaxing into the global minimum, making it easier to find.

To examine the performance of the GA, all of the randomly generated structures produced for the Cp<sup>\*Ph</sup> GA run as well as the GA runs for the three iPr variants discussed in the next section were compared to offspring produced by the GA. Histograms of both the random sampling and GA offspring were created and are shown in Figures 27 and 28 respectively. Relative energies with respect to the lowest energy structure found for each respective variant are plotted. The random sampling has a roughly normal distribution, as would be expected, and also fails to find the global minimum for any variant. The histogram of the GA offspring shows the remarkable ability of this approach to find significant numbers of low energy structures, increasing the chances of finding the global minimum. It is also important to note that more than 95 percent of the randomly generated structures were more than 25 kJ/mol higher in energy than the minimum found by the GA. Conversely, nearly 60 percent of the structures created by the GA were within 25 kJ/mol of the eventual minimum found. Ideally, the GA approach would be validated against a variant with an experimentally known structure. Unfortunately, there are only two variants for which there is experimental structural data, the Cp<sup>\*</sup> and the Cp<sup>^</sup> variants. The Cp<sup>\*</sup> is symmetric about rotation, so there would be thousands of degenerate configurations which would likely be found quite easily by just a random sampling of structures. Similarly, as previously mentioned, the Cp<sup>^</sup> is likewise insensitive to monomer rotation and therefore would not be a good test for the GA.

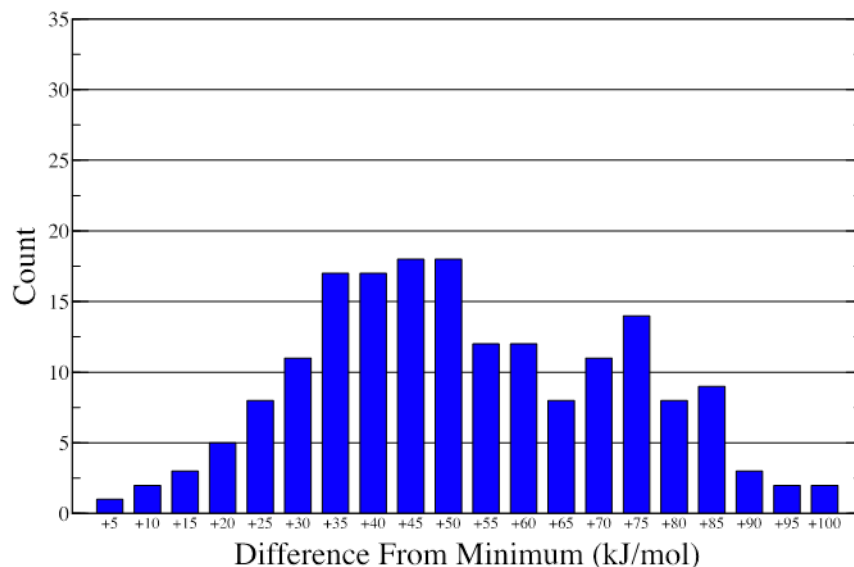


Figure 27. Histogram of calculated energy for randomly created structures.

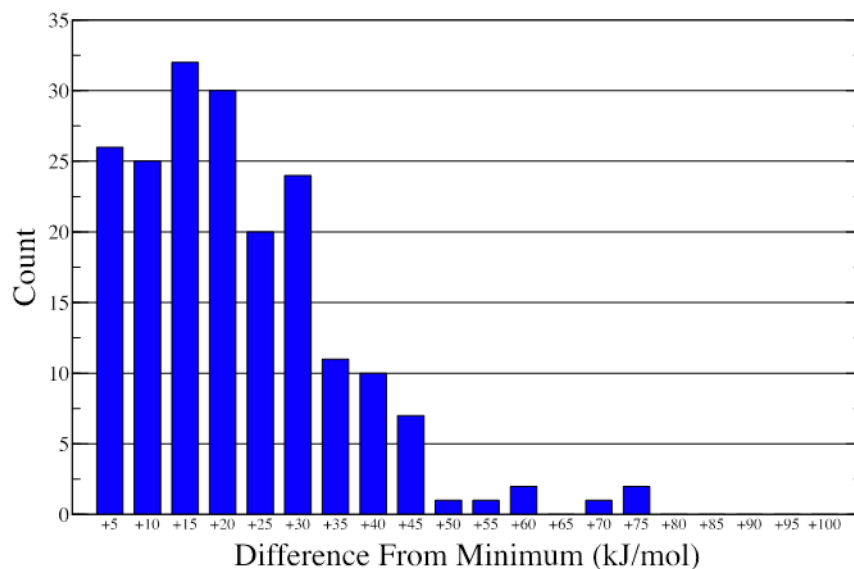


Figure 28. Histogram of calculated energy for structures produced by GA.

A sampling of structures from the GA were optimized in Gaussian with M06-2X and the split-valence double zeta basis set 6-31G(d). Results showed that GA structures within 4-5 kJ/mol of each other were essentially degenerate when optimized with Gaussian, even if they did not have the same configuration. Relative ranking for structures with larger energy differences, however, were preserved. Further optimization

of the lowest energy structure for the  $\text{Cp}^{*\text{Ph}}$  variant was done using the triple zeta cc-pVTZ basis set.

### ***b. NMR Results***

The inability to obtain crystals of the  $\text{Cp}^{*\text{Ph}}$  tetramer forces the reliance on  $^{27}\text{Al}$  NMR to identify the compound in solution. The  $\text{Cp}^*$  and  $\text{Cp}^\wedge$  tetramers have  $^{27}\text{Al}$  NMR chemical shifts of -82 ppm and -81 ppm respectively. They are the only two tetramers for which crystals have been obtained. The  $\text{Cp}^{*\text{Pr}}$  and  $\text{Cp}^{*\text{iPr}}$  variants never crystallized, but compelling thermochemical and DFT data suggest that the experimental signals of -86 ppm and -89 ppm were in fact the respective tetramers of these two variants. This would seem to indicate is that the  $^{27}\text{Al}$  NMR chemical shift for the  $\text{Cp}^{*\text{Ph}}$  variant should be relatively close to these numbers. The shift of -102.5 found by Buchin et al. in 2005 was too far from the signals of the known  $\text{Cp}^*$  and  $\text{Cp}^\wedge$  tetramers for them to definitively say that they had synthesized the  $\text{Cp}^{*\text{Ph}}$  tetramer [25]. David Morris from NAWC, China Lake, attempted to synthesize the  $\text{Cp}^{*\text{Ph}}$  tetramer using multiple routes and consistently detected a signal at -82 ppm. Buchin et al. used a synthesis process similar to that of Roesky [33], but with the halogen bromine instead of chlorine to improve yield [25]. Morris used the same synthesis method as Buchin et al. as well as the method of Fischer [63] reported on in 2013. It is unclear as to the discrepancy in  $^{27}\text{NMR}$  results, but DFT calculated NMR chemical shifts predict a shift of -84.7 ppm, indicating Morris has more than likely synthesized the tetramer. Additionally, variable temperature NMR data up to 100 degrees C contains only one signal at -82 ppm, indicating no monomers in solution.

### ***c. Thermochemistry and Equilibrium Constant***

Vibrational frequency analysis of the  $\text{Cp}^{*\text{Ph}}$  variant indicates that it is more enthalpically stable than the other six variants previously investigated. Calculated  $\Delta H_{tet}$  for the  $\text{Cp}^{*\text{Ph}}$  variant was -182.9 kJ/mol. This is significantly lower than the  $\Delta H_{tet}$  of the  $\text{Cp}^{*\text{Pr}}$  variant, -158.7 kJ/mol. The lower value of  $\Delta H_{tet}$  for the  $\text{Cp}^{*\text{Ph}}$  variant is consistent with its average Al-Al interatomic distance and with QTAIM analysis. The  $\text{Cp}^{*\text{Ph}}$  has a longer average Al-Al bond distance, and less  $\rho_b$  associated with Al-Al BCPs as compared with the  $\text{Cp}^{*\text{Pr}}$  variant. Total  $\rho_b$  associated with inter-ligand H-C and H-H

NCIs, however, is  $0.1640 \text{ \AA}^{-3}$  for the  $\text{Cp}^{*\text{Ph}}$  variant. This is almost 20 percent more than the total inter-ligand  $\rho_b$  calculated for the  $\text{Cp}^{*\text{Pr}}$  variant. Table 12 shows these metrics for both variants. The  $\text{Cp}^{*\text{Ph}}$  variant is another demonstration that weakening of the bonding in the aluminum core of a tetramer due to ligand hindrance can be offset by additional inter-ligand NCIs.

Table 12. Average Al-Al distance and  $\rho_b$  for the  $\text{Cp}^{*\text{Pr}}$  and  $\text{Cp}^{*\text{Ph}}$  variants.

	Al-Al dist	Total Al-Al $\rho_b$	Total H-H $\rho_b$	Total H-C $\rho_b$
$\text{Al}_4\text{Cp}^{*\text{Pr}}_4$	2.7670	0.2114	0.1242	0.0159
$\text{Al}_4\text{Cp}^{*\text{Ph}}_4$	2.8052	0.2046	0.0934	0.0706

\* Numbers are in  $\text{\AA}$  or  $\text{\AA}^{-3}$ .

Available thermochemical data now allows for an assessment of the relative monomer to tetramer ratio in solution as compared to the other six variants. Figure 29 shows a logarithmic plot of the monomer to tetramer ratio of the six variants previously discussed as well as the  $\text{Cp}^{*\text{Ph}}$  variant. All numbers were normalized to produce a monomer to tetramer ratio of 1:449 for the  $\text{Cp}^*$  variant, the known experimental value. The results show that the  $\text{Cp}^{*\text{Ph}}$  variant is distinct from the  $\text{Cp}^*$ ,  $\text{Cp}^{*\text{Et}}$ ,  $\text{Cp}^{*\text{Pr}}$  and  $\text{Cp}^{*\text{iPr}}$  variants, which all have roughly the same monomer to tetramer ratio. The  $\text{Cp}^{*\text{Ph}}$  variant is also distinct from the  $\text{Cp}^\wedge$  variant which has a much smaller monomer to tetramer ratio. The  $\text{Cp}^{*\text{Ph}}$  has a monomer to tetramer ratio almost identical to that of the  $\text{Cp}$  variant, a variant for which monomers are not found in solution. Due to reasons previously discussed, this type of analysis can only inform of relative trends. The analysis suggests that the  $\text{Cp}^{*\text{Ph}}$  variant is likely to have a significantly smaller monomer to tetramer ratio compared to the  $\text{Cp}^*$ ,  $\text{Cp}^{*\text{Et}}$ ,  $\text{Cp}^{*\text{Pr}}$  and  $\text{Cp}^{*\text{iPr}}$  variants and a significantly higher monomer to tetramer ratio as compared with the  $\text{Cp}^\wedge$  variant. Based on experimental equilibrium data for the  $\text{Cp}^*$ ,  $\text{Cp}^{*\text{Pr}}$ ,  $\text{Cp}^{*\text{iPr}}$ ,  $\text{Cp}$  and  $\text{Cp}^\wedge$  variants, a definitive conclusion with respect to monomers in solution for the  $\text{Cp}^{*\text{Ph}}$  variant cannot be made. However, the results calculated with DFT and shown in Figure 29 are consistent with the fact that monomers of the  $\text{Cp}^{*\text{Ph}}$  were not found in solution by two different experimental groups, even at

elevated temperatures. The fact that the calculated ratio for the  $\text{Cp}^{*\text{Ph}}$  variant would fall so much lower than the ratio for the  $\text{Cp}^*$ ,  $\text{Cp}^{*\text{Et}}$ ,  $\text{Cp}^{*\text{Pr}}$  and  $\text{Cp}^{*\text{iPr}}$  variants is surprising considering that the  $\text{Cp}^{*\text{Ph}}$  carries with it significantly more bulk. As QTAIM analysis has shown, though, this bulk is not steric and makes non-trivial contributions to stability that bind the  $\text{Cp}^{*\text{Ph}}$  variant more strongly than other less bulky variants. Adding bulk is not sufficient to increase the monomer/tetramer ratio in solution due primarily to the small effect on Al-Al distance. It is likely that continued stretching of the Al-Al distance with more ligand hindrance is needed to degrade aluminum bonding in the core. To get a qualitative look at this effect, analysis with the electron localization function (ELF) is conducted.

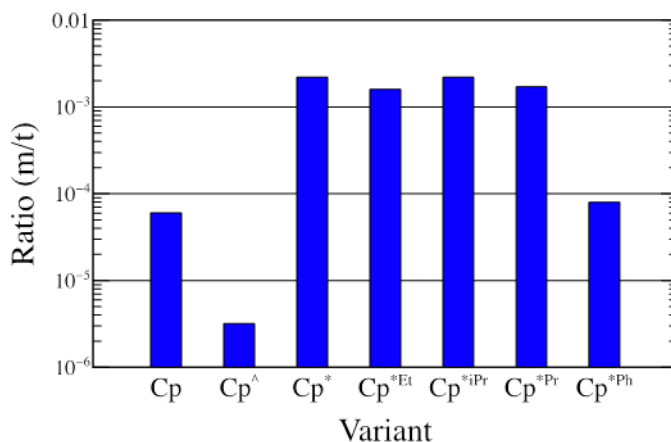


Figure 29. Logarithmic plot of normalized monomer/tetramer ratio for seven different Cp variants.

#### *d. ELF Analysis*

First introduced by Becke and Edgecombe, ELF is a topological analysis of a molecule based on likely locations of electron pairs [101]. ELF takes advantage of the Pauli exclusion principle which prevents electrons of the same spin from occupying the same region of space [102]. Using the electron pair density function, which determine the probability of finding two electrons of the same spin in given regions of space, one can determine where pairs of electrons of opposite spins are localized. Because of the Pauli exclusion principle, a high probability of finding two electrons of the same spin

corresponds to regions where electrons are delocalized [103]. Conversely, a low probability of finding two electrons of the same spin corresponds to regions where electrons are well localized [103]. For a closed shell system where all molecular orbitals are doubly occupied, as is the case for all clusters studied in this work, regions of high electron localization would correlate to locations of electron pairs of opposite spins. ELF results are scaled such that they run from zero to one. High values correlate to regions of high electron pair localization and low values corresponds to regions of low pair localization. A value of 0.5 corresponds to the localization of electrons in a uniform electron gas. The results help to connect the electron density with Lewis' concept of the electron pair. Figure 30 shows the ELF results for the AlCp monomer with a 0.75 isosurface displayed. The graphic gives an intuitive picture of the behavior of the electron pairs and their involvement with chemical bonding. The red, blue and green surfaces display behavior of valence electrons and the cyan surfaces show core shells. The red surface corresponds to  $\sigma$  bonds connecting hydrogen and carbon atoms. The green surface corresponds primarily to  $\pi$  bonds between carbons, but also includes a single electron from the aluminum atom. The blue surface corresponds to the lone pair from the aluminum atom. Finally, the cyan surfaces close to the atomic centers are core shells. The carbon atoms have a single core shell, the K shell. The aluminum atom has two core shells, the K and L shells.

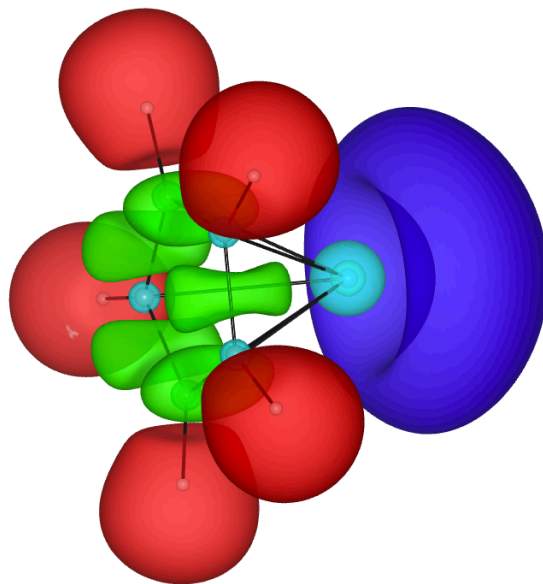


Figure 30. ELF for AlCp monomer with the 0.75 isosurface displayed.

The ELF for the Cp-type tetramers is very similar for the ligand groups with clear bonding regions around hydrogen atoms and between carbon atoms. The ELF in the core is more complex. Figure 31 shows the 0.79 isosurface ELF data for the Cp, Cp<sup>^</sup>, Cp<sup>\*</sup>, Cp<sup>\*Pr</sup>, Cp<sup>\*Ph</sup> and Cp<sup>\*iPr</sup> variants spherically clipped so that only data within 4.5 Å of the center of the aluminum tetrahedron core is visible. The ELF surfaces for the two aluminum core shells have also been excluded. Included are average Al-Al bond distances for each variant. For a better understanding of the significance of the surface shapes, ELF bifurcation analysis is conducted.

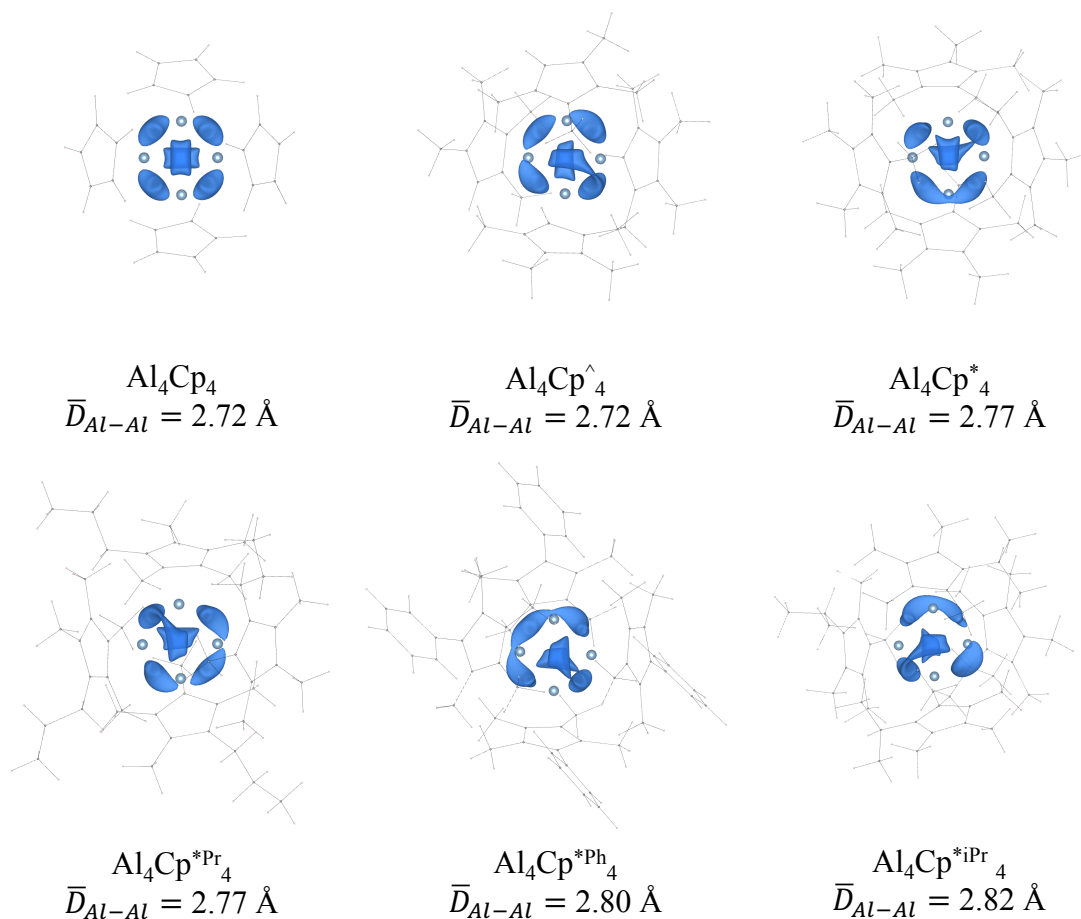
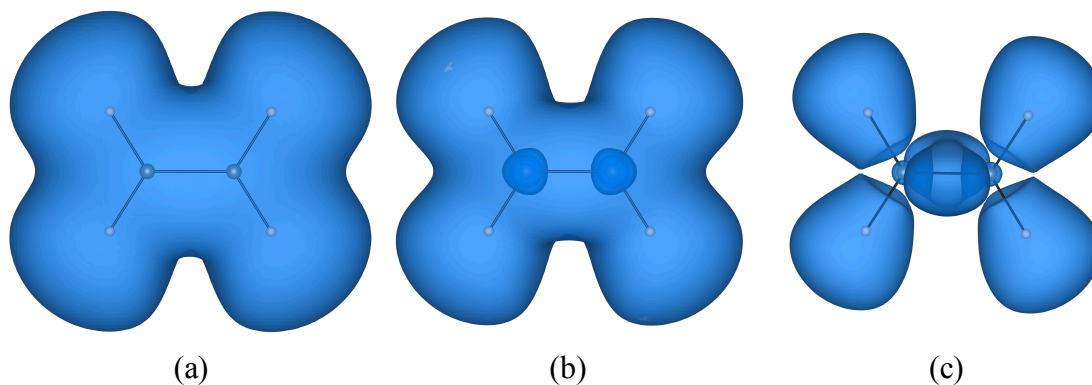


Figure 31. ELF for aluminum core of six Cp-type variants with the 0.79 isosurface displayed.

In order to understand bifurcation, it is necessary to understand the concept of an attractor and a basin in ELF. Attractors are essentially maxima on the ELF surface. Basins are related to attractors and are defined as the region of space within which the gradient of the ELF surface points towards a given attractor. In Figure 30 there are 17 attractors and 17 basins surrounding those attractors. Bifurcation is the study of so-called  $f$ -localization domains, which are volumes enclosed by ELF isosurfaces of a given value,  $f$  [104]. Figure 32(a) depicts the ELF of  $\text{C}_2\text{H}_4$  with an  $f$  value of 0.05 which is relatively close to zero. At this level, there is only one domain. It encloses all eight attractors in the molecule: the two carbon core attractors and the six valence attractors corresponding to the four  $\sigma$  bonds and the two attractors associated with the double  $\pi$  bond. As the  $f$  value

is increased, the domain will shrink and will eventually bifurcate. In the case of  $C_2H_4$  the first bifurcation is at about  $f = 0.15$  at which point the single domain splits into three domains, Figure 32(b). Two domains are considered irreducible because they enclose only one attractor, the center of each carbon atom. The third domain is considered reducible because it encloses more than one attractor [105]. The next bifurcation is when  $f = 0.66$  and corresponds to the point when the remaining reducible domain splits into five domains, Figure 32(c). Four domains contain the four H-C valence attractors and the fifth domain contains the two attractors associated with the C-C double bond. The final bifurcation, not shown in Figure 32, occurs at  $f = 0.93$  when the domain containing the two attractors associated with the C-C double bond splits in two. Bifurcation analysis helps understand the relative electron localization between basins. The lower the bifurcation point for a given attractor, the more localized the electrons are within the associated basin [104].



Isosurface values: (a)  $f = 0.05$ ; (b)  $f = 0.15$ ; (c)  $f = 0.66$ .

Figure 32. Three ELF isosurface values illustrating bifurcation.

Figure 31 shows aluminum core bonding at various bifurcation levels. The core of the Cp variant shows six clearly distinguishable domains enclosing the six Al-Al valence attractors. These domains are all irreducible and indicate a high level of localization compared with the other five variants. This would suggest that the Cp variant has the strongest Al-Al core bonding. The  $Cp^{\wedge}$  compound shows a slight merging of two domains creating a single reducible domain that indicates a slight electron pair delocalization as

compared with the Cp variant. This is interesting considering that the Cp and Cp<sup>^</sup> variants have virtually the same average Al-Al distance. Insight gained through ELF could suggest that the Al-Al bonding in the core of the Cp<sup>^</sup> variant is marginally weaker than that of the Cp variant, despite similar Al-Al distances. This is consistent with QTAIM analysis which shows slightly more  $\rho_b$  associated with Al-Al BCPs in Cp variant. The Cp<sup>\*</sup> and Cp<sup>\*Pr</sup> variants show additional signs of delocalization as compared to the Cp and Cp<sup>^</sup> variants. Both have similar average Al-Al distances and both show the presence of reducible domains. There are two reducible domains present in the core of the Cp<sup>\*</sup> variant and only one in the core of the Cp<sup>\*Pr</sup> variant. The two domains on the right of the core of the Cp<sup>\*Pr</sup> variant, however, are on the verge of merging and will in fact merge if  $f$  is lowered to 0.78. Additionally, the irreducible domains show signs of distortion as compared to the Cp variant, indicating some electron pair delocalization. The Cp<sup>\*Ph</sup> and Cp<sup>\*iPr</sup> variants have the largest Al-Al distances of any of the variants and also show the most amount of distortion of Al-Al valence domains. The Cp<sup>\*Ph</sup> variant has a reducible domain containing three attractors and though the three irreducible domains at the bottom right of the core have not merged yet, they will at  $f = 0.78$ . The Cp<sup>\*iPr</sup> shows two reducible and two irreducible domains, similarly to the Cp<sup>\*</sup> variant, but with significant distortion of all domains as compared to the Cp<sup>\*</sup> variant. These two variants clearly have the most amount of electron delocalization of the six clusters examined and therefore most likely have the weakest Al-Al bonding in the core. This ELF analysis, while qualitative, provides insight into metal bonding in the core that compliments QTAIM.

Analysis of domains, particularly at low  $f$  values, has also been used to study phenomenon not directly captured by ELF such as NCIs. Covalent bonds between atoms are easily identified with ELF due to the existence of an attractor between atoms, as is the case for C<sub>2</sub>H<sub>4</sub>. The enclosed volume between the two carbon atoms in Figure 32(c) encloses the valence attractors associated with the double  $\pi$  bond in the molecule. NCIs, however, cannot be identified by attractors as none will exist between the interacting atoms. Work by Massobrio et al. showed that NCIs could be identified by examining where distinct domains join as  $f$  is decreased [106]. They showed that NCIs between OH<sup>-</sup> and NO<sub>3</sub><sup>-</sup> in copper hydroxonitrate could be identified by the joining of the domains of

each molecule at  $f$  values of about 0.15. To illustrate this point, ELF calculations were conducted on a typical  $\beta$ -turn of a protein. Proteins are long strings of amino acids, but here only the turn is investigated and connections to the remainder of the protein chain were truncated with hydrogen atoms. Figure 33 shows the ELF of the  $\beta$ -turn at an  $f$  value of 0.06. There is only one domain encompassing all attractors in the molecule, but the left and right regions of the domain join precisely between an oxygen atom and a hydrogen atom. This identifies a known NCI that is the primary reason the  $\beta$ -turn exists and ultimately results in the common folding behavior of large proteins [107].

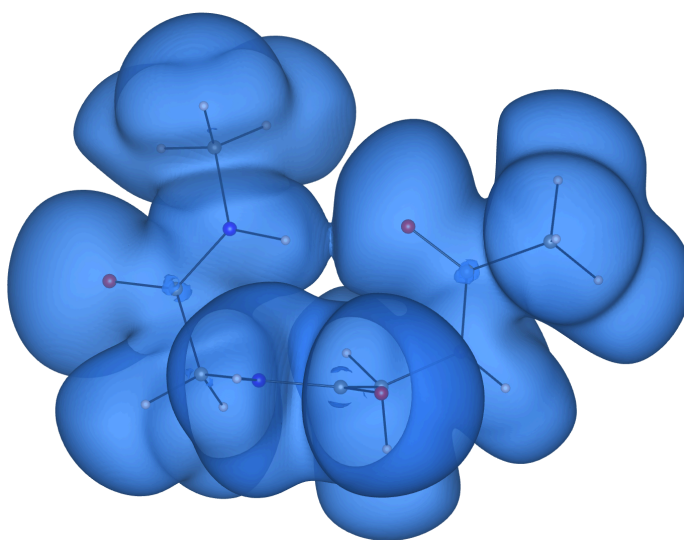


Figure 33. ELF 0.06 isosurface showing NCI between hydrogen and oxygen atoms in a  $\beta$ -turn of amino acids.

The connecting of separate domains as well as the connecting of separate regions of the same domain both occur within all Cp-type variants. Figure 34 shows two neighboring ligands of the Cp<sup>\*Ph</sup> variant with most of the ELF isosurface clipped out for clarity. The isosurface corresponds to  $f = 0.03$ . Highlighted with the red circle is an inter-ligand connection between the separate domains of the two ligands. This connection is associated with an NCI between a Me hydrogen atom from the lower ligand and a Me carbon atom from the upper ligand. This also correlates with an H-C BCP discovered through QTAIM analysis. Highlighted with green circles are intra-ligand connections

between two regions of the domains surrounding each ligand. The connections are between Me hydrogen atoms and Ph carbon atoms from the same ligand. Both also correlate with QTAIM H-C BCPs. This would suggest that connections between separate domains or between separate region of the same domain can indicate bone-fide NCIs.

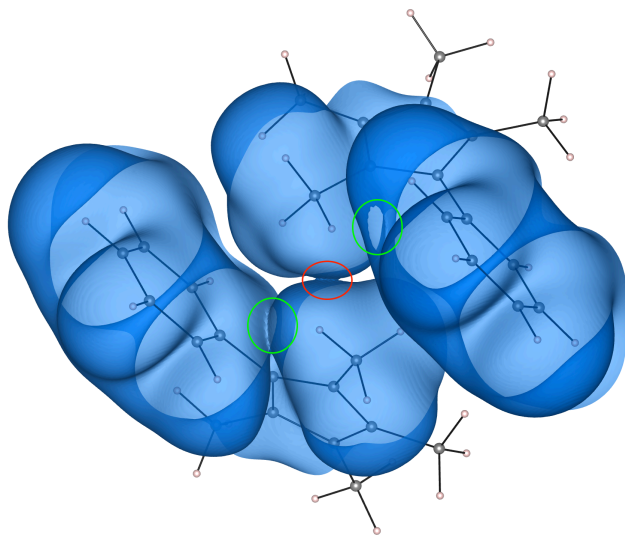


Figure 34. ELF 0.03 isosurface showing inter-ligand connection (red circle) and intra-ligand connections (green circles) of domains in  $\text{Cp}^{*\text{Ph}}$  variant.

## 2. Other Isopropyl Variants

Because the addition of bulk, in general, does not lead to a higher monomer to tetramer ratio for Cp-type clusters, three variants that have functional groups which may hinder bonding in the aluminum core are examined. Investigation of these variants was suggested by researchers at the China Lake NAWC. They are based on the  $\text{Cp}^{*\text{iPr}}$  variant and all have the form  $\text{AlCp}^{\text{niPr}}$  ( $\text{Cp}^{\text{niPr}} = \text{C}_5\text{iPr}_n\text{H}_{(5-n)}$ ;  $n=3,4,5$ ). The  $\text{Cp}^{*\text{iPr}}$  variant has the largest Al-Al average bond distance in the core of the tetramer and despite being one of the most enthalpically stable variants, it has the highest experimental monomer to tetramer ratio of any variant previously discussed. All three  $\text{Cp}^{\text{niPr}}$  variants were subjected to the same theoretical structural and thermochemical analysis as the  $\text{Cp}^{*\text{Ph}}$  and their potential monomer/tetramer ratios calculated.

*a. Triisopropyl Variant*

Before attempting to find the lowest energy tetrameric configuration for the  $\text{Cp}^{3\text{iPr}}$  variant, DFT analysis into the monomer was conducted. There are two stable directions the lone hydrogen atom of the iPr functional group can point in the monomer. The monomer, aluminum (I) 1,2,4-triisopropylcyclopentadienide, has iPr groups on the ligand at the 1, 2 and 4 positions. For the iPr group at position 4, a change in direction has no impact on ground state energy. This leaves four possible combination of directions for the two remaining groups. Due to symmetry only three of these configurations are distinct. Ground state energies for all three types were calculated with M06-2X/cc-pVTZ and the configuration shown in Figure 35 was found to be 6.5 kJ/mol lower in energy than the next closest configuration. For this reason, tetramers created with this monomer were ultimately used for the GA.

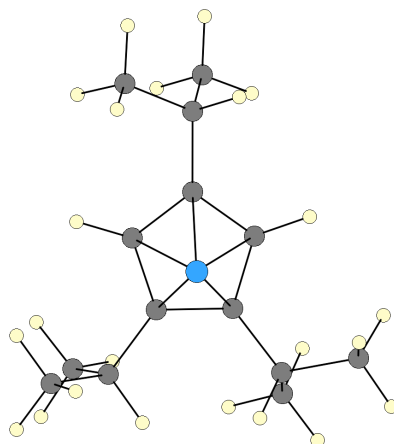


Figure 35. Lowest energy configuration of the  $\text{AlCp}^{3\text{iPr}}$  monomer.

The lowest energy structure for the  $\text{Cp}^{3\text{iPr}}$  tetramer calculated via the GA found the lowest structure in the 9<sup>th</sup> generation, though this structure was only 0.13 kJ/mol lower in energy than the previous lowest structure discovered in the 5<sup>th</sup> generation. The minimum found by the GA was relaxed using M06-2X/cc-pVTZ in Gaussian. Surprisingly, the average Al-Al distance for this variant was 2.746 Å, making it slightly more compact than the  $\text{Cp}^*$  variant and significantly more compact than the  $\text{Cp}^{*\text{iPr}}$

variant. The inter-ligand dispersive forces due to the extra bulk are likely strong enough to overcome the hindrance of the *iPr* functional groups and pack the aluminum core closer than expected. This produces a synergistic effect whereby the additional stability gained through inter-ligand NCIs actually forces aluminum atoms closer which, in turn, increases the stability gained through Al-Al bonding. This is reflected in the calculated  $\Delta H_{tet}$  value of -181.1 kJ/mol. This makes it slightly less stable than the  $\text{Cp}^{*Ph}$  variant which has an  $\Delta H_{tet}$  value of -182.9 kJ/mol.

ELF analysis of the  $\text{Cp}^{3iPr}$  variant indicates very localized bonding in the aluminum core. Figure 36 shows the Al-Al valence ELF isosurface with  $f = 0.79$ . The  $\text{Cp}^{3iPr}$  variant has six distinct irreducible domains surrounding the six Al-Al bond attractors. The core of this variant looks very similar to the core of the  $\text{Cp}$  variant and more localized than even the  $\text{Cp}^\wedge$  which has a smaller average Al-Al distance. It would appear that despite having a larger average Al-Al distance, the aluminum bonding in the core of the  $\text{Cp}^{3iPr}$  variant may be stronger than that of the  $\text{Cp}^\wedge$  variant.

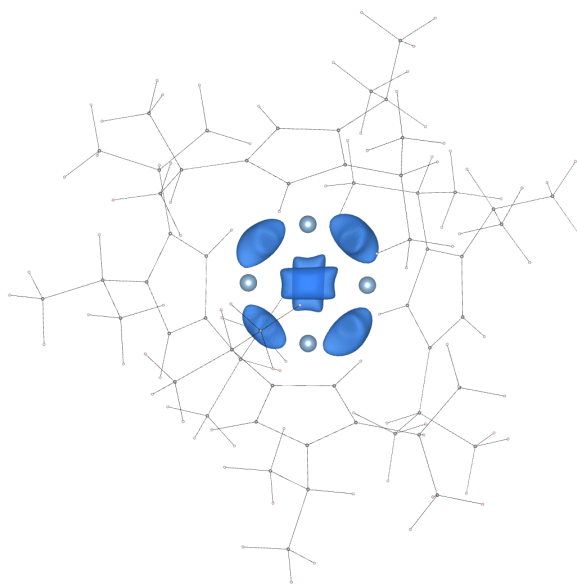


Figure 36. ELF for aluminum core of the  $\text{Cp}^{3iPr}$  tetramer with the 0.79 isosurface displayed

### b. *Tetraisopropyl Variant*

There are several different configurations of the  $\text{Cp}^{4\text{iPr}}$  monomer. The four iPr groups can be arranged in 16 different configurations. Due to symmetry, only eight are distinct. The ground state energies for all eight configurations were calculated with M062X/cc-pVTZ. The lowest energy configuration is shown in Figure 37 and was ultimately used to create tetramers for the GA. The  $\text{Cp}^{4\text{iPr}}$  proved to be much more difficult to pack together than the  $\text{Cp}^{3\text{iPr}}$  variant. After ten generations of the GA, the lowest energy structure was optimized in Gaussian and found to have an average Al-Al bond distance of 3.4567 Å, making the Al-Al core bonding significantly weaker than all previous variants.

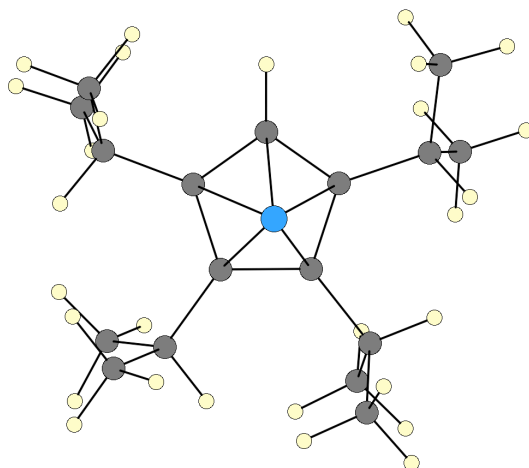


Figure 37. Lowest energy configuration of the  $\text{AlCp}^{4\text{iPr}}$  monomer.

The calculated  $\Delta H_{tet}$  for the  $\text{Cp}^{4\text{iPr}}$  variant is -72.9 kJ/mol, making this by far the least enthalpically stable variant. This result is primarily due to the increased average Al-Al bond distance. QTAIM analysis indicates that the Al-Al bonds here are distinct from those of the other clusters analyzed. All six Al-Al BCPs are associated with a  $\nabla^2\rho_b > 0$ , which is unique for this variant, and a relatively low total value of  $\rho_b$ , 0.0840. All other variants have  $\nabla^2\rho_b < 0$  and an average total  $\rho_b$  of 0.2127 at Al-Al BCPs. A  $\nabla^2\rho_b > 0$  combined with a relatively low value of  $\rho_b$  at a BCP is an indication of local charge

depletion which is typically associated with NCIs [108]. As Bone and Bader point out, however, a  $\nabla^2\rho_b < 0$  is not a necessary indicator of a covalent bond [85]. The Al-Al BCPs for the  $\text{Cp}^{4\text{iPr}}$  variant are also associated with  $H_b < 0$ , a kinetic energy per density ratio ( $G_b/\rho_b$ ) much less than 1 and  $|V_b| > G_b$ . These are characteristics typically associated with covalent bonding [82]. The unique nature of this bonding is also reflected in ELF analysis of the aluminum core. Figure 38 shows core ELF isosurfaces for three different  $f$  values. With  $f = 0.76$  it is clear that the six Al-Al valence attractors present in all other variants are non-existent. The surfaces seen in Figure 38 are those enclosing the four attractors associated with the lone pair of electrons associated with each aluminum atom. Connections between the four domains begins as  $f$  is reduced through 0.47. This is seen in the middle image of Figure 38 where the domains of the two rearward Al atoms have joined. Connections between all aluminum atoms is achieved when  $f = 0.36$ . Each aluminum domain is connected to the domains of other three aluminum atoms creating six distinct connections analogous to the six valence attractors present in each of the previous eight clusters examined. Connections between aluminum domains occurring between  $f = 0.36$  and  $f = 0.47$  are below the typical value of  $f > 0.5$  associated with covalent bonds [109]. This, in addition to QTAIM analysis, suggests that describing aluminum lone pair overlap in the core of the  $\text{Cp}^{4\text{iPr}}$  variant as covalent is tenuous.

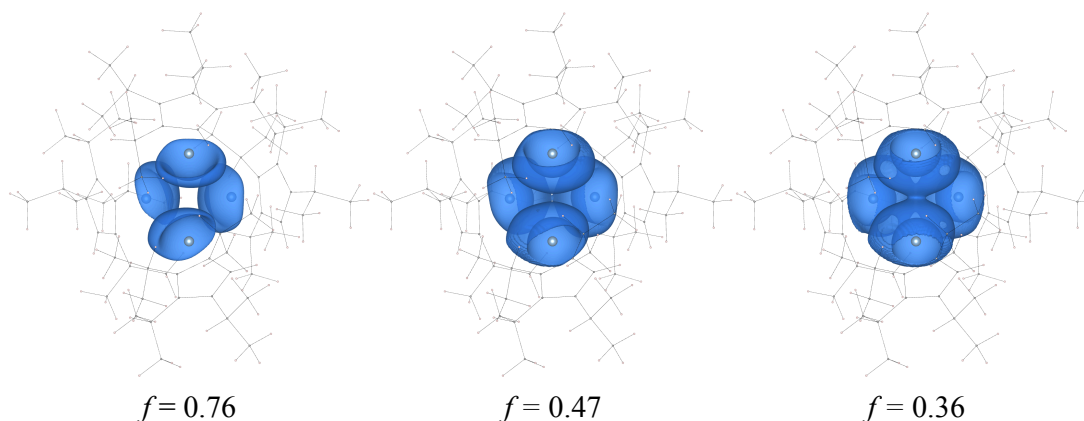


Figure 38. ELF for aluminum core of the  $\text{Cp}^{4\text{iPr}}$  tetramer.

*c. Pentaisopropyl Variant*

The  $\text{Cp}^{5\text{iPr}}$  monomer has an iPr group attached to every carbon site on the Cp ring. For this reason, all iPr groups must be orientated in the same direction. Switching the orientation of one group results in about a 25 kJ/mol increase in ground state energy, and switching multiple groups results in even higher energy changes. This leaves two possible configurations for the  $\text{Cp}^{5\text{iPr}}$  monomer, but they are degenerate. The configuration used for to build tetramers for the GA is shown in Figure 39. Despite a run that included 15 generations and more than 200 structures, the GA never produced a  $\text{Cp}^{5\text{iPr}}$  variant with an average Al-Al distance smaller than 4.9 Å. This is well outside the Al-Al bonding region and all subsequent attempts to optimize top GA candidates in Gaussian failed. The addition of the fifth iPr group to each monomer appears to have provided enough hindrance to prevent aluminum lone pair overlap and as a consequence no stable tetramer was found. While synthesis of the monomer is possible, as Fischer's reductive elimination method produces monomers directly [63], it is unclear if larger metalloid clusters would be stable without a stable tetramer for this variant. Much is unknown about the growth process of clusters in solution, however, and it is possible that cluster growth routes which do not involve the tetramer may exist.

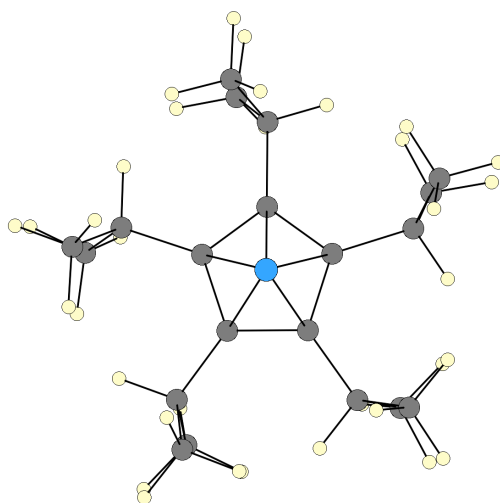


Figure 39. Lowest energy configuration of the  $\text{AlCp}^{5\text{iPr}}$  monomer.

*d. Equilibrium Constants for Cp<sup>niPr</sup> Variants*

The three iPr variants just discussed have a steady progression of increasing steric bulk and hindrance preventing short Al-Al bond distance. The variant with the smallest amount of bulk, Cp<sup>3iPr</sup>, is the most enthalpically stable due primarily to the fact that, despite its bulk, it has an average Al-Al bond distance even smaller than those of the Cp\* variants. The hindrance of Cp<sup>4iPr</sup> and Cp<sup>5iPr</sup> variants, however, force much larger Al-Al bond distances and in the case of the Cp<sup>5iPr</sup> variant, likely prevent the existence of a stable tetramer. Figure 40 shows a logarithmic plot of monomer/tetramer ratios for the Cp, Cp\*, Cp<sup>\*Ph</sup>, Cp<sup>3iPr</sup> and Cp<sup>4iPr</sup> variants normalized so that the ratio for the Cp\* variant is 1:449, the known experimental ratio. Results indicate that the monomer to tetramer ratio for the Cp<sup>3iPr</sup> variant would fall between that of the Cp\* and Cp<sup>\*Ph</sup> variants. Whether or not monomers for this variant would be found in solution is inconclusive. The Cp<sup>4iPr</sup> variant, however, has a much lower calculated equilibrium constant and therefore a much higher monomer to tetramer ratio. The ratio of the Cp<sup>4iPr</sup> variant is actually higher than all other variants examined and is that only variant with more monomers than tetramers in solution. This likely makes it the best precursor for larger metalloid clusters.

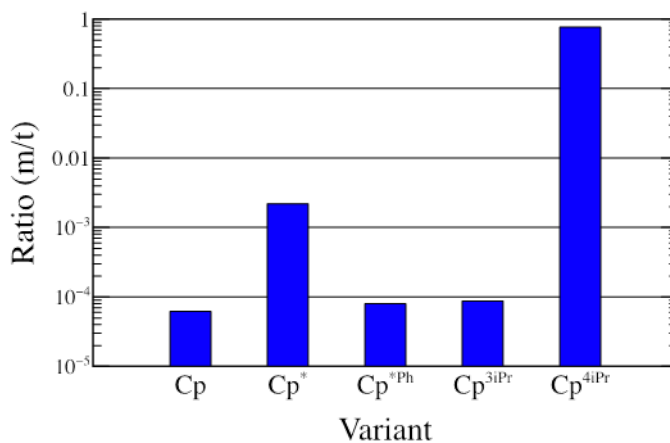


Figure 40. Logarithmic plot of monomer/tetramer equilibrium ratios for Cp, Cp\*, Cp<sup>\*Ph</sup>, Cp<sup>3iPr</sup> and Cp<sup>4iPr</sup> variants.

THIS PAGE INTENTIONALLY LEFT BLANK

## IV. CONCLUSION

Large metalloid clusters such as  $\text{Al}_{50}\text{Cp}^*_{12}$  show enormous potential as novel energetic materials. Theoretical heats of combustion suggest that these clusters have very high energy density compared to explosives, but their small size and core/shell structure may allow for much more rapid combustion kinetics than standard metal fuels. In this work, computational analysis of several small, prototypical monovalent aluminum clusters was performed with the ultimate goal of developing novel energetic materials. DFT calculations show that the predicted thermochemistry is extremely sensitive to the functional choice, both due to the prominence of non-covalent interactions between ligands and DFT inaccuracies in treating the low-valent Al bonding in the core. Calculated results compared with available experimental thermochemical data for three different AlCp-based variants indicate the necessity to account for short and medium range dispersive forces. This work demonstrates that the Minnesota functional M06-2X, specifically parameterized to capture these effects, is an exceptional method for calculating key characteristics of these clusters. It predicted enthalpies of tetramerization within 2% of experimental values and geometrical parameters to better than 1% of available data when paired with the triple zeta, cc-pVTZ basis set. This work also demonstrates that M06-2X is more accurate and computationally expedient than methods that used additional calculations to explicitly treat dispersive interactions.

Using a GA and M06-2X, the lowest-energy structures of ten AlCp-based clusters with varying amounts of steric bulk were determined. Thermochemical analysis indicated the addition of steric bulk on the Cp ligands tends to stabilize these clusters enthalpically, primarily via NCIs across ligand groups. QTAIM analysis shows that there is a strong correlation between inter-ligand BCPs and overall stability of the tetrameric form. Additionally, for all variants except the unsubstituted AlCp variant, covalent Al-Al bonding in the tetrahedral core accounted for only about 65% of the overall enthalpic stability of the tetramer. Equilibrium analysis, however, reveals no trend between ligand steric bulk and monomer to tetramer equilibrium. The two variants with the least amount of steric bulk have by far the lowest monomer to tetramer ratio. The  $\text{Cp}^{\text{*Ph}}$  variant,

however, has the lowest ratio of monomer to tetramers amongst all the Cp\* variants, despite having the most steric bulk. Additional steric bulk seems to only increase monomer to tetramer ratio when the bulk interferes with Al-Al covalent bonding in the tetrahedral core. The addition of a single iPr group to the Cp<sup>3iPr</sup> variant is sufficient to force the average Al-Al distance further apart by approximately 0.6 Å. The resulting variant, Cp<sup>4iPr</sup>, has a tetramer with the most steric bulk of any examined, but also with the second weakest enthalpy of tetramerization. This reduction in stability produces the highest monomer to tetramer ratio of all variants, making it a good candidate for solution-based synthesis techniques.

DFT with M06-2X revealed that there is no trend relating bulk and monomer to tetramer ratio in solution. Each potential cluster must be examined individually. The hope is that cluster variants with large numbers of monomers in solution will provide the building blocks needed to produce larger systems analogous to Al<sub>50</sub>Cp\*<sub>12</sub>. Other avenues to large metalloid clusters are likely possible and should be pursued. The ultimate goal is to passivate aluminum atoms with specifically designed organic ligands to create clusters with accelerated combustion kinematics compared to much larger aluminum particles that are typically added to high explosives.

Beyond metalloid cluster synthesis, it is also important to continue to examine potential stabilizing ligands. The ligands examined in the work contain no oxidizing agents. Aluminum combustion would require the addition of an oxidizer to the eventual explosive compound produced. Ligands whose bulk includes multiple nitro groups, for example, would allow for the inclusion of some oxidizing agent as part of the cluster. This would reduce the amount of external oxidizer required. Synthesizing metalloid clusters passivated with fluorinated monomers such as AlCp<sup>\*5F</sup> (Cp<sup>\*5F</sup> = C<sub>5</sub>(CF<sub>3</sub>)<sub>5</sub>) could create material with enough oxidizer for the entire core of aluminum atoms, potentially eliminating the need for an added oxidizer. Theoretical analysis of these and other types of ligands will help determine their effect on tetrameric stability as well as the viability of these tetramers to produce larger clusters.

## APPENDIX A. COMPUTATIONAL METHODOLOGY

DFT calculations of all compounds were carried out using the Gaussian G09.E01 and G16.A03 software [110], [111]. All calculations used an ultra-fine grid and systems were relaxed until no imaginary vibrational frequencies were found. Basis set superposition error analysis was done using a counterpoise methodology [112]. Solvent corrections were made using the conductor-like screen model (COSMO) as implemented in the Polarizable Continuum Model (PCM) framework for Gaussian [113], [114]. Calculations which include explicit dispersion corrections were done using Grimme's D3 approach [54]. Bond critical points and associated density metrics were determined using the DGrid software [115]. In order to calculate  $^{27}\text{Al}$  NMR chemical shifts, known experimental NMR values were plotted against the isotropic output from a GIAO calculation scaled by the 0 ppm reference,  $\text{Al}(\text{H}_2\text{O})_6^{3+}$  [116]. ELF analysis was done using the TopMoD software [117]–[119]. All calculations were performed on DOD HPC computer clusters.

THIS PAGE INTENTIONALLY LEFT BLANK

## APPENDIX B. ADDITIONAL PUBLICATIONS

The following publications resulted from this dissertation work:

S. Vaddypally, I. G. McKendry, W. Tomlinson, J. P. Hooper, and M. J. Zdilla, "Electronic structure of manganese complexes of the redox-non-innocent tetrazene ligand and evidence for metal-azide/imido cycloaddition intermediate," *Chem. Eur. J.*, vol. 22, pp. 10548-10557, 2016.

S. DeCarlo, D. H. Mayo, W. Tomlinson, J. Hu, J. P. Hooper, P. Zavalij, K. Bowen, H. Schnöckel, and B. Eichhorn, "Synthesis, structure and properties of  $\text{Al}(\text{R}^t\text{bpy})_3$  complexes (R=*t*-Bu, Me): Homoleptic maingroup tris-bipyridyl compounds," *Inorg. Chem.*, vol. 55, pp. 4344-4353, 2016.

J. R. Hemmer, S. O. Peolma, N. Treat, Z. A. Page, N. D. Dolinski, Y. J. Diaz, W. Tomlinson, K. D. Clark, J. P. Hooper, C. Hawker, and J. R. Alaniz, "Tunable visible and near infrared photoswitches", *J. Am. Chem. Soc.*, vol. 138, pp. 13960-13966, 2016.

W. Tomlinson, D. H. Mayo, R. M. Wilson, and J. P. Hooper, "The role of steric bulk in new monovalent aluminum compounds," *J. Chem. Phys. A.*, vol. 121, no. 24, pp. 4678-4687, 2017.

THIS PAGE INTENTIONALLY LEFT BLANK

## LIST OF REFERENCES

- [1] R. Helmut and S. Braun, “High explosives containing ultrafine aluminum ALEX,” *Propellants, Explos., Pyrotech.*, vol. 22, pp. 311–314, 2001.
- [2] W. A. Trzciński, S. Cudziło, and L. Szymańczyk, “Studies of detonation characteristics of aluminum enriched RDX compositions,” *Propellants, Explos., Pyrotech.*, vol. 32, no. 5, pp. 392–400, 2007.
- [3] P. C. Soures, “A library of prompt detonation reaction zone data,” LLNL, Livermore, Ca., UCRL-ID-130055 Rev 1, Jun. 1998.
- [4] E. L. Baker, W. Balas, C. Capellos, J. Pincay, and L. Stiel, “Combined effects aluminized explosives,” ARDEC, Picatinny Arsenal, NJ, Tech. Rep. ARMET-TR-10007.
- [5] H. Yang and W. Yoon, “Modeling of aluminum particle combustion with emphasis on the oxide effects and variable transport properties,” *J. Mech. Sci. Technol.*, vol. 24, no. 4, pp. 909–921, 2010.
- [6] T. Bazyn, N. Glumac, H. Krier, T. S. Ward, M. Schoenitz, and E. L. Dreizin, “Reflected shock ignition combustion of aluminum and nanocomposite thermite powders,” *Combust., Sci., Technol.* vol. 179, no. 3, pp. 457–476, 2007.
- [7] J. Carleone, *Tactical Missile Warheads*, 155th ed. Boulder, Co: AIAA, 1993, pp. 127.
- [8] P. E. Eaton, M. Zhang, R. Gilardi, N. Gelber, S. Iyer, and R. Surapaneni, “Octonitrocubane: A new nitrocarbon,” *Propellants, Explos., Pyrotech.*, vol. 27, pp. 1–6, 2002.
- [9] R. Carole, *Al-based Energetic Nanomaterials*, Hoboken, NJ: John Wiley & Sons, Inc., 2015.
- [10] N. Fischer, D. Fischer, T. M. Klapötke, D. G. Piercey, and J. Stierstorfer, “Pushing the limits of energetic materials – the synthesis and characterization of dihydroxylammonium 5,5'-bistetrazole-1,1'-diolate,” *J. Mater. Chem.*, vol. 22, pp. 20418–20422, 2012.
- [11] K. O. Christe, D. A. Dixon, M. Vasiliu, R. I. Wagner, R. Haiges, J. A. Boatz, and H. L. Ammon, “Are DTTO and *iso*-DTTO worthwhile targets for synthesis,” *Propellants, Explos., Pyrotech.*, vol. 40, pp. 463–468, 2015.
- [12] P. Politzer, P. Lane, and J. Murray, “Computational characteristics of two di-1,2,3,4-tetrazine tetraoxides, DTTO and *iso*-DTTO, as potential energetic compounds,” *Cent. Eur. J. Energ. Mat.*, vol. 10, no. 1, pp. 37–52, 2013.

- [13] M. Zhang, P. E. Eaton, and R. Gilardi, "Hepta- and octonitrocubanes," *Agnew. Chem. Int. Ed.*, vol. 39, no. 2, pp. 401–404, 2000.
- [14] *CRC Handbook of Chemistry and Physics*, 97th ed., CRC Press, Boca Raton, FL, 2016.
- [15] R. L. Simpson, P. A. Urtiew, D. L. Ornellas, G. L. Moody, K. J. Scribner, and D. M. Hoffman, "CL-20 performance exceeds that of HMX and its sensitivity is moderate," *Propellants, Explos., Pyrotech.*, vol. 22, pp. 249–255, 1997.
- [16] R. J. Jouet, A. D. Warren, D. M. Rosenberg, V. J. Bellitto, K. Park, and M. R. Zachariah, "Surface passivation of bare aluminum nanoparticles using perfluoroalkyl carboxylic acids," *Chem. Mater.*, vol. 17, pp. 2987–2996, 2005.
- [17] V. I. Levitas, J. McCollum, M. Pantoya, "Pre-stressing micron-scale aluminum core-shell particles to improve reactivity," *Sci. Rep.*, vol. 5, no. 7879, pp. 1–6, 2015.
- [18] M. W. Beckstead, "A summary of aluminum combustion," NATO, RTO-EN-023, 2002.
- [19] S. E. Olsen and M. W. Beckstead, "Burn time measurements of single particle in steam and CO<sub>2</sub> mixtures," *J. Propul. Power*, vol. 12, no. 4, pp. 662–671, 1996.
- [20] E. L. Dreizin, "On the mechanism of asymmetric aluminum particle combustion," *Combust. Flame*, vol. 117, pp. 841–850, 1999.
- [21] C. Dohmeier, C. Robl, M. Tacke, and H. Schnöckel, "The tetrameric aluminum(I) compound [ $\{\text{Al}(\eta^5\text{-C}_5\text{Me}_5)\}_4$ ]," *Angew. Chem., Int. Ed.*, vol. 30, pp. 564–565, 1991.
- [22] M. Witt, H. W. Roesky, "Organoaluminum chemistry at the forefront of research and development," *Curr. Sci.* vol. 78, pp. 410–430, 2000.
- [23] H. Schnöckel, "Dalton discussion 11: The renaissance of main group chemistry," *Dalton, Trans.*, pp. 4344–4362, 2008.
- [24] H. Roesky and S. Kumar, "Chemistry of aluminium(I)," *Chem. Commun.*, pp. 4027–4038, 2005.
- [25] B. Buchin, T. Steinke, C. Gemel, T. Cadenbach, and R. Fischer, "Synthesis and characterization of the novel Al<sup>I</sup> compound Al(C<sub>5</sub>Me<sub>4</sub>Ph): Comparison of the coordination chemistry of Al(C<sub>5</sub>Me<sub>5</sub>) and Al(C<sub>5</sub>Me<sub>4</sub>Ph) at d<sup>10</sup> metal centers," *Z. Anorg. Allg. Chem.*, vol. 631, pp. 2756–2762, 2005.
- [26] A. Ecker, E. Weckert, and H. Schnöckel, "Synthesis and structural characterization of an Al<sub>77</sub> cluster," *Nature*, vol. 387, pp. 379–381, 1997.

- [27] A. Schnepf and H. Schnöckel, "Metalloid aluminum and gallium clusters: Element modifications on the molecular scale?" *Angew. Chem., Int. Ed.*, vol. 41, pp. 3532–3554, 2002.
- [28] H. Schnöckel and H. Köhnlein, "Synthesis and structure of metalloid aluminum clusters—Intermediates on the way to the elements." *Polyhedron*, vol. 21, pp. 489–501, 2002.
- [29] D. Bono, J. Hartig, M. Huber, H. Schnöckel, and L. Jongh, "<sup>27</sup>Al NMR study of the metal cluster compound Al<sub>50</sub>C<sub>120</sub>H<sub>180</sub>," *J. Cluster Sci.*, vol. 18, pp. 319–331, 2007.
- [30] H. Schnöckel, "Structures and properties of metalloid Al and Ga clusters open our eyes to the diversity and complexity of fundamental chemical and physical processes during formation and dissolution of metals," *Chem. Rev.*, vol. 110, pp. 4125–4163, 2010.
- [31] K. Williams and J. P. Hooper, "Structure, thermodynamics, and energy content of aluminum cyclopentadienyl clusters," *J. Phys. Chem. A*, vol. 115, pp. 14100–14109, 2011.
- [32] M. W. Beckstead, B. Newbold, and C. Waroquet, "A summary of aluminum combustion," in Proceedings of the 37th JANNAF Combustion Meeting, Monterey, CA, 2000, vol 1, p. 492.
- [33] S. Schulz, H. Roesky, H. Koch, G. Sheldrick, D. Stalke, and A. Kuhn, "A simple synthesis of [(Cp\*Al)<sub>4</sub>] and its conversion to the heterocubanes [(Cp\*AlSe)<sub>4</sub>] and [(Cp\*AlTe)<sub>4</sub>] (Cp\* = η<sup>5</sup>-C<sub>5</sub>(CH<sub>3</sub>)<sub>5</sub>)," *Angew. Chem., Int. Ed. Engl.*, vol. 32, pp. 1729–1731, 1993.
- [34] A. Purath, C. Dohmeier, A. Ecker, H. Schnöckel, K. Amelunxen, T. Passler, and N. Wiberg, "Synthesis and crystal structure of the tetraaluminatetrahedrane Al<sub>4</sub>[Si(*t*-Bu)<sub>3</sub>]<sub>4</sub>, the second Al<sub>4</sub>R<sub>4</sub> compound," *Organometallics*, vol. 17, pp. 1894–1896, 1998.
- [35] C. Schnitter, H. Roesky, C. Röpken, R. Herbst-Irmer, H. Schmidt, and M. Noltemeyer, "The behavior of [RAlX<sub>2</sub>·THF] compounds under reductive conditions: Tetrakis[tris(tri- methylsilyl)methylaluminum(I)]—A neutral aluminum(I) compound with σ-bound alkyl groups and a tetrahedral structure," *Angew. Chem., Int. Ed.*, vol. 37, pp. 1952–1955, 1998.
- [36] H. Sitzmann, M. Lappert, C. Dohmeier, C. Üffing, and H. Schnöckel, "Cyclopentadienyl-derivate von aluminium(I)," *J. Organomet. Chem.*, vol. 561, pp. 203–208, 1998.

- [37] M. Schiefer, N. Reddy, H. Roesky, and D. Vidovic, "Synthesis and structural characterization of an exclusively n-based tetrameric aluminum(I) compound," *Organometallics*, vol. 22, pp. 3637–3638, 2003.
- [38] A. Purath and H. Schnöckel, "Tetrakis[tris(trimethylsilyl)silyl]aluminum(I)  $\text{Al}_4[\text{Si}(\text{SiMe}_3)_3]_4$ —eine siliziumreiche Verbindung mit zentralem tetraedrischem  $\text{Al}_4$ -Kern," *J. Organomet. Chem.*, vol. 579, pp. 373–375, 1999.
- [39] M. Huber and H. Schnöckel, " $\text{Al}_4(\text{C}_5\text{Me}_4\text{H})_4$ : Structure, reactivity and bonding," *Inorg. Chim. Acta*, vol. 361, pp. 457–461, 2008.
- [40] R. Ahlrichs, M. Ehrig, and H. Horn, "Bonding in the aluminum cage compounds  $[\text{Al}(\eta^5\text{-C}_5\text{R}_5)]_4$  and  $\text{Al}_4\text{X}_4$ , X=H, F, Cl," *Chem. Phys. Lett.*, vol. 183, pp. 227–233, 1991.
- [41] U. Schneider, R. Ahlrichs, H. Horn, and A. Schäfer, "Ab initio investigations of structure and stability of  $[\text{R}_3\text{SiAl}]_4$  R = H, Me, *t*Bu," *J. Angew. Chem., Int. Ed.*, vol. 31, pp. 353–355, 1992.
- [42] C. Dohmeier, D. Loos, and H. Schnöckel, "Aluminum(I) and gallium(I) compounds: Syntheses, structure and reactions," *Angew. Chem., Int. Ed.*, vol. 35, pp. 129–149, 1996.
- [43] F. Alary, J.-L. Heully, R. Poteau, L. Maron, G. Trinquier, and J.-P. Daudey, "Using effective group potential methodology for predicting organometallic complex properties," *J. Am. Chem. Soc.*, vol. 125, pp. 11051–11061, 2003.
- [44] J. Vollet, J. R. Hartig, and H. Schnöckel, " $\text{Al}_{50}\text{C}_{120}\text{H}_{180}$ : A pseudofullerene shell of 60 carbon atoms and 60 methyl groups protecting a cluster core of 50 aluminum atoms," *Angew. Chem., Int. Ed.*, vol. 43, pp. 3186–3189, 2004.
- [45] M. Huber, P. Henke, and H. Schnöckel, "Experimentally based DFT calculations on the hindered disproportionation of  $[\text{Al}_4\text{Cp}^*_4]$ : Formation of metalloid clusters as intermediates on the way to solid Al prevents the decomposition of a textbook molecule," *Chem. Eur. J.*, vol. 15, pp. 12180–12183, 2009.
- [46] A. C. Stelzer, P. Hrobárik, T. Braun, M. Kaupp, and B. Braun-Cula, "Completing the heterocubane family  $[\text{Cp}^*\text{AlE}]_4$  (E = O, S, Se, and Te) by selective oxygenation and sulfuration of  $[\text{Cp}^*\text{Al}]_4$ : density functional theory calculations of  $[\text{Cp}^*\text{AlE}]_4$  and reactivity of  $[\text{Cp}^*\text{AlO}]_4$  toward hydrolysis," *Inorg. Chem.*, vol. 55, pp. 4915–4923, 2016.
- [47] G. Linti and H. Schnöckel, "Low valent aluminum and gallium compounds—Structural variety and coordination modes to transition metal fragments," *Coord. Chem. Rev.*, vol. 206-207, pp. 285-319, 2000.
- [48] C. Johnson and D. M. Morris, email communication, Jul. 2017.

- [49] W. Koch and M. C. Holthausen, *A Chemist's Guide to Density Functional Theory*, 2nd ed. Weinheim, Germany, WILEY-VCH, 2000.
- [50] F. Neese, "Prediction of molecular properties and molecular spectroscopy with density functional theory: From fundamental theory to exchange-coupling," *Cord. Chem. Rev.*, vol. 253, pp. 526–563, 2009.
- [51] P. Hohenberg and W. Kohn, "Inhomogeneous electron gas," *Phys. Rev.*, vol. 136, no. 3B, pp. B864-B871, 1964.
- [52] W. Kohn and L. J. Sham, "Self-consistent equations including exchange and correlation effects," *Phys. Rev.*, vol. 140, no. 4A, pp. A1133–A1138, 1965.
- [53] A. Karton, D. Gruzman, and J. M. L. Martin, "Benchmark thermochemistry of the  $C_nH_{2n+2}$  alkane isomers ( $n = 2-8$ ) and performance of DFT and composite ab initio methods for dispersion-driven isomeric equilibria," *J. Chem. Phys.*, vol. 113, pp. 8434–8447, 2009.
- [54] S. Grimme, J. Antony, S. Ehrlich, and H. Krieg, "A consistent and accurate ab initio parametrization of density functional dispersion correction (DFT-D) for the 94 elements H-Pu," *J. Chem. Phys.*, vol. 132, no. 154101, pp. 1–19, 2010.
- [55] Y. Zhao and D. Truhlar, "The M06 suite of density functionals for main group thermochemistry, thermochemical kinetics, noncovalent interactions, excited states, and transition elements: Two new functionals and systematic testing of four M06-class functionals and 12 other functionals," *Theor. Chem. Acc.*, vol. 120, pp. 215–241, 2008.
- [56] J. Wagner and P. Schreiner, "London dispersion in molecular chemistry-reconsidering steric effects," *Angew. Chem. Int. Ed.*, vol. 54, pp. 12274–12296, 2015.
- [57] K. Thanthiriwatte, E. Hohenstein, L. Burns, and C. Sherrill, "Assessment of the performance of DFT and DFT-D methods for describing distance dependence of hydrogen-bonded interactions," *J. Chem. Theory Comput.*, vol. 7, pp. 88–96, 2011.
- [58] L. Burns, Á. Vázquez-Mayagoitia, B. Sumpter, and C. Sherrill, "Density-functional approaches to noncovalent interactions: a comparison of dispersion corrections (DFT-D), exchange-hole dipole moment (XDM) theory, and specialized functionals," *J. Chem. Phys.*, vol. 134, no. 084107, pp. 1–25, 2011.
- [59] J. Klimeš and A. Michaelides, "Prospective: advances and challenges in treating van der Waals dispersion forces in density functional theory," *J. Chem. Phys.*, vol. 137, no. 120901, pp. 1–15, 2012.

- [60] H. Krieg and S. Grimme, "Thermochemical benchmarking of hydrocarbon bond separation reaction energies: jacob's ladder is not reversed!" *Mol. Phys.*, vol. 108, pp. 2655–2666, 2010.
- [61] L. Goerigk, H. Kruse, and S. Grimme, "Benchmarking density functional methods against the S66 and S66x8 datasets for non-covalent interactions," *ChemPhysChem*, vol. 12, pp. 3421–3433, 2011.
- [62] F. Lu, X. Li, Z. Sun, Y. Zeng, and L. Meng, "Influences of the substituents on the M–M bonding in  $\text{Cp}_4\text{Al}_4$  and  $\text{Cp}_2\text{M}_2\text{X}_2$  (M = B, Al, Ga; Cp =  $\text{C}_5\text{H}_5$ , X = halogen)," *Dalton, Trans.*, vol. 44, pp. 14092–14100, 2015.
- [63] C. Ganesamoorthy, S. Loerke, C. Germel, P. Jarabek, M. Winter, G. Frenking, and R. Fischer, "Reductive elimination: a pathway to low-valent aluminium species," *Chem. Commun.*, vol. 49, no. 28, pp. 2837–2944, Apr. 2013.
- [64] L. Goerigk and S. Grimme, "Efficient and accurate double-hybrid-meta-GGA density functionals—evaluation with the extended GMTKN30 database for general main group thermochemistry, kinetics, and noncovalent interactions," *J. Chem. Theory Comput.*, vol. 6, pp. 107–126, 2010.
- [65] H. Kruse, L. Goerigk, and S. Grimme, "Why the standard B3LYP/6-31G\* model chemistry should not be used in DFT calculations of molecular thermochemistry: Understanding and correcting the problem," *J. Org. Chem.*, vol. 77, pp. 10824–10834, 2012.
- [66] A. Becke, "Density-functional exchange-energy approximation with correct asymptotic-behavior. *Phys. Rev. A*, vol. 38, pp. 3098–3100, 1988.
- [67] J. Perdew, "Density-functional approximation for the correlation energy of the inhomogeneous electron gas. *Phys. Rev. B*, vol. 33 pp. 8822–8824, 1986.
- [68] A. Becke, "Density-functional thermochemistry. III. The role of exact exchange," *J. Chem. Phys.*, vol. 98, pp. 5648–5652, 1993.
- [69] J. Tao, J. Perdew, V. Staroverov, and G. Scuseria, "Climbing the density functional ladder: Nonempirical meta-generalized gradient approximation designed for molecules and solids," *Phys. Rev. Lett.*, vol. 91, no. 146401, pp. 1–4, 2003.
- [70] J. Perdew, K. Burke, and M. Ernzerhof, "Generalized gradient approximation made simple. *Phys. Rev. Lett.*, vol. 77, pp. 3865–3868, 1996.
- [71] C. Adamo and V. Barone, "Toward reliable density functional methods without adjustable parameters: The PBE0 model," *J. Chem. Phys.*, vol. 110, pp. 6158–6169, 1999.

- [72] Y. Zhao and D. Truhlar, "A new local density functional for main-group thermochemistry, transition metal bonding, thermochemical kinetics, and noncovalent interactions," *J. Chem. Phys.*, vol. 125, pp. 1–18, 2006.
- [73] C. Adamo and V. Barone, "Exchange functionals with improved long-range behavior and adiabatic connection methods without adjustable parameters: The *mPW* and *mPW1PW* models," *J. Chem. Phys.*, vol. 108, pp. 664–675, 1998.
- [74] A. Austin, G. Petersson, M. Frisch, F. Dobek, G. Scalmani, and K. Throssell, "A density functional with spherical atom dispersion terms," *J. Chem. Theory and Comput.*, vol. 8, no. 12, pp. 4989–5007, 2012.
- [75] A. McLean and G. Chandler, "Contracted gaussian basis sets for molecular calculations. I. Second row atoms,  $Z=11-18$ ," *J. Chem. Phys.*, vol. 72, pp. 5639–5648, 1980.
- [76] T. Clark, J. Chandrasekhar, G. Spitznagel, and P. Schleyer, "Efficient diffuse function-augmented basis sets for anion calculations. III. The 3-21+G basis set for first-row elements, Li–F," *J. Comp. Chem.*, vol. 4, pp. 294–301, 1983.
- [77] F. Weigend and R. Ahlrichs, "Balanced basis sets of split valence, triple zeta valence and quadruple zeta valence quality for H to Rn: Design and assessment of accuracy," *Phys. Chem. Chem. Phys.*, vol. 7, pp. 3297–3305, 2005.
- [78] A. Schaefer, H. Horn, and R. Ahlrichs, "Fully optimized contracted gaussian basis sets for atoms Li to Kr," *J. Chem. Phys.*, vol. 97, pp. 2571–2577, 1992.
- [79] M. M. Francl, W. J. Pietro, W. J. Hehre, J. S. Binkley, D. J. DeFrees, J. A. Pople, and M. S. Gordon, "Self-consistent molecular orbital methods. XXIII. A polarization-type basis set for second-row elements," *J. Chem. Phys.*, vol. 77, pp. 3654–3665, 1982.
- [80] T. H. Dunning, "Gaussian basis sets for use in correlated molecular calculations. I. The atoms boron through neon and hydrogen," *J. Chem. Phys.*, vol. 90, pp. 1007–1023, 1989.
- [81] V. Subramanian, D. Sivanesan, J. Padmanabhan, N. Lakshminarayanan, and T. Ramasami, "Atoms in molecules: application to electronic structure of van der waals complexes," *Proc. Indian Acad. Sci. (Chem. Sci.)*, vol. 111, pp. 369–375, 1999.
- [82] R. Bader and H. Essén, "The characterization of atomic interactions," *J. Chem. Phys.*, vol. 80, pp. 1943–1960, 1984.
- [83] R. Bader, T. Slee, D. Cremer, and E. Kraka, "Description of conjugation and hyperconjugation in terms of electron distributions," *J. Am. Chem. Soc.*, vol. 105, pp. 5061–5068, 1983.

- [84] D. Cremer and E. Kraka, "A description of the chemical bond in terms of local properties of electron density and energy," *Croat. Chem. Acta.*, vol. 57, pp. 1259–1281, 1984.
- [85] G. Bone and F. Bader, "Identifying and analyzing intermolecular bonding interactions in van der waals molecules," *J. Phys. Chem.*, vol. 100, pp. 10892–10911, 1996.
- [86] F. Cortés-Guzmán and R. Bader, "Complementarity of QTAIM and MO theory in the study of bonding in donor–acceptor complexes," *Coord. Chem. Rev.*, vol. 249, pp. 633–662, 2005.
- [87] R. Bianchi, G. Gervasio, and D. Marabello, "Experimental electron density analysis of  $\text{Mn}_2(\text{CO})_{10}$ : Metal-metal and metal-ligand bond characterization," *Inorg. Chem.*, vol. 39, pp. 2360–2366, 2000.
- [88] L. Farrugia, C. Evans, D. Lentz, and M. Roemer, "The QTAIM approach to chemical bonding between transition metals and carbocyclic rings: A combined experimental and theoretical study of  $(\eta^5\text{-C}_5\text{H}_5)\text{Mn}(\text{CO})_3$ ,  $(\eta^6\text{-C}_6\text{H}_6)\text{Cr}(\text{CO})_3$ , and  $(E)\text{-}\{(\eta^5\text{-C}_5\text{H}_4)\text{CF}=\text{CF}(\eta^5\text{-C}_5\text{H}_4)\}(\eta^5\text{-C}_5\text{H}_5)_2\text{Fe}_2$ ," *J. Am. Chem. Soc.*, vol. 131, pp. 1251–1268, 2009.
- [89] P. H. M. Budzelaar, J. J. Engelberts, and J. H. van Lenthe, "Trends in cyclopentadienyl-main-group-metal bonding," *Organometallics*, vol. 22, pp. 1562–1576, 2003.
- [90] S. Grabowski, "An estimation of strength of intramolecular hydrogen bonds – ab initio and AIM Studies," *J. Mol. Struct.*, vol. 562, pp. 137–143, 2001.
- [91] S. Grabowski, "High-level ab initio calculations of dihydrogen-bonded complexes. *J. Phys. Chem. A.*, vol. 104, pp. 5551–5557, 2000.
- [92] R. Boyd and S. Choi, "Hydrogen bonding between nitriles and hydrogen halides and the topological properties of molecular charge distributions," *Chem. Phys. Lett.*, vol. 129, pp. 62–65, 1986.
- [93] J. J. Mortensen, L. B. Hansen, and K. W. Jacobsen, "Real-space grid implementation of the projector augmented wave method," *Phys. Rev. B*, vol. 71, no. 035109, pp. 1–13, 2005.
- [94] J. Enkovaara, C. Rostgaard, and J. J. Mortensen et al., "Electronic structure calculations with GPAW: a real-space implementation of the projector augmented-wave method," *J. Phys.: Condens. Matter*, vol. 22, no. 253202, pp. 1–24, 2010.

- [95] A. H. Larsen, et al., “The Atomic Simulation Environment—A Python library for working with atoms,” *J. Phys.: Condens. Matter*, vol. 29, no. 273002, pp. 1–30, 2017.
- [96] P. E. Blöchl, C. J. Först, and J. Schimble, “Projector augmented wave method: *ab initio* molecular dynamics with full wave functions,” *Bull. Mater. Sci.*, vol. 26, no. 1, pp. 33–41, 2003.
- [97] A. Tkatchenko and M. Scheffler, “Accurate molecular van der Waals interactions from ground-state electron density and free-atom reference data,” *Phys. Rev. Lett.*, vol. 102, no. 073005, pp. 1–4, 2009.
- [98] D. M. Deaven and K. M. Ho, “Molecular geometry optimization with a genetic algorithm,” *Phys. Rev. Lett.*, vol. 75, no. 2, pp. 288–291, 1995.
- [99] L. B. Vilhelmsen and B. Hammer, “A genetic algorithm for first principles global structure optimization of supported nano structures,” *J. Chem. Phys.*, vol. 141, no. 044711, pp. 1–11, 2014.
- [100] R. L. Johnston, “Evolving better nanoparticles: Genetic algorithms for optimizing cluster geometries,” *Dalton Trans.*, pp. 4193–4207, 2003.
- [101] A. D. Becke and K. E. Edgecombe, “A simple measure of electron localization in atomic and molecular systems,” *J. Chem. Phys.*, vol. 92, no. 9, pp. 5397–5403, 1990.
- [102] W. Pauli, “Über den zusammenhang des abschlusses der elektronengruppen im atom mit der komplexstruktur der spektren,” *Z. Physik*, vol. 31, no. 1, pp. 765–783, 1925.
- [103] J. K. Burdett and T. A. McCormick, “Electron localization in molecules and solids: the meaning of ELF,” *J. Chem. Phys.*, vol. 102, pp. 6366–6372, 1998.
- [104] P. Fuentealba, E. Chamorro, and J. C. Santos, “Understanding and using the electron localization function,” *Theoretical Aspects of Computational Reactivity*, vol. 19, pp. 57–85, 2007.
- [105] B. Silvi, “The synaptic order: a key concept to understanding multicenter bonding,” *J. Mol. Struct.*, vol. 614, pp. 3–10, 2003.
- [106] C. Massobrio, P. Rabu, M. Drillon, and C. Rovira, “Structural properties, electron localization and magnetic behavior of copper hydroxonitrate: a density functional study,” *J. Phys. Chem. B.*, vol. 103, pp. 9387–9391, 1999.
- [107] C. Kolano, J. Helbing, M. Koriusz, W. Sander, and P. Hamm, “Watching hydrogen-bond dynamics in a  $\beta$ -turn by transient two-dimensional infrared spectroscopy,” *Nature (London)*, vol. 444, pp. 469–472, 2006.

- [108] R. F. W. Bader, "A Bond Path: A universal indicator of bonded interactions," *J. Phys. Chem. A*, vol. 102, pp. 7314–7323, 1998.
- [109] X. Li, S. Huo, Y. Zeng, Z. Sun, S. Zheng, and L. Meng, "Metal-metal and metal-ligand bonds in  $(\eta^5\text{-C}_5\text{H}_5)_2\text{M}_2$  (M = Be, Mg, Ca, Ni, Cu, Zn)", *Organometallics*, vol. 32, pp. 1060–1066, 2013.
- [110] *Gaussian 09*, revision E01, Gaussian Inc., Wallingford, CT, 2009.
- [111] *Gaussian 16*, revision A03, Gaussian Inc., Wallingford, CT, 2016.
- [112] S. Boys and F. Bernardi, "The calculation of small molecular interactions by the differences of separate total energies. some procedures with reduced errors," *Mol. Phys.*, vol. 19, pp. 553–566, 1970.
- [113] A. Klamt and G. Schüürmann, "COSMO: A new approach to dielectric screening in solvents with explicit expressions for the screening energy and its gradient," *J. Chem. Soc., Perkin Trans 2*, pp. 799–805, 1993.
- [114] V. Barone and M. Cossi, "Quantum calculation of molecular energies and energy gradients in solution by a conductor solvent model," *J. Phys. Chem. A*, vol. 102, pp. 1995–2001, 1998.
- [115] M. Kohout, Radebeul. (2014). *DGrid version 4.6*, [Online]. Available: <http://www2.cpfs.mpg.de/~kohout/dgrid.html>. Accessed Sep. 21, 2016.
- [116] K. Wolinski, J. Hilton, and P. Pulay, "Efficient implementation of the gauge-independent atomic orbital method for NMR chemical shift calculations. *J. Am. Chem. Soc.*, vol. 112, pp. 8251–8260, 1990.
- [117] F. Feixas, E. Matito, M. Duran, and M. Solà, "," *J. Chem. Theor. And Comp.*, vol. 6, no. 9, pp. 2736-2742, 2010.
- [118] S. Noury, X. Krokidis, F. Fuster, and B. Silvi, "," *Computers and Chemistry*, vol. 23, no. 6, pp. 597–604, 1999.
- [119] E. Matito, B. Silvi, M. Duran, and M. Solà, "," *J. Chem. Phys.*, vol. 125, no. 024301, pp. 1–9, 2006.

## INITIAL DISTRIBUTION LIST

1. Defense Technical Information Center  
Ft. Belvoir, Virginia
2. Dudley Knox Library  
Naval Postgraduate School  
Monterey, California